
Calibrating the ATLAS Muon Spectrometer for a Search for Charged Stable Massive Particles

Master's thesis
at the Faculty of Physics
of the Ludwig-Maximilians-Universität München

submitted by
Martin Habedank
born in Berlin

Munich, 15 November 2018

**Kalibration des
ATLAS-Myonenspektrometers für eine
Suche nach geladenen, stabilen,
massiven Teilchen**

Masterarbeit
an der Fakultät für Physik
der Ludwig-Maximilians-Universität München

eingereicht von
Martin Habedank
geboren in Berlin

München, den 15. November 2018

Supervisor: Prof. Dr. Dorothee Schaile

Abstract

Many theories extending the Standard Model predict charged stable massive particles in reach of the LHC. In the last years, ATLAS conducted multiple searches for those particles as they offer signatures distinct from that of every Standard Model particle: Due to their high mass, stable massive particles are expected to exhibit velocities significantly below the speed of light, providing a model-independent approach to observe New Physics. As low particle velocities result in large times of flight, in particular in the outer parts of the detector, timing measurements in the ATLAS muon spectrometer provide a valuable handle for those searches.

Meaningful timing and velocity measurements are impossible without an in-depth calibration of the muon spectrometer systems, which was therefore carried out for the previous ATLAS searches. A complete revision of the ATLAS reconstruction algorithm for charged stable massive particles in the last few years requires a renewed approach to the muon spectrometer calibration.

This thesis presents studies on the changes coming with the new reconstruction algorithm and provides a novel understanding of the algorithm's output. In addition, a calibration procedure for timing measurements with the ATLAS muon spectrometer is described that seizes upon the previous calibration and extends it, involving corrections of charge drift times and propagation times of signals, and deriving calibration constants for more than 735,000 detector elements. Thereby, it takes advantage of the new reconstruction algorithm for charged stable massive particles and the enlarged dataset of 128.3 fb^{-1} of proton–proton collisions taken with the ATLAS particle detector at $\sqrt{s} = 13 \text{ TeV}$ in 2015–2018.

Contents

Abstract	v
Contents	ix
1 Introduction	1
2 The Standard Model and New Physics	3
2.1 Fundamental interactions in the Standard Model	3
2.2 Particle content of the Standard Model	4
2.3 Open questions	5
2.4 New Physics	8
2.4.1 Supersymmetry	8
2.5 Longevity of particles	11
2.5.1 Longevity in the Standard Model	12
2.5.2 Longevity in BSM theories	12
3 Experimental setup	15
3.1 The Large Hadron Collider	15
3.2 The ATLAS experiment	18
3.2.1 Inner Detector	21
3.2.2 Calorimeters	22

3.2.3	Muon spectrometer	23
4	Searches for charged stable massive particles with ATLAS	31
4.1	Observables	31
4.2	Reconstruction	33
4.2.1	Need for a dedicated reconstruction algorithm	34
4.3	Current results	37
4.4	Upcoming searches	37
4.4.1	Changes in the new reconstruction algorithm	37
5	Timing calibration of the ATLAS muon spectrometer	45
5.1	Data and simulated events	46
5.2	Event selection	46
5.3	Uncalibrated distributions	48
5.4	Previous calibration	52
5.5	Drift-time calibration	55
5.6	Propagation-time calibration	58
5.6.1	MDTs	58
5.6.2	RPCs	60
5.7	Run-wise calibration	62
5.8	Element-wise calibration	69
5.9	Second run-wise calibration	72
5.10	Pull correction and final β resolution	75
5.11	Evaluation of the impact of missing MDT hits	78
5.12	Comparison between the years	78
6	Simulation treatment	81

Contents	ix
6.1 Element-wise treatment	81
6.2 Chamber-wise treatment	87
6.3 Signal treatment	93
7 Conclusion and Outlook	97
A Missing MDT hits in the barrel region of the ATLAS side C	99
B Attempt for an analytical propagation-time correction for RPCs	105
Bibliography	111
List of Abbreviations	121
Acknowledgement	127

Chapter 1

Introduction

The fundament of modern particle physics is the Standard Model, providing an extensive theoretical framework for elementary particles and their interactions. In an astonishing way, it did not only explain known interactions but was even able to predict particles unobserved at that time, decades before technology was advanced enough to find final evidence of their existence. However, success is no guarantor for completeness and indeed, more and more observations pile up, indicating the need for theories beyond the Standard Model: The Standard Model is neither able to answer questions on the origin of dark matter nor capable of explaining the imbalance between matter and antimatter, to name but two. Thus, there is a variety of theories extending the Standard Model, aiming to mend its shortcomings. Since many of them give rise to new particles, as of yet missing evidence for those theories could be found with the ATLAS particle detector at the LHC. In a broad range of theories extending the Standard Model, charged stable massive particles are predicted. Those allow a compelling approach for a model-independent search for new particles by measuring ionisation energy losses and times of flight: Due to their charge and mass higher than that of any elementary Standard Model particle, they would suffer large ionisation energy losses. In addition, their high mass also causes them to propagate with a velocity significantly lower than the speed of light. Thus, given they are stable and therefore able to traverse the whole detector, they would exhibit times of flight larger than any Standard Model particle can obtain. In consequence, they would leave signatures distinct from that of any Standard Model particle in the detector, if any, comparable to that of a slow heavy muon. Thus, these searches offer the rare opportunity to investigate theories extending the Standard Model without being model-specific or having a physical background. Indeed, the only background that has to be considered in those searches is that of instrumental mismeasurements. To account for this and to be able to assign a mass to potential observed particles, an in-depth understanding and thorough timing calibration of the detector is mandatory.

ATLAS conducted multiple searches for charged stable massive particles that as of yet did not observe a significant excess over the estimated background. For the time-of-flight measurements of those searches, the tile calorimeter as well as resistive-plate chambers and monitored drift tubes were deployed after an in-depth calibration. Due to their large time of

flight, particle–detector interactions are registered in those systems considerably later than expected by algorithms running on ATLAS data trying to reconstruct muon trajectories. As this significantly decreases their reconstruction efficiency, an algorithm dedicated to reconstruct charged stable massive particles is used in the searches with ATLAS. In the last few years, this reconstruction algorithm received a major revision to account for known difficulties. Among others, the effects of this revision are investigated in this thesis, with a focus on the reconstruction efficiency.

In addition, in its new form, the dedicated reconstruction algorithm renders the previous calibrations outdated, demanding for a renewed approach on those. In the work at hand, the procedure for the timing calibration of the muon spectrometer systems used in searches for charged stable massive particles with ATLAS is presented.

For a summary of the different topics and order of chapters in this thesis, the reader may be referred to the table of contents. As a vast amount of abbreviations is common in particle physics that this thesis adopts and tries to explain, a list of abbreviations with short explanations is given at the end of this work.

Chapter 2

The Standard Model and New Physics

The Standard Model of particle physics (SM) is a gauge theory that has enormous success in explaining and predicting the elementary particles of matter and their interactions, making it the fundament of modern particle physics. Nevertheless, there are questions left open by the SM which give rise to theories Beyond the Standard Model (BSM) or so-called New Physics. As the work at hand focusses on a calibration for a search for charged stable massive BSM particles it is instructive to review the aforementioned topics and give a more thorough look at long-lived and stable particles in general.

It is important to note here that the common convention in particle physics $c := \hbar := 1$ is used in the work at hand.

2.1 Fundamental interactions in the Standard Model

As of current knowledge, there is only a limited set of fundamental interactions: electromagnetic, weak, strong and gravitational interaction [1]. To date, gravity could not be successfully incorporated into the Standard Model, making it a theory accounting for the remaining three fundamental interactions. This is no critical drawback for the SM, though: While gravity plays a dominant role for example in astrophysics, it is weak compared to the other three on short scales and at low energies and thus negligible in today's particle physics [2].

The electromagnetic interaction is described in the Standard Model by the quantum field theory (QFT) called quantum electrodynamics (QED), which is a gauge theory with symmetry group $U(1)_{QED}$. It deals with electrically charged particles like electrons (e^-) and their interactions via photons (γ).

The weak interaction is responsible for flavour changes in Standard Model processes and allows for momentum exchange between electrically uncharged particles. It acts only on left-handed particles and can be described by the symmetry group $SU(2)_L$. One of the large successes of the Standard Model is the unification of weak and electromagnetic inter-

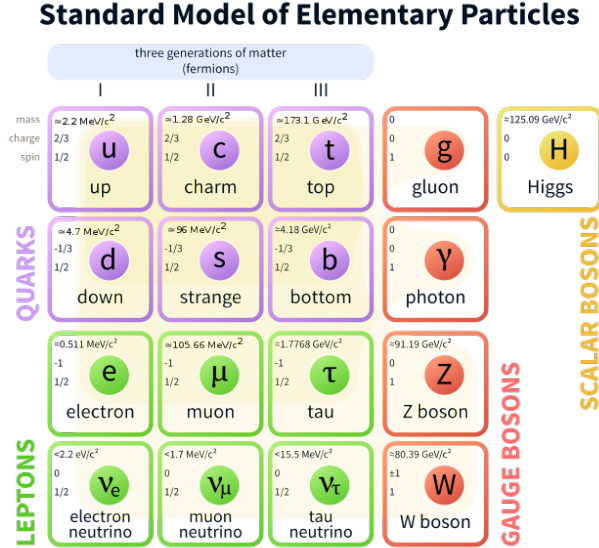


Figure 2.1: Overview of the particle content of the Standard Model. Figure was taken from [4].

action, forming the symmetry group $SU(2)_L \otimes U(1)_Y$ [3]. Hereby, the electric charge Q of QED is absorbed into the hypercharge $Y := 2(Q - I_3)$, where I_3 is the third component of the weak isospin.

Quantum chromodynamics (QCD) is the theory of the strong interaction, which accounts for the force between particles carrying a colour charge (usually chosen to be red, green and blue) like quarks (q) or composite particles like protons (p). As its gauge group is $SU(3)_C$, the total symmetry of the Standard Model can be expressed as $SU(3)_C \otimes SU(2)_L \otimes U(1)_Y$.

2.2 Particle content of the Standard Model

A summary of the elementary particles described by the Standard Model including their charge, spin and mass can be found in Figure 2.1.

Most elementary SM particles have spin $1/2$ and are therefore fermions, i.e., particles with half-integer spin. They can be divided by their interactions into leptons and quarks.

Leptons carry no colour charge and thus do not interact strongly. There are six different *flavours* of leptons, which are grouped into three generations, each consisting of two particles: a particle with electric charge $-1 e$ (electron e^- , muon μ^- , tau τ^-) and a neutrino (ν_e , ν_μ , ν_τ) that is electrically uncharged and (almost) massless. The generations have identical quantum numbers but they differ in their mass, e being the lightest charged lepton and τ the heaviest. For each flavour, there is also an antiparticle with the same mass but opposite charges.

Like leptons, quarks can be divided into three generations with equal quantum numbers but different masses. Each generation contains two flavours: An up- and a down-type

quark (named after the up quark (u) and down quark (d) of the first and lightest generation) with electric charge $+\frac{2}{3}e$ and $-\frac{1}{3}e$, respectively. The corresponding particles of the second generation are the strange quark (s) and charm quark (c). The third and heaviest generation yields the bottom quark (b) and top quark (t). In difference to leptons, quarks also carry a colour charge and therefore undergo strong interaction. Thus, they are subject to all four fundamental interactions. Like for leptons, an antiparticle with same mass but opposite charges exists for each flavour.

All non-fermionic particles are bosons, carrying an integer spin. In the Standard Model, the various mediators of the fundamental interactions are all bosons of spin 1: The electrically uncharged photon (γ) transmits electromagnetic interactions and therefore couples only to electrically charged particles. Gluons (g) are the mediators of the strong interaction. They do not carry electric charge but colour, which allows them to couple to every colour-charged particle, including themselves. As the symmetries of the generators of electromagnetic and strong interaction are unbroken, photons and gluons are massless.

This is not the case for W^+ , W^- and Z^0 bosons, which mediate the electroweak interaction: The symmetry of the electroweak interaction is spontaneously broken and thus its mediators carry mass, which also allows them to interact with every other Standard Model particle except for gluons.

The only elementary Standard Model boson without spin 1 is the Higgs boson (H^0), the mediator of the Higgs field, with spin 0. The Higgs field is responsible for the spontaneous symmetry breaking of the electroweak symmetry, giving mass to W^\pm and Z bosons. It is electrically- and colour-neutral and was the last elementary particle of the Standard Model to be discovered [5,6]. Only recently its most dominant decay mode (into pairs of b quarks) was observed [7,8].

Out of the various elementary SM particles also composite particles can be created. Subatomic composite particles are called hadrons and are either mesons, with quark–antiquark ($q\bar{q}$) content and spin 0 or 1, or baryons, with spin $1/2$ consisting of three quarks (qqq).

Apart from this nominal quark content (referred to as *valence quarks*), hadrons also consist of other constituents: Due to the intense colour field in hadrons, gluons mediating the strong interaction between the (anti)quarks can constantly split into virtual quark–antiquark pairs. Those are *virtual*, as they, in turn, annihilate after a very short period of time and form gluons again [9]. The quarks of this indeterminate additional particle content of hadrons are referred to as *sea quarks*. Nevertheless, as the quantum numbers of hadrons are defined by their valence quarks only those are usually stated as their quark content.

2.3 Open questions

Although the Standard Model had enormous success not only in explaining elementary particles but also in predicting them — as examples charm [10] and top quarks [11] as

well as W^\pm , Z [12] and Higgs bosons [13] shall be mentioned here — there are still some questions that cannot be solved within the Standard Model.

One of those was the problem of neutrino oscillations. While neutrinos are considered massless in the Standard Model, their detected flavour oscillations [14] require them to have mass. This problem could be solved by extending the Standard Model towards massive neutrinos [1].

Nevertheless, there are further questions that still lack an appropriate answer. Selected ones are introduced in the following.

Matter–antimatter asymmetry

The fact that the observable universe is made of matter, while there is almost no antimatter, inevitably leads to the questions of why and how such an imbalance could be produced. While there are attempts to explain this within the Standard Model, those arguments usually lead to an asymmetry orders of magnitude below observation [15].

Dark matter

Observations of gravitational lensing, the structure of the cosmic microwave background (CMB), X-ray radiation of galaxy collisions, galaxy rotation curves and many more give evidence that there has to be an electrically neutral, massive and not very strongly interacting particle, usually referred to as *dark matter* [16]. The Standard Model does neither yield another explanation for those observations nor an appropriate candidate for dark matter.

Unification of forces

The successful unification of electromagnetic and weak interaction into the electroweak interaction gives rise to efforts to also merge the remaining two other interactions — strong and gravitational — with the electroweak interaction. As shown in Figure 2.2a, the gauge couplings do not obtain a common value at any scale in the SM, though.

The unification of the strong with the electroweak interaction is called Grand Unified Theory (GUT) and expected to happen at the GUT scale at $\mathcal{O}(10^{16} \text{ GeV})$ [17, p. 855]. It would be accompanied by a merging of the gauge couplings as sketched in Figure 2.2b.

The GUT scale is still clearly below the Planck scale $\mathcal{O}(10^{19} \text{ GeV})$, at which gravity cannot be neglected in particle interactions anymore, leading to a theory explaining quantum gravity and thus the unification of all four fundamental forces [1].

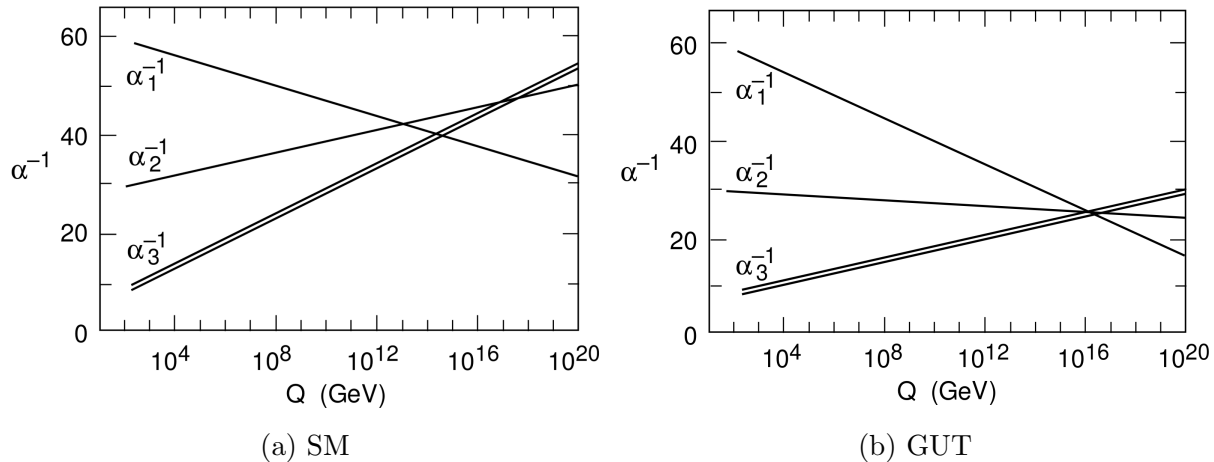


Figure 2.2: Evolution of the gauge couplings $\alpha_{1,2,3}^{-1}$ for electromagnetic, weak and strong interaction, respectively, as a function of momentum transfer Q of an interaction. In the Standard Model there is no unification of couplings (a), while a hypothetic GUT could allow for that (b). The double line for α_3 indicates the larger experimental error in this quantity compared to $\alpha_{1,2}$. Figures adapted from [18].

Hierarchy problem

While the finding of the Higgs boson in 2012 is a large success of the Standard Model [1], its considerably low mass of about 125 GeV is in fact a slight reason for concern: The Higgs boson mass m_H is closely related to the Higgs field with the potential

$$V(\Phi) = -\mu^2 |\Phi|^2 + \lambda^2 |\Phi|^4$$

because $\mu = \frac{m_H}{\sqrt{2}}$. In consequence, m_H receives large quantum corrections from each particle that couples to the Higgs field. Fermions, for example, can yield loop corrections to the Higgs potential according to Figure 2.3a, which result in corrections for the Higgs mass [19] corresponding to

$$\Delta m_H^2 \approx -\frac{|\lambda_f|^2}{8\pi^2} \Lambda_{UV}^2. \quad (2.1)$$

Here, higher-order corrections have been neglected. λ_f is the coupling constant of fermions to the Higgs field, hence related to the mass of the considered fermion. Λ_{UV} is the so-called ultraviolet momentum cut-off, which can be interpreted as the maximum energy scale up to which the theory is valid. Taking Λ_{UV} to be of the order of the Planck scale $\mathcal{O}(10^{19} \text{ GeV})$ or considering only one particle substantially heavier than Standard Model particles, the mass corrections for the Higgs boson become enormous. This of course raises the question why the Higgs boson mass (and with it the entire mass spectrum of the Standard Model) is actually of the order of the electroweak scale and not much more massive.

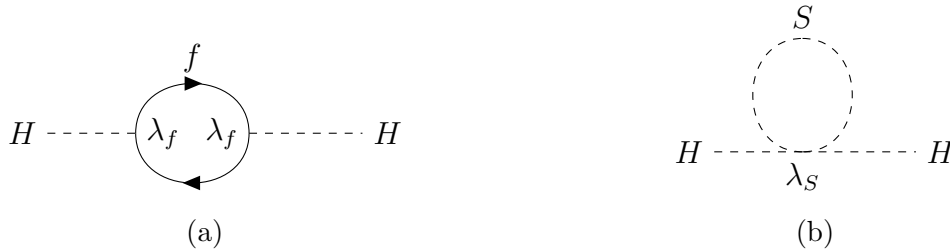


Figure 2.3: Loop diagrams for quantum corrections to the Higgs mass of a fermion with coupling constant λ_f (a) and of a scalar boson with coupling constant λ_S (b).

2.4 New Physics

There is a large variety of BSM theories which address the above stated open questions. A candidate for dark matter, for example, is provided by the axion, which was initially introduced to solve the strong CP-problem (the fact that there is no CP violation in the strong sector) [16]. Recent experiments [20] place strong limits onto the coupling constant to electrons, though.

Models with Universal Extra Dimensions (UED) introduce additional compactified spatial dimensions, which then allow to address the hierarchy problem while at the same time providing a dark matter candidate [16].

The perhaps most prominent example for a BSM theory, however, is supersymmetry, which shall be regarded more closely in the following.

2.4.1 Supersymmetry

Supersymmetry (SUSY) [21–26] refers to a group of models that primarily addresses the hierarchy problem while conveniently ”on the way” often also providing a unification of the strong and electroweak interactions [27–30] and a dark matter candidate [31,32]. They exploit the fact that, similar to the fermionic case in equation (2.1), the correction to the Higgs mass m_H for scalar bosons by coupling as shown in Figure 2.3b is

$$\Delta m_H^2 \approx \frac{\lambda_S}{16\pi^2} [\Lambda_{UV}^2 - 2m_S^2 \ln(\Lambda_{UV}/m_S)], \quad (2.2)$$

where again higher-order corrections have been neglected [19]. Here λ_S is the coupling constant of the scalar boson to the Higgs field and therefore closely related to the mass of the scalar boson m_S . Comparing equations (2.1) and (2.2), one recognises that the Λ_{UV}^2 terms cancel nicely if one Standard Model fermion is always associated with two scalar bosons that have $\lambda_S = |\lambda_f|^2$. This suggests there exists a new symmetry relating fermions and bosons, referred to as *supersymmetry*. Mathematically, this supersymmetry would be based on operators Q that transform fermionic states into bosonic ones and vice versa:

$$Q |\text{fermion}\rangle = |\text{boson}\rangle \quad Q |\text{boson}\rangle = |\text{fermion}\rangle$$

Adding even more restrictions on the model can ensure that also higher-order corrections in equations (2.1) and (2.2) cancel each other.

Particles transformed into each other by Q then are referred to as *superpartners*, which yield the exact same quantum numbers like electric charge, except for the spin whereby one of course is integer and the other half-integer. Superpartners form so-called *supermultiplets* [33].

To linguistically distinguish SUSY and SM particles, the SUSY superpartners of SM fermions acquire the prefix "s" to indicate their *scalar* character; SUSY superpartners of SM bosons acquire the suffix "ino". As those pre- and suffixes are not visible in notation, SUSY particles are denoted with an additional tilde " \sim " above the particle symbol. Consequently, SUSY particles are for example the top squark (\tilde{t}), stau ($\tilde{\tau}$) or zino (\tilde{Z}). This naming convention also applies to larger categories, hence the SUSY superpartners of fermions are called sfermions, the SUSY superpartners of gauge bosons gauginos, etc. For each SM particle, there is at least one SUSY superpartner, whereby the left- and right-handed pieces of fermions acquire separate superpartners, e.g., the superpartners of the left- and right-handed component of electrons, e_L and e_R , are \tilde{e}_L and \tilde{e}_R , respectively. The indices L and R of the SUSY particle then do not denote their handedness anymore.

In principle, SUSY models can yield a much larger particle content than just the factor of roughly two suggested by above remarks, and in fact, they have to if they want to avoid gauge anomalies [34]. Accordingly, even the extension of the Standard Model that adds minimal additional particle content — known as the Minimal Supersymmetric (version of the) Standard Model (MSSM) [35,36] — requires five Higgs bosons instead of the familiar single one [37]. At least one of those had to be lighter than 135 GeV, though, such that the discovery of a Higgs boson with mass 125 GeV in 2012 could be counted as a successful prediction of supersymmetry theories — in contrast to the SM, which allowed no prediction of the Higgs boson mass [19].

In the MSSM, electroweak symmetry breaking, which gave mass to W^\pm and Z^0 bosons, causes a mixing of the electrically neutral gauginos and higgsinos into four neutral mass eigenstates χ_i^0 ($i = 1, 2, 3, 4$) called neutralinos. The same happens for electrically charged gauginos and higgsinos, giving rise to four charginos χ_i^\pm ($i = 1, 2$). For sfermions, mixing takes place as well, but apart from the third generation sfermions — which form the mass eigenstates \tilde{t}_i , \tilde{b}_i and $\tilde{\tau}_i$ ($i = 1, 2$) — it is negligible. The complete additional particle content predicted by the MSSM can be seen in Table 2.1.

R-parity

In the SM, lepton number L and baryon number B are conserved in interactions. The most striking reason why this is necessary is the proton decay: It is imaginable that protons (p^+) — which are baryons with quark content uud — could decay according to $p^+ \rightarrow e^+ \pi^0$ into a positron (e^+ , the antiparticle to the electron e^-) and a pion (π^0 , a meson

Names	Spin	P_R	Gauge Eigenstates	Mass Eigenstates
Higgs Bosons	0	+1	$H_u^0 H_d^0 H_u^+ H_d^-$	$h^0 H^0 A^0 H^\pm$
Squarks	0	-1	$\tilde{u}_L \tilde{u}_R \tilde{d}_L \tilde{d}_R$	same
	0	-1	$\tilde{s}_L \tilde{s}_R \tilde{c}_L \tilde{c}_R$	same
Sleptons	0	-1	$\tilde{t}_L \tilde{t}_R \tilde{b}_L \tilde{b}_R$	$\tilde{t}_1 \tilde{t}_2 \tilde{b}_1 \tilde{b}_2$
	0	-1	$\tilde{e}_L \tilde{e}_R \tilde{\nu}_e$	same
	0	-1	$\tilde{\mu}_L \tilde{\mu}_R \tilde{\nu}_\mu$	same
Neutralinos	0	-1	$\tilde{\tau}_L \tilde{\tau}_R \tilde{\nu}_\tau$	$\tilde{\tau}_1 \tilde{\tau}_2 \tilde{\nu}_\tau$
	1/2	-1	$\tilde{B}^0 \tilde{W}^0 \tilde{H}_u^0 \tilde{H}_d^0$	$\tilde{\chi}_1^0 \tilde{\chi}_2^0 \tilde{\chi}_3^0 \tilde{\chi}_4^0$
Charginos	1/2	-1	$\tilde{W}^\pm \tilde{H}_u^\pm \tilde{H}_d^\pm$	$\tilde{\chi}_1^\pm \tilde{\chi}_2^\pm$
Gluino	1/2	-1	\tilde{g}	same
Gravitino	3/2	-1	\tilde{G}	same

Table 2.1: Particle content beyond the Standard Model predicted by the MSSM (including the SM Higgs boson H^0). Table adapted from [19].

with quark content $u\bar{u}$ or $d\bar{d}$). This would violate baryon number conservation as well as lepton number conservation. As this decay has not been observed, the proton lifetime is known to be larger than $\mathcal{O}(10^{33}$ years) [38] and thus in some way, baryon and lepton number have to be conserved.

In SUSY models, though, those quantities are violated if no further measures are taken. That is why often a new symmetry called R -parity [39] is introduced as

$$P_R := (-1)^{3(B-L)+2s}$$

where s is the spin of the particles involved in the interaction. It has the advantageous property that each SM particle has even R -parity $P_R = +1$ and each SUSY particle odd R -parity $P_R = -1$. If one then postulates that R -parity is conserved, not only proton decay is prevented because R -parity would need to be violated at the decay's intermediate interactions, but at the same time each interaction must have an even number of SUSY particles. In consequence, the decay chain of each SUSY particle has to end with a lightest supersymmetric particle (LSP) that cannot decay any further without violating R -parity and, thus, is an excellent candidate for dark matter [31, 32]. In the MSSM, the LSP is usually the lightest neutralino, χ_1^0 .

Supersymmetry breaking

One striking drawback when considering SUSY is that its particles should already have been discovered if they were indeed exact copies (excluding the spin) of their SM superpartners: They would not only have the same electric charge, flavour, etc. as the SM particles but also the same mass, allowing them to be observed just like SM particles. As this is not the case, SUSY must be a broken symmetry such that SUSY particles acquire higher masses than their SM superpartners. While SUSY theories can introduce a SUSY breaking term that causes precisely this, the expected mass scale of SUSY particles still is about a few TeV [37, 40, 41], which is in range of today's experiments.

There has not been any sign of SUSY to date, though. Instead, experiments set increasingly strong limits on SUSY particle masses [42, 43], reducing the desirable phase space for possible SUSY particles considerably [44, 45]. At the same time, with increasing mass splitting between SM and SUSY particles, the non-excluded SUSY models yield much less appalling solutions to the hierarchy problem [46].

2.5 Longevity of particles

Indifferent of whether a particle is part of the SM, SUSY or any other BSM theory, its decay is a stochastic process following the function

$$N(t) = N_0 \cdot e^{-\Gamma_{\text{tot}} t}$$

where $N(t)$ is the amount of particles that did not decay after time t and N_0 is the original amount of particles. The total decay rate Γ_{tot} is connected to the mean lifetime τ via

$$\tau = \frac{1}{\Gamma_{\text{tot}}}$$

which usually comes to mind when considering particle longevity. Still, Γ_{tot} is the more handy quantity, as a particle with n decay channels simply acquires the sum of the single decay rates Γ_i as total decay rate:

$$\Gamma_{\text{tot}} = \sum_{i=1}^n \Gamma_i. \quad (2.3)$$

Each single decay rate can be calculated following *Fermi's Golden Rule* for transition rates of a given process

$$\Gamma = \frac{(2\pi)^4}{2M} S \int |\mathcal{M}|^2 \delta^4 \left(P - \sum_{i=1}^n p_i \right) \prod_{i=1}^n \frac{d^3 \vec{p}_i}{(2\pi)^3 2E_i}, \quad (2.4)$$

where M and P are the mass and four-momentum of the decaying particle. p_i and E_i are the four-momentum and energy of the decay products, respectively. S is a statistics factor accounting for identical particles, $|\mathcal{M}|$ the matrix element (also called decay amplitude) characteristic for the decay process. The δ -function ensures four-momentum-conservation. Equations (2.3) and (2.4) nicely show what controls the characteristics of decay rates and therefore particle lifetimes:

- the decay amplitude $|\mathcal{M}|$: Herein, lower decay rates are covered that arise if a soft coupling, i.e., the weak interaction, is responsible for the particle decay. It also accounts for non-existing (low) decay rates if a quantum number has to be conserved (almost conserved).
- the phase space of the decay products $\int \prod_{i=1} d^3\vec{p}_i$.
- the number of different viable decay channels.

Of course, even knowing these mechanisms influencing particle lifetimes, calling a particle "long-lived" is rather ambiguous. As the work at hand is closely connected to particle detectors, it is suggestive to consider longevity compared to the amount of time a particle spends in a detector. Therefore, in the following the term "long-lived" refers to particles that reach (in their mean lifetime) at least the inner parts of the detector. "Detector stable" or short "stable" particles are long-lived particles (LLPs) that traverse the detector completely without decaying. Considering the typical dimensions of a particle detector of $\mathcal{O}(10\text{ m})$, the expected time a stable particle at speed of light c propagates through the detector is $\mathcal{O}(100\text{ ns})$, and of course equivalently longer if the particle is slower than this.

2.5.1 Longevity in the Standard Model

One of the most present stable SM particles is the (free) proton. As already mentioned in Section 2.4.1, its decay, e.g., $p^+ \rightarrow e^+\pi^0$, is prohibited by conservation of lepton and baryon number. This is reflected in equation (2.4) by a decay amplitude $|\mathcal{M}| = 0$ resulting in the aforementioned lifetime larger than $\mathcal{O}(10^{33}\text{ years})$ [38].

Free neutrons n^0 , in turn, can decay into protons: $n^0 \rightarrow p^+e^-\bar{\nu}_e$ (see Figure 2.4a). Given neutrons and protons are almost mass-degenerate ($m_n = 940\text{ MeV}$, $m_p = 938\text{ MeV}$), the corresponding phase space is small resulting in a large lifetime of 880 s [17, p. 94f].

The last example for a stable SM particle that shall be given here is the muon (μ^-), which can decay via $\mu^- \rightarrow W^-\nu_\mu \rightarrow e^-\bar{\nu}_e\nu_\mu$ as shown in Figure 2.4b. It is stable ($\tau = 2.2\ \mu\text{s}$) because on the one hand, it decays via weak interaction, thus lowering the decay amplitude $|\mathcal{M}|$. On the other hand, its decay chain includes a virtual W^+ boson that is much heavier than a muon ($m_W = 80.4\text{ GeV}$, $m_\mu = 106\text{ MeV}$ [17, p. 33ff]) lowering $|\mathcal{M}|$ even further.

2.5.2 Longevity in BSM theories

LLPs emerge in a vast range of BSM theories. In UED, for example, SM particles are accompanied by Kaluza-Klein (KK) excitations from which they are separated by a mass

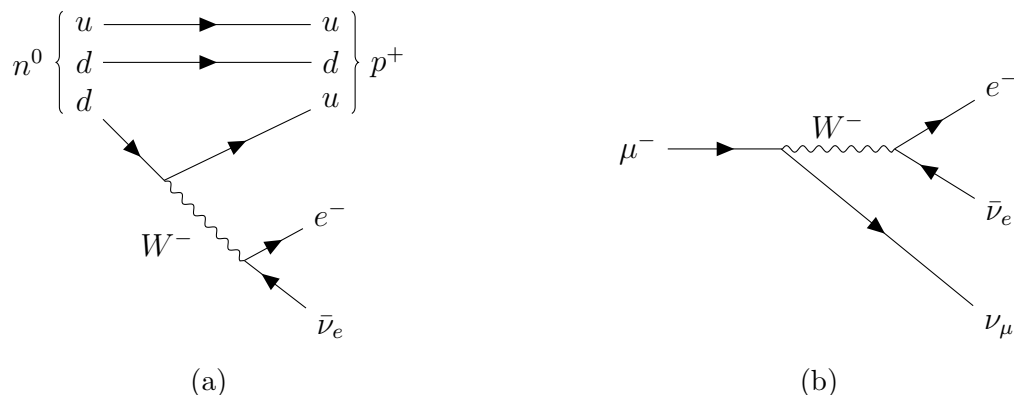


Figure 2.4: Feynman diagram for the decay of a free neutron, n^0 , (a) and a muon, μ^- (b).

gap. Since KK parity — a reflection symmetry about the mid point of the extra dimension — is conserved, the lightest Kaluza-Klein particle (LKP) is long-lived [47].

Dark matter in general, independent of the underlying theory, has to be a stable particle of course. Otherwise, it would decay at a much easier detectable rate, and it could not be so abundant in galaxies in the first place.

In supersymmetric models with R -parity conservation, the LSP — being a promising candidate for dark matter — is stable as its decay would violate R -parity conservation. As a dark matter LSP has to be electrically- and colour-uncharged, the next-to-lightest supersymmetric particle (NLSP) is in many cases more promising for observation: It could be stable if it is only slightly heavier than the LSP, and accordingly the decay phase space is small. In contrast to the LSP, it could at the same time carry colour or electric charge, leaving tracks or a measurable energy deposit in a particle detector (see Chapters 3 and 4). Depending on the SUSY model and breaking mechanism, candidates for colour or electrically charged NLSPs are, for example, stau ($\tilde{\tau}$) and chargino (χ_1^\pm) [48].

Chapter 3

Experimental setup

Before conducting a search for BSM particles, or in particular calibrating a detector for such a search, a deep understanding of the utilised detector is indispensable. For the work at hand, the ATLAS particle detector [49] at the Large Hadron Collider (LHC) [50] is employed, which shall therefore be described in more detail in the following.

3.1 The Large Hadron Collider

The LHC is the world’s most powerful particle collider and is operated by the European Organization for Nuclear Research (CERN) [51]. It is a synchrotron with a circumference of 27 km and is located near Geneva, Switzerland, in a tunnel about 100 m below ground which was previously occupied by the Large Electron–Positron Collider (LEP). As the names say, LEP collided electrons and positrons, while the LHC collides hadrons. More specifically, the LHC does proton–proton (pp) collisions most of the time, which are also the basis of the work at hand. During some special data-taking runs, proton–lead and lead–lead collisions are also conducted.

The choice of pp collisions for the LHC over LEP e^+e^- collisions is motivated by the radiation power of synchrotron radiation, which is proportional to m_0^{-4} [52]. Therefore, it is much more convenient to accelerate protons with mass $m_p = 938 \text{ MeV}$ [17, p. 94] than electrons with mass $m_e = 511 \text{ keV}$ [17, p. 36].

The disadvantage of colliding protons, or hadrons in general, is that they are composite particles. Thus, the constituents of the hadron (valence and sea quarks as well as gluons), referred to as *partons*, do not have a defined momentum. Instead, it is distributed according to parton distribution functions (PDFs). In addition, it is neither clear which partons collided in the first place nor determined that only one parton of each proton interacted. It is the obligation of a prudent analysis to account for this background.

The protons that are collided at the LHC are beforehand passed on by a succession of machines that accelerates them to increasingly higher energies: First, Linac2; secondly, the Proton Synchrotron Booster (PSB); thirdly, the Proton Synchrotron (PS); fourthly,

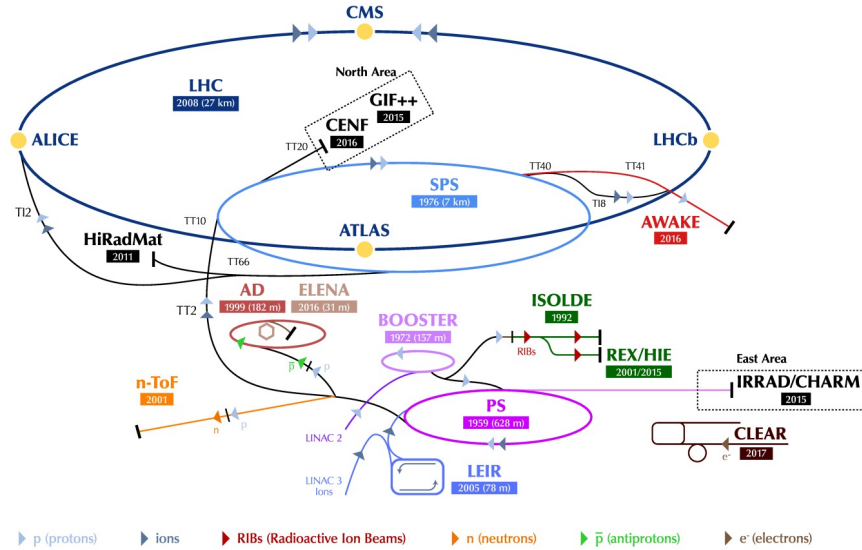


Figure 3.1: The CERN accelerator complex. The acceleration chain for protons is drawn in shades of purple and blue. It ends with the LHC (large dark blue ring). The positions of the four main experiments at the LHC, ALICE, ATLAS, CMS, and LHCb, are marked in yellow. Figure adapted from [53].

the Super Proton Synchrotron (SPS). The LHC is the last accelerator in this chain which is also pictured in Figure 3.1.

It accelerates the protons to their final energy, which varies for the different *operational runs* of the LHC. Operational runs are periods of multiple years that are separated by a shutdown phase for upgrades and maintenance for the accelerators and the various detectors. The first operational run, Run 1, took place from 2009 to 2013 and exhibited centre-of-mass energies \sqrt{s} of the pp -collisions of 7 TeV and 8 TeV. Run 2 takes place from 2015 to 2018 at $\sqrt{s} = 13$ TeV, i.e., 6.5 TeV per proton. The next operational run, Run 3, is currently scheduled for 2021 at the LHC design centre-of-mass energy $\sqrt{s} = 14$ TeV. These centre-of-mass energies are unprecedented for particle colliders, clearly marking the LHC as a collider at the so-called high-energy frontier. In contrast to this, particle colliders at the "precision frontier" like SuperKEKB [54] collide electrons or positrons, which are elementary particles and therefore yield less background.

One single fill with protons that is accelerated and collided at the LHC and, finally, dumped is referred to as *data-taking run*. In the data-taking period 2015 to 2018, there were more than 550 runs with pp collisions suitable for physics analysis recorded with ATLAS. To allow for greater statistics, the LHC is designed for fills which nominally consist of 2808 bunches with 1.15×10^{11} protons each and a temporal spacing of 25 ns [50].

When colliding such enormous amounts of composite particles, the particle collider's ability to produce a desired number of interactions is of peculiar interest. As this is not meaningfully represented in the mere number of particles revolving in the beams of the collider,

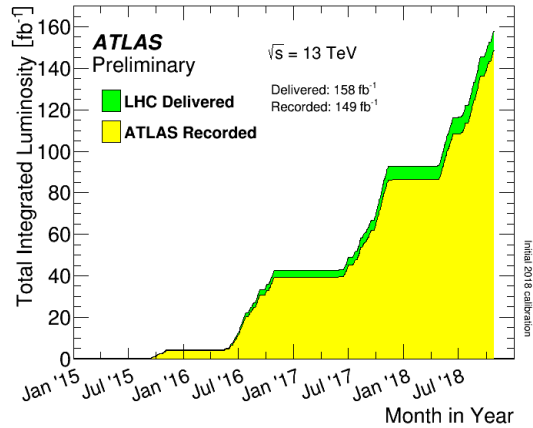


Figure 3.2: Integrated luminosity \mathcal{L} delivered by the LHC and recorded by ATLAS in Run 2 as a function of the date. Figure taken from [56].

instead the *instantaneous luminosity* L given by

$$L = \frac{N_1 N_2 f N_b}{4\pi\sigma_x\sigma_y}$$

is investigated [55]. Hereby, N_1 and N_2 are the number of particles per bunch, revolving in N_b bunches in beams at a revolution frequency f . The beams are assumed to have Gaussian profiles with widths σ_x and σ_y in x - and y -direction, respectively. The nominal instantaneous luminosity for the LHC is as high as $10^{34} \text{ cm}^{-2} \text{ s}^{-1}$ [50], but even this is exceeded on a regular basis, e.g., with instantaneous luminosities up to $2.1 \times 10^{34} \text{ cm}^{-2} \text{ s}^{-1}$ in 2018 [56]. The *integrated* luminosity

$$\mathcal{L} = \int L dt$$

can be used for calculating the expected number of events N_x of a certain process x during data-taking as

$$N_x = \sigma_x \cdot \mathcal{L},$$

whereby σ_x is the interaction cross section.

Figure 3.2 shows how the delivered integrated luminosity of the LHC increased with time. It resulted in an integrated luminosity for the data-taking period Run 2 in 2015–2018 recorded by ATLAS in pp collisions of $\mathcal{L} = 149 \text{ fb}^{-1}$.

There are in total seven experiments at the LHC. TOTEM (TOTAL Elastic and diffractive cross-section Measurement) aims, as the name already implies, at measuring elastic scattering and diffractive processes as well as total cross sections. LHCf (Large Hadron

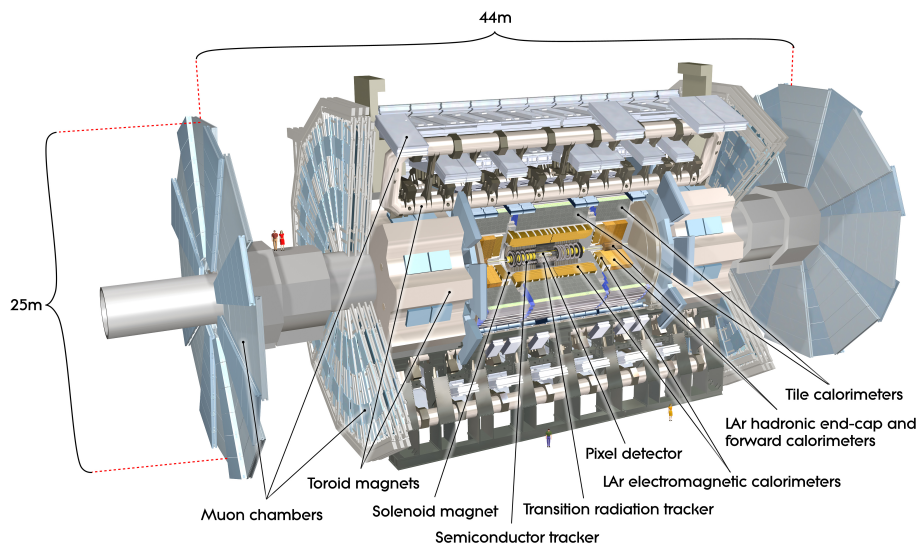


Figure 3.3: Cutaway drawing of the whole ATLAS detector. All subsystems are labelled. Figure taken from [57].

Collider forward) simulates cosmic rays in laboratory conditions by the particles thrown forward by collisions. MoEDAL (Monopole and Exotics Detector at the LHC) searches for hints of New Physics that might manifest themselves in highly ionising particles like magnetic monopoles.

The other four experiments are the main experiments at the LHC, and are marked in Figure 3.1. LHCb (Large Hadron Collider beauty) focusses on bottom (also called "beauty") quarks and antibottom quarks. Differences in the decays of quarks and antiquarks might give hints for CP -violation and the origin of the matter–antimatter asymmetry. ALICE (A Large Ion Collider Experiment) uses the heavy-ion runs of the LHC, measuring the properties of strongly interacting matter that can then form quark–gluon plasma. The last two, CMS (Compact Muon Solenoid) and ATLAS, are multi-purpose particle detectors aiming at tracking, identifying and measuring the properties of all particles emerging from a collision. This allows studying the Standard Model as well as searching for New Physics.

3.2 The ATLAS experiment

ATLAS is built of many layers concentric to the interaction point (IP). Those in the central region (referred to as *barrel*) are parallel to the beam pipe as indicated in Figure 3.3. The outer parts of the detector (*end-caps*) are perpendicular to it.

A particle emerging from a collision first has to pass the Inner Detector (ID) where, in presence of a strong magnetic field, its trajectory is bent according to its charge and mo-

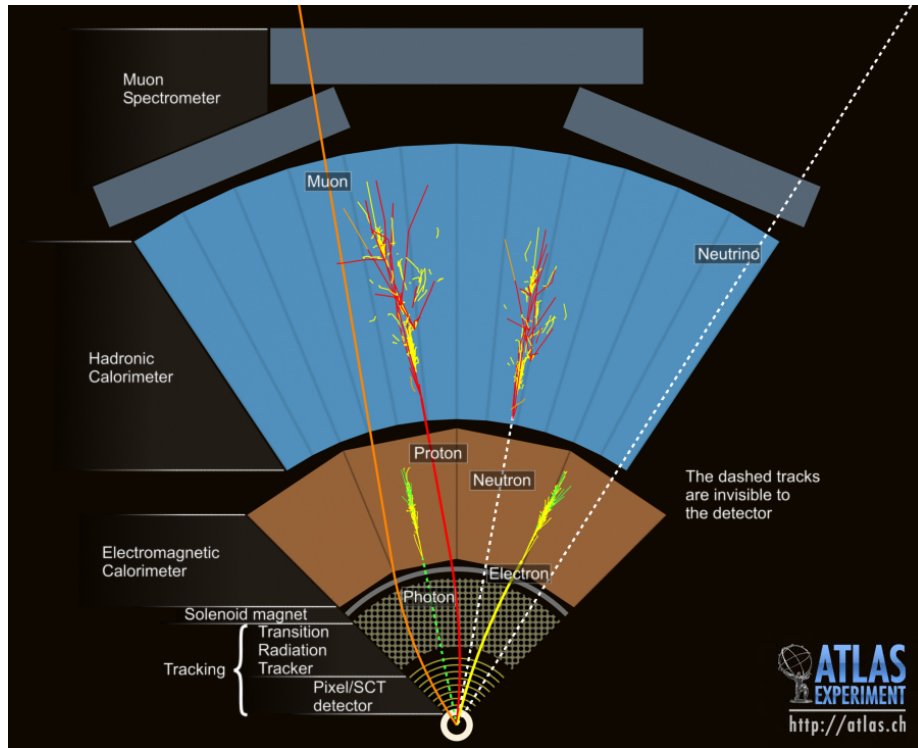


Figure 3.4: Schematic cross section of the ATLAS detector with tracks left by different types of SM particles drawn in. Figure taken from [57].

momentum. Afterwards, the particle reaches the electromagnetic calorimeter where the energy deposit of electromagnetically interacting particles is measured. Light electromagnetically interacting particles (i.e., electrons, positrons and photons) deposit all of their energy. Heavier electromagnetically interacting particles and particles without electric charge can pass it and enter the hadronic calorimeter. Here, colour charged particles deposit all of their energy, leaving collimated tracks in a cone that is called *jet*. Jets cannot be matched to a specific quark or gluon taking part in the collision as those immediately *hadronise*, i.e. form hadrons, after the collision. Due to their longer lifetimes and higher mass compared to other quarks, it is — with respectable effort — possible to identify which jets contained *b* quarks, though.

SM particles passing the hadronic calorimeter are either muons or neutrinos. Muons can be identified in the muon spectrometer where they leave bent tracks due to their charge and another magnetic field. Neutrinos interact too weakly to be measurable with the detector at all. A schematic overview of the kind of tracks SM particles leave in ATLAS is also given in Figure 3.4.

Even if a neutrino or a very weakly interacting, non-SM particle like dark matter does not leave a track or measurable energy deposit within the detector, it is possible to get hints for it, though: As the proton–proton collisions take place head-on in the IP, the total

momentum perpendicular to the beam pipe of all produced particles, the *transverse momentum* p_T , has to be zero if momentum is to be conserved. Therefore, *missing* transverse momentum, which can be calculated according to

$$\vec{p}_{T,\text{miss}} = - \sum \vec{p}_{T,i}, \quad (3.1)$$

indicates the momentum of at least one particle that escaped the detector unobserved. Hereby, $\vec{p}_{T,i}$ are the momenta of the observed particles. The magnitude of the missing transverse momentum, referred to as E_T^{miss} , is therefore an important quantity for identifying neutrinos or BSM particles.

As for many physical quantities, like p_T , a Cartesian coordinate system using x , y and z is of limited use, in ATLAS an additional dedicated coordinate system is used that, i.a., exploits the cylindrical symmetry of the detector. The origin of both coordinate systems is the IP in the centre of the detector.

In the ATLAS Cartesian coordinate system, the x -axis points towards the centre of the LHC ring, the y -axis upwards. The z -axis points tangential along the beam pipe such that a right-handed coordinate system is formed. This is also depicted in Figure 3.5a.

The coordinate system used besides (x, y, z) in ATLAS is based on the (r, ϕ, η) coordinate set. $r := \sqrt{x^2 + y^2}$ is the distance in the transverse plane to the IP. ϕ is the polar angle in transverse plane, i.e., the azimuthal angle along the beam pipe: $\phi := \arctan\left(\frac{y}{x}\right)$, $-\pi \leq \phi < \pi$. In spherical coordinates, $\theta := \arccos\left(\frac{z}{r}\right)$, $0 \leq \theta < \pi$ would be the third coordinate. In practice, the pseudorapidity $\eta := -\ln \tan\left(\frac{\theta}{2}\right)$ turns out to be more convenient, though, as particle production is approximately constant as a function of η and differences in η are invariant under boosts in z -direction. Exemplary values for η in dependence of θ are given in Figure 3.5b.

The introduction of a coordinate system also allows the nominal separation between *side A* ($\eta > 0$) and *side C* ($\eta < 0$) of the ATLAS detector [58].

As was already mentioned in the previous section, the LHC runs with an immense amount of protons per bunch and a considerably small bunch spacing to allow for greater statistics. The negative aspect is, this leads to a background for analyses called *underlying event*. Underlying events are subdivided into *in-time pile-up* and *out-of-time pile-up*.

In-time pile-up is a result of the immense amount of protons per bunch: When a certain signature of an event like multiple jets is registered within an analysis, it has to be verified that the origin of the signature is really one single parton–parton interaction and not just resulting as a sum of simultaneously happening collisions.

In difference to this, *out-of-time pile-up* arises because of the bunch spacing of merely 25 ns: As shortly mentioned in Section 2.5, the time a particle propagates through the detector can reach 100 ns, even at the speed of light. In addition, time elapses between interactions of the particle with the detector and the signal of these reaching the readout. This time span can, for example, exceed 600 ns in the monitored drift tubes (MDTs). Fortunately, most of this can be taken into account during reconstruction.

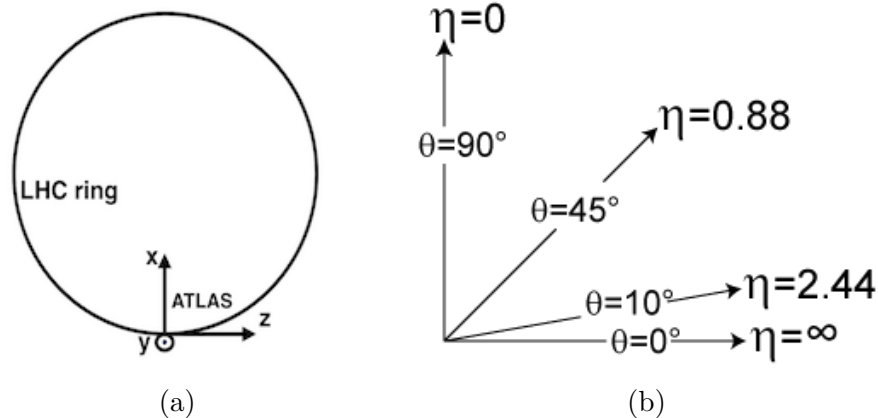


Figure 3.5: (a) Definition of ATLAS' Cartesian coordinate system. (b) Exemplary values for η in dependence of θ . Figures taken from [59].

Another consequence of the tight bunch spacing of 25 ns, i.e., a proton–proton collision frequency of 40 MHz, is the vast amount of data arising. As it is not possible to record all this data at full rate, a two-level trigger system is introduced. The low-level, Level-1 (L1) trigger is hardware based, while the High-level Trigger (HLT) is software based [60]. Both reduce the rate at which data has to be written into storage by analysing and identifying signatures and accepting only those that fulfill previously defined selection criteria. The L1 trigger is able to reduce the rate from 40 MHz to about 100 kHz. The HLT then reduces it further to a recordable rate of approximately 1 kHz [61].

In the following sections, the working principles of ATLAS' various subdetectors shall be discussed in more detail.

3.2.1 Inner Detector

The aim of the Inner Detector is to allow tracking of particles originating from the IP as well as vertex reconstruction with high efficiency and precision [62]. For this, it is enclosed in a magnetic field with central flux density 2 T, bending electrically charged particles, and thus allowing for momentum measurement from the track curvature. Vertex reconstruction is necessary to identify displaced vertices, which is evidence of a long-lived particle. In addition, high precision track reconstruction allows to reveal spatial differences between the primary decay vertex (PV) and the IP, which is crucial for identifying jets from b quark hadronisation [63].

To optimally fulfill the demands for efficiency and precision as well as keep a reasonable cost, the ID is made up of three different subdetector systems, covering the region $|\eta| < 2.5$.

The innermost subdetector system is a semiconductor pixel detector, or short pixel detector. With a resolution in the r – ϕ -plane of $12 \mu\text{m}$ and $66 \mu\text{m}$ in z -direction for the barrel

($77\ \mu\text{m}$ in r -direction for the end-caps), it allows for highest granularity and highest precision. It consists of four layers, the innermost of which — the Insertable B-Layer (IBL) at an average radius of 3.3 cm from the beam pipe — was only inserted in the maintenance and upgrade phase 2013–2015 [64]. The outermost barrel layer of the pixel detector is at about 14 cm.

As the pixel detector is the subdetector closest to the interaction point and has a high energy resolution, it is well suited for ionisation energy loss (dE/dx) measurements that can be used for searches for charged stable massive particles as shall be discussed in Chapter 4.

The ID's intermediate subdetector system is the semiconductor tracking detector (SCT). The SCT is made up of four layers of silicon microstrip detectors with a resolution of $16\ \mu\text{m}$ in the r - ϕ -plane, but a considerably lower resolution of $580\ \mu\text{m}$ along the z -axis (r -axis) for the barrel region (end-caps).

The outermost subdetector system of the ID is the transition-radiation tracker (TRT), which is made of straws with a spatial resolution of $170\ \mu\text{m}$ each. The TRT is the largest of the ID subdetector systems, reaching outward to about $r = 108\ \text{cm}$. It is therefore a compromise between precision and cost reduction, yielding an average of 36 hits per track [62].

3.2.2 Calorimeters

Particles passing the Inner Detector reach the calorimeters where *absorber* material is located. This causes intensive particle interactions — pair-production, photoelectric effect and Compton-scattering for photons as well as bremsstrahlung for electrons and positrons —, resulting in so-called *electromagnetic showers*. As the energies of the interacting particles decrease, eventually all particles of the shower are absorbed. To detect the interactions, *active materials* are installed in calorimeters that measure the deposited energy.

Hadronic showers are similar to electromagnetic showers only that they occur as a result of strong interactions. Those showers are wider, longer and start later, making a dedicated detector setup necessary. In ATLAS, there are therefore two distinct types of calorimeters: the electromagnetic calorimeter and the hadronic calorimeter.

The electromagnetic calorimeter is the one directly surrounding the Inner Detector. It uses liquid argon (LAr) as active material and lead as the absorber. It covers the region $|\eta| < 3.2$ and has a maximum radius of 2.2 m [65].

The hadronic calorimeter in the η -region $1.4 < |\eta| < 4.8$ also uses LAr as active material but copper as absorber. For the central region a different setup is used: For $|\eta| < 1.7$, the *tile calorimeter* is installed, consisting of scintillating tiles as active material and steel as absorber. It has a maximum radius of 4.2 m [66]. An overview of the ATLAS calorimeters is shown in Figure 3.6.

The ATLAS calorimeters are specifically designed for good timing resolution and fast readout, which allows to trigger on electrons, photons, jets and E_T^{miss} . The timing resolution

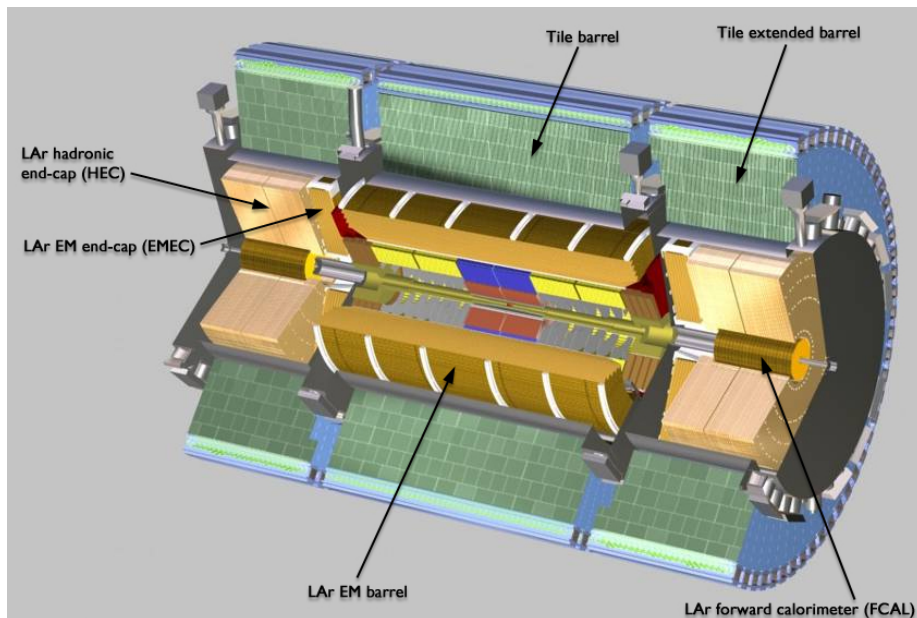


Figure 3.6: Cutaway view of the ATLAS calorimeters. Figure taken from [57].

thereby has to be good enough to resolve different bunch crossings.

3.2.3 Muon spectrometer

As the interaction of muons in the calorimeters is, due to their large mass and missing colour charge, too weak to cause showers, they propagate into the outer parts of the detector, the muon spectrometer (MS). Here, strong magnetic fields again bend the trajectory of electrically charged particles, i.e., only muons in the Standard Model at this stage.

The ATLAS muon spectrometer is designed in a twofold way: On the one hand, systems with high timing resolution and fast readout to allow triggering on tracks. On the other hand, high-precision tracking chambers which allow accurate track reconstruction and reliable momentum measurement.

The trigger systems are the resistive-plate chambers (RPCs) in the barrel region and the thin-gap chambers (TGCs) in the end-caps (compare Figure 3.7). TGCs are similar to multiwire proportional chambers (MWPCs): A particle passing a chamber ionises a gas, resulting in an ionisation cascade that is collected in a close-by wire, causing an electric signal. The ATLAS TGCs use a CO_2 - n -pentane gas mixture [68], allowing a chamber timing resolution of 4 ns. In addition to allowing for triggering due to the short drift times of electrons to the wires, the TGCs also complement the position measurements of the high-precision tracking chambers. They achieve a spatial resolution of less than 6 mm in r and less than 7 mm in ϕ [49].¹

¹Values stated for resolution in this chapter are always root mean square (RMS) values.

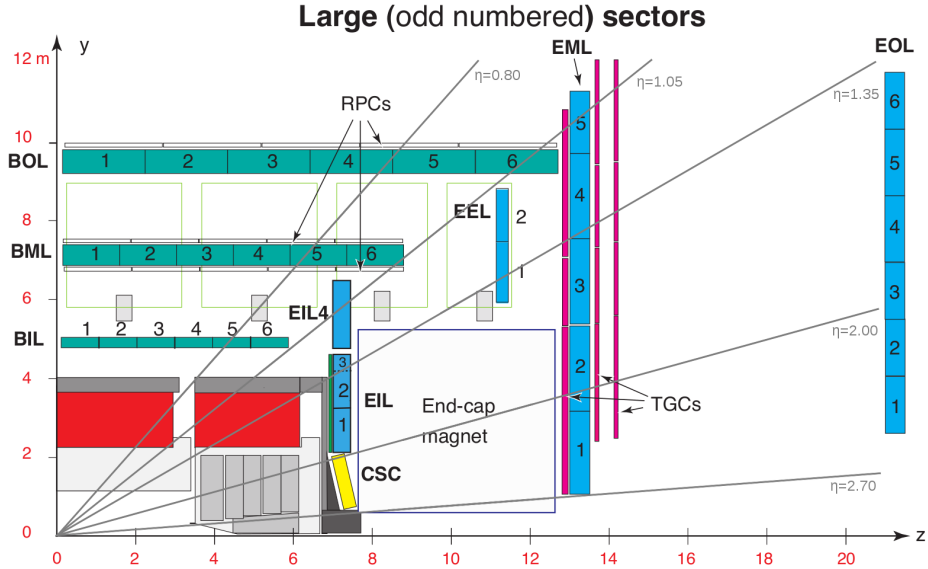


Figure 3.7: Cross-sectional view of the ATLAS muon spectrometer for the large sectors in a plane containing the beam axis. MDTs are drawn in blue (end-caps) and turquoise (barrel), respectively. Figure adapted from [67].

As RPCs are one of the two systems whose calibration the work at hand is focused on they are described in more detail in a later paragraph of this section.

The high-precision tracking in ATLAS is mostly done by monitored drift tubes (MDTs), which also are discussed in more detail in a later paragraph of this section. Due to their large diameter and high operating pressure, MDTs are not well-suited for areas with an expected high counting rate, though [68]. As this is the case for $|\eta| > 2$ in ATLAS, they are replaced by cathode-strip chambers (CSCs) there. CSCs are MWPCs with a wire spacing of 2.54 mm and the same distance between wire and cathode. They are filled with an Ar-CO₂-CF₄-mixture and yield a timing resolution of 3.6 ns as well as a spatial resolution of 40 μm in the bending direction. In the azimuthal direction, their resolution of 5 mm is considerably worse [68].

The muon spectrometer as the outermost shell of ATLAS ultimately also defines its dimensions, being 46 m in length and 25 m in diameter. Following the eight-fold ϕ -symmetry of the bending magnets, the muon spectrometer is divided into 16 *sectors*: 8 large and 8 small ones (also referred to as "long" and "short") as shown in Figure 3.8.

Chambers in the barrel are arranged in *detector layers* at approximately $r = 5$ m, 7.5 m and 10 m. In the end-caps, they form four layers at $|z| \approx 7.4$ m, 10.8 m, 14 m and 21.5 m. There are gaps in the barrel detector layers and therefore acceptance at $|\eta| \approx 0$ as well as at $\phi \approx 1.3$ and 1.9. This is unavoidable to allow for maintenance service and the detector feet, respectively.

For nominal clarity, the ATLAS muon spectrometer is divided into different *stations* in

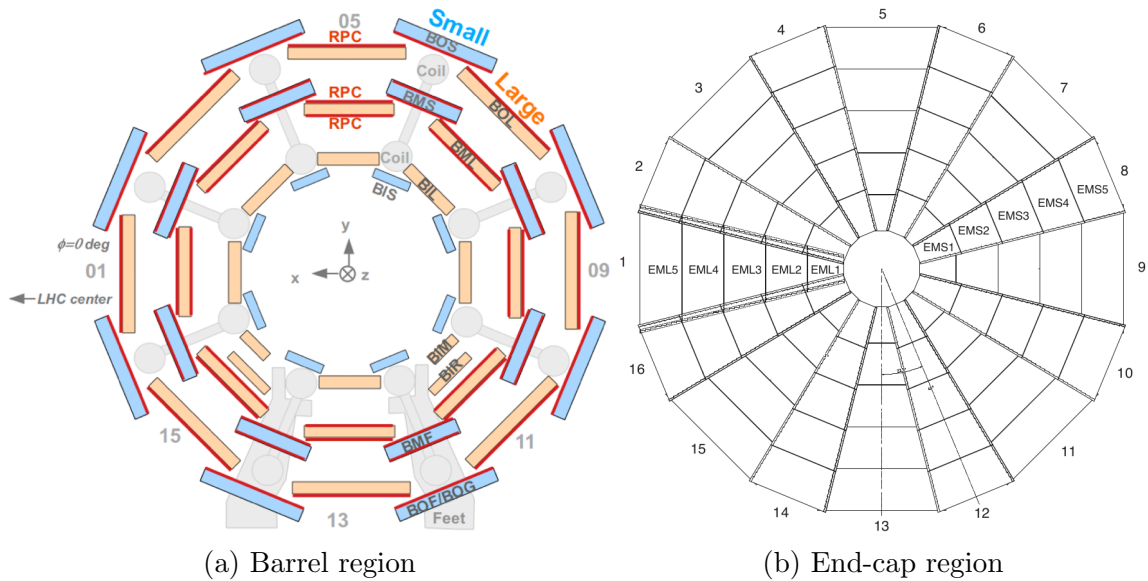


Figure 3.8: (a) Cross-sectional view of the MS barrel region perpendicular to the beam axis. MDTs in small sectors are drawn in blue, in large sectors in orange. RPCs are shown in red and magnetic coils and feet in grey. Figure taken from [69]. (b) Sketch of the MS end-cap chambers. Figure taken from [68]. In both figures, the view is from the IP onto side A and station names as well as sector numbers are given.

which chambers exhibit similar properties. Abbreviations for those consist of three characters, which are explained in Table 3.1.

Monitored drift tubes

The basic elements of MDT chambers are *tubes*. In those, like in MWPCs, the tube wall serves as cathode and a central wire as electron-collecting anode as shown in Figure 3.9. In contrast to MWPCs, MDT tubes have a circular cross section giving rise to a radial electric field, which simplifies position measurements. On the other hand, this is complicated by MDT tubes being operated with pressurised Ar-CO₂ gas (93/7 at 3 bar), which has a highly non-linear space-drift-time-relation as indicated in Figure 3.10. Due to their large diameter of 29.970 mm, the drift times of electrons in MDT tubes can become as high as 700 ns.

Tubes that are in the same plane of an MDT chamber are considered a *tube layer*. Multiple tube layers are then grouped into *multi-layers*. Two of those — separated by a mechanical spacer — form the MDT chamber itself. A multi-layer consists of four tube layers in the innermost detector layer of the muon spectrometer and of three layers everywhere else. The complete layout of an MDT chamber is sketched in Figure 3.11. The readout of MDT chambers is in general located at their large- ϕ end in the small sectors and at their small- ϕ end for large sectors [67].

	Character	Meaning
1. Region	B	Barrel
	E	End-cap
2. Layer	I	Inner
	M	Middle
	O	Outer
3. Sector	E	Extra
	L	Large
	S	Small
	F/G/H	Feet

Table 3.1: Naming scheme of stations in the ATLAS muon spectrometer.

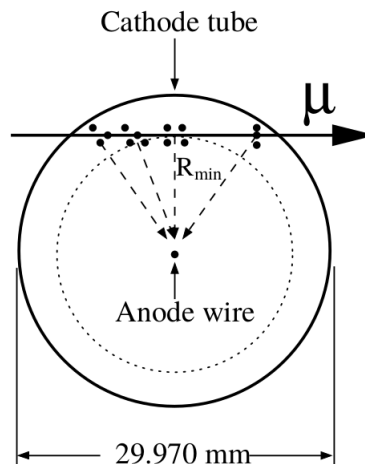


Figure 3.9: Cross section of an MDT tube. Shown is also the ionisation caused by a passing muon. R_{\min} is the distance of closest approach of the muon to the anode wire. Figure adapted from [49].

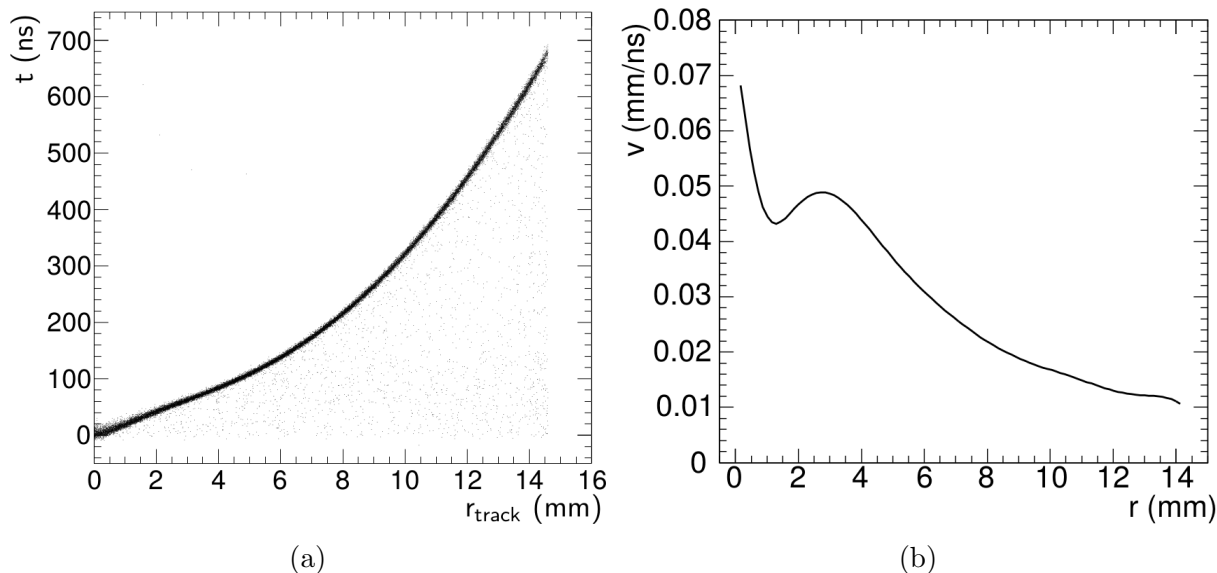


Figure 3.10: (a) Drift times t of electrons in MDT tubes caused by traversing muons as a function of the muons' distance r_{track} from the wire. (b) Electron drift velocity v in MDT tubes as a function of the drift radius r . Figures taken from [70].

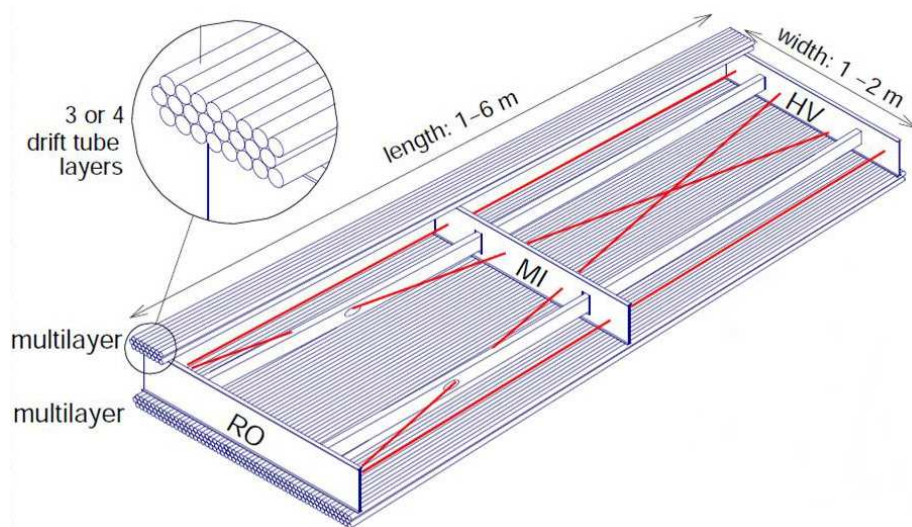


Figure 3.11: Overall layout of an MDT chamber. Figure taken from [49].

With this setup, MDT chambers deliver about 20 hits per track and achieve a resolution of $35 \mu\text{m}$ in r -direction (z -direction) in the barrel (end-caps). MDT tubes exhibit a timing resolution of about 3.4 ns if calibrated correctly, as will be shown in Chapter 5.

In total, there are 1,150 MDT chambers and more than 359,000 MDT tubes installed in the ATLAS detector.

Resistive-plate chambers

In the barrel region, RPC chambers are mounted onto the MDT chambers. Thereby, two chambers are placed on the surface of MDT chambers in the middle detector layer and one on MDT chambers in the outer detector layer. The exact positioning can be seen in Figures 3.7 and 3.8a. RPCs are gaseous parallel electrode-plate detectors, i.e., in contrast to all other detector systems in the ATLAS muon spectrometer, they do not have wires. Instead, the charge avalanches caused by ionising tracks are collected at the electrodeplates directly. The signal is read out by pick-up strips in η - and ϕ -direction, accordingly referred to as η - and ϕ -strips. Each RPC *gas gap*² is confined by two resistive plates and their pick-up strips, each RPC *unit* consists of two independent gas gaps. This layout is also drawn in Figure 3.12.

In ϕ -direction, as is sketched in Figure 3.13, two units are assembled together to form a *module*. This allows for a homogeneous trigger scheme for all chamber types and gives rise to the fact that there are about twice as many ϕ -strips as η -strips.

In z -direction on the other hand, two modules are assembled together forming a *chamber*. All in all, 606 such chambers are installed in ATLAS, containing more than 376,000 strips in total. Each of those strips has a spatial resolution of 10 mm and a nominal timing

²In the literature, gas gaps are also called *layers*. For nominal clarification between these components of RPCs and the inner, middle and outer *detector layers*, the term "gas gap" is used in this work.

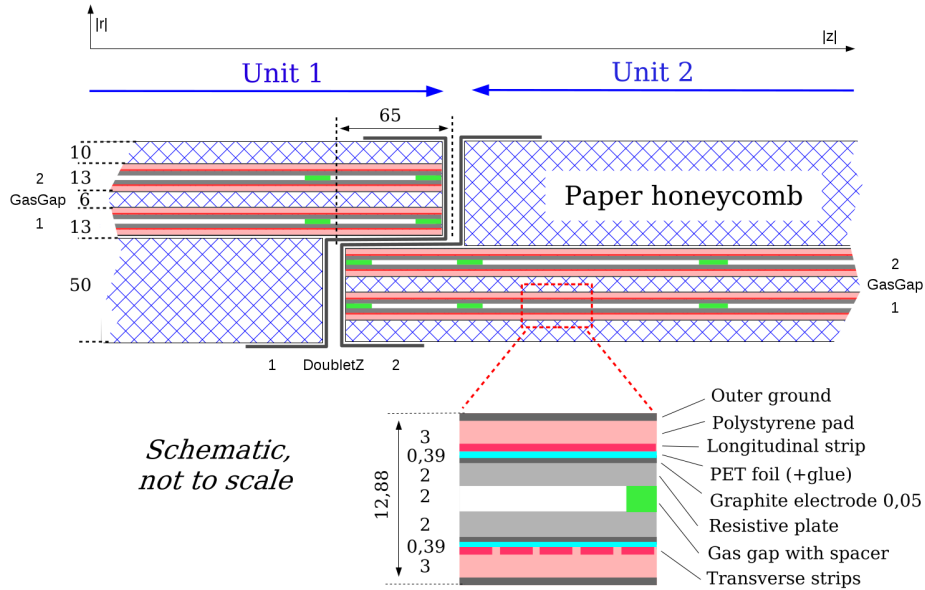


Figure 3.12: Cross section of RPC modules and the way those are assembled together in $|z|$ -direction to form a chamber. Measures are given in mm. Figure adapted from [67]. The scheme for identifying RPCs by the variables DoubletR, DoubletZ, DoubletPhi and GasGap can be found in [58]. Not shown here are the variables DoubletR, which discriminates the two RPC chambers mounted onto the same MDT chamber in $|r|$, and DoubletPhi, which discriminates the two units of one RPC module in ϕ .

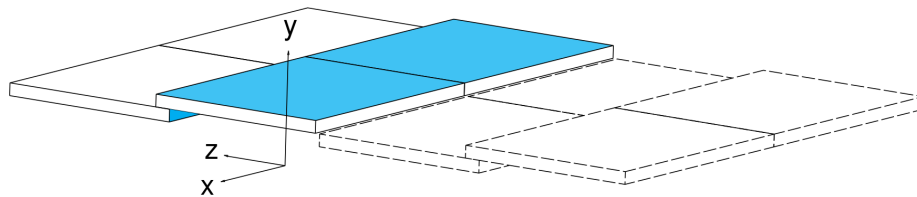


Figure 3.13: Sketch of the way adjacent RPC chambers (one drawn in solid line, the other one dashed) are segmented into two modules each in z -direction and those again are segmented into two units each in ϕ -direction. Figure taken from [68].

resolution of 1.5 ns.

Taking the three different detector layers in which RPCs are mounted on MDTs (2x middle, 1x outer) and the up to four measurements per RPC unit into account, the RPC system yields six or twelve measurements per track, depending on whether measurements of one unit are clustered or treated separately (see also Section 5.3).

As the ATLAS trigger logic works at 320 MHz, RPCs are read out in distinct temporal intervals of 3.125 ns, i.e., eight times per bunch crossing [71]. This intrinsic timing-granularity for RPCs is also visible in RPC timing measurements and has to be accounted for during the calibration procedure.

Chapter 4

Searches for charged stable massive particles with ATLAS

There are many different ways in which BSM physics could be observed with the ATLAS detector. Measurements of SM parameters constantly test SM predictions [72–74] and, if the predictions are significantly contradicted, they could give hints on BSM physics. When observing an excess over the estimated background, searches for model-dependent decay signatures of BSM particles, e.g., top-quark pairs [75], tau pairs [76] or multiple leptons [77], could tip off the existence of immediately decaying BSM particles. Long-lived BSM particles are expected to interact more directly with the detector and yield a handle for a more model-independent approach: If they reach the Inner Detector before decaying, they could be observed, e.g., due to disappearing tracks [78] or displaced vertices [79]. If they exist, particles with even larger lifetimes that fulfill the longevity criterion defined in Section 2.5, i.e., stable particles, could even deposit energy in the calorimeters and leave tracks in the muon spectrometer. One type of search ATLAS conducted for stable particles also requires them to be charged and massive [80–82]. These searches shall be examined in this chapter.

4.1 Observables

It is appealing to search for stable massive particles (SMPs) that are charged as they leave a signature in the detector distinct from every SM particle: Due to their high mass, they are expected to suffer large ionisation energy losses in the ID. In addition, they would exhibit a velocity significantly lower than the speed of light, the velocity Standard Model particles are expected to obtain. Hence, a large time difference between expected time of arrival and actual particle–detector interaction can be measured, especially in the outer parts of the detector. There is no SM process with the same signature and therefore the only background for such an analysis is detector mismeasurements.

The ID is well suited for ionisation energy loss (dE/dx) measurements as it is the detector

closest to the IP. Therefore, particles do not undergo interactions with the detector material before reaching the ID. The pixel detector is the preferred subdetector in the ID for dE/dx measurements for those searches, as its dE/dx resolution is much higher than that of the TRT. The SCT, in contrast, does not provide a dE/dx measurement at all. In addition, with a width of less than 15 cm of the pixel detector, particle trajectories through the subdetector are short and interactions along it are therefore expected to be almost uniform. The mean ionisation energy loss of a particle with energy E and charge z travelling a distance x into a material is, according to Bethe's formula [83],

$$\left\langle \frac{dE}{dx} \right\rangle = -\frac{4\pi}{m_e c^2} \cdot \frac{nz^2}{\beta^2} \cdot \left(\frac{e^2}{4\pi\epsilon_0} \right)^2 \cdot \left[\ln \left(\frac{2m_e c^2 \beta^2}{I \cdot (1 - \beta^2)} \right) - \beta^2 \right]. \quad (4.1)$$

Hereby, n is the electron density of the material and m_e and e are the rest mass of electrons and their charge, respectively. I denotes the mean excitation potential. In addition, the usual substitution in relativistic physics, $\beta := v/c$ with v the particle's velocity and c the speed of light, is used.

The pixel detector yields typically only one measurement per layer, i.e., four measurements, of the ionisation energy. Thus, an averaging of the available dE/dx measurements would give the most probable value (MPV) for dE/dx . As dE/dx is known to be Landau distributed, the MPV differs from the mean given by equation (4.1). In consequence, an empiric *parametric* Bethe formula that is merely oriented by equation (4.1) and gives the MPV of dE/dx ,

$$\text{MPV}_{dE/dx} = \frac{A}{(\beta\gamma)^C} + B, \quad (4.2)$$

is used for connecting the measured ionisation energies with the particle's velocity [84]. Hereby, A , B and C are factors determined by measurements and γ is the Lorentz factor $1/\sqrt{1 - \beta^2}$. As in equation (4.2) $\text{MPV}_{dE/dx}$ of a particle depends on its velocity β , reciprocally, β can be determined from a given $\text{MPV}_{dE/dx}$. To ensure that the mean of the ionisation energy measurements gives a good estimate of $\text{MPV}_{dE/dx}$, it is calculated *truncated*, by disregarding the highest dE/dx measurement. This reduces the impact of the tails of the Landau distribution.

Using an orthogonal approach, β can also be estimated by time-of-flight measurements. Hereby, the fact is exploited that, given the same energy and momentum, a particle with high mass propagates slower through the detector than a particle with low mass. In practice, this means a particle with low β will arrive later at a point in distance d to the IP than a particle with $\beta \approx 1$. In consequence, if a temporal difference t_0 between the expected time of flight ToF_e with $\beta = 1$ and the actual time of flight ToF_a ,

$$t_0 = \text{ToF}_a - \text{ToF}_e = \text{ToF}_a - \frac{d}{c}, \quad (4.3)$$

is measured, the particle's velocity can be calculated according to

$$\beta = \frac{d}{\text{ToF}_a} \cdot \frac{1}{c} = \frac{d}{(\text{ToF}_e + t_0) \cdot c} = \frac{d}{d + t_0 \cdot c}. \quad (4.4)$$

Due to their large acceptance, available timing information and good timing resolution, supported by a low ratio of measurement uncertainty to numerical value of timing measurements as a result of the large distance from the IP, the tile calorimeter as well as MDTs and RPCs in the muon spectrometer are best suited for t_0 and thereby β measurements in ATLAS.

The rest mass m_0 of an SMP whose velocity β was determined by at least one of the methods described above can then simply be calculated from the relativistic formula [85]

$$m_0 = \frac{p}{\beta\gamma}.$$

For this, also the momentum p has to be determined by various measurements in the ID and MS, of course.

To better understand and estimate properties of charged SMPs, especially when considering the above observables, it is essential to conduct simulations of them. These simulations, called *Monte Carlo (MC) simulations* [86], give rise to *truth information*, the underlying properties of the simulated particles. This can be used to test reconstruction as well as analysis techniques. The MC events used in the following are simulated stable staus and charginos. For a more detailed discussion of the simulated events used for this work see Section 5.1.

4.2 Reconstruction

The only electrically charged stable particle in the Standard Model that escapes the calorimeters and reaches the muon spectrometer is the muon, as explained in Section 2.5 and Chapter 3. Charged BSM SMPs could also reach the muon spectrometer and leave a signature in the detector similar to that of a muon. More precisely, the only difference in their MS signatures is the lower velocity of SMPs, which could therefore be described as "slow muons".

In the computational reconstruction process of ATLAS, different algorithms take the interactions registered by the various ATLAS subdetectors as input and try to reconstruct trajectories and properties of the particles that caused the detector signal.

As the purpose of ATLAS is to detect as many particles emerging from a collision as possible, a number of algorithms are run during computational reconstruction aiming at identifying muons. Registered particle–detector interactions, called *hits*, in the muon spectrometer are most certainly caused by muons. Therefore, most of those reconstruction

algorithms start by fitting a track to the muon spectrometer hits [87, 88]. Those tracks are then extrapolated towards the IP to also assign hits in the ID and calorimeters correctly to the muons. There are other reconstruction algorithms, though, which start reconstruction in the ID [89] or in the calorimeters [90].

During nominal reconstruction, the results of the various muon reconstruction algorithms are combined to achieve the best possible accuracy for the muon candidate. Depending on their reconstruction quality, e.g., number of hits and χ^2 of the track fit, muons are assigned a *loose*, *medium* or *tight* quality label.

In the following, reconstruction efficiencies of algorithms are investigated. Although it is suggestive, the term "reconstruction efficiency" is in fact ambiguous: The comparison always takes place between candidates of one source with candidates of a second source that is considered more reliable, of course. Nevertheless, there might be multiple, more reliable sources available. On the one hand, when examining muons not reconstructed by the nominal muon reconstruction algorithms, comparing to those can be sensible. In this case, usually medium-quality muons are used. On the other hand, if truth information is available, this is naturally a very reliable candidate source.

For comparing two sources, candidates of the first source are always *matched* to the particle of the second source with minimal differing track orientation in this work. This is called ΔR -matching, whereby $\Delta R := \sqrt{(\Delta\eta)^2 + (\Delta\phi)^2}$. Here, $\Delta\eta$ is the difference in η of the two candidates and $\Delta\phi$ the difference in ϕ .

4.2.1 Need for a dedicated reconstruction algorithm

Although charged SMPs leave signatures similar to that of muons in the detector, their slowness is a major drawback during reconstruction: As shown in the bottom plot of Figure 4.1, ATLAS' nominal muon reconstruction algorithms lose efficiency with decreasing particle velocity β . There are two main reasons why this is the case [91].

On the one hand, delayed hits might be associated to the wrong bunch crossing (BC), worsening the track fitting or outright preventing it. If trigger information is lost this way, the precision in reconstruction is especially reduced since MDTs have a much lower ϕ resolution than RPCs and TGCs, and therefore almost no ϕ information is available during reconstruction.

On the other hand, due to the late arrival of the particle, the drift radii appear larger. Hence, the nominal muon reconstruction algorithms can cause wrongly fitted tracks, as indicated in Figure 4.2.

This loss of efficiency for low β in the nominal muon reconstruction is in general not a problem as muons have velocities close to the speed of light. For reconstructing charged SMPs, though, a dedicated reconstruction algorithm is clearly needed since their velocity β can be significantly lower than one, as can be seen in the top plot of Figure 4.1. In ATLAS, this dedicated reconstruction algorithm is called MUGIRLSTAU; later on it was renamed MUGIRLLOWBETA. MUGIRLSTAU applies a number of techniques different from those of

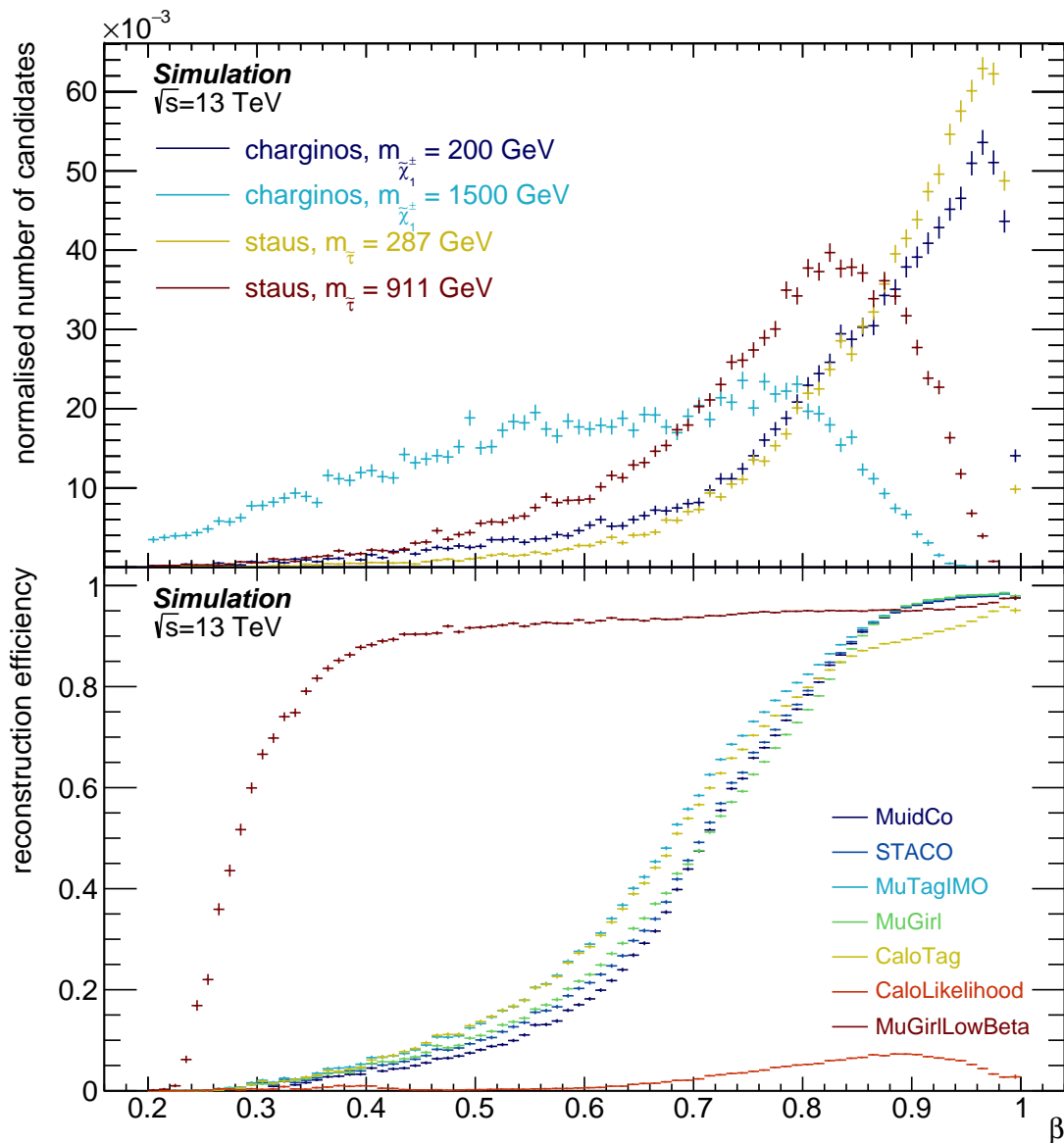


Figure 4.1: Top: β distribution for pair-produced stable charginos and staus of various masses. Bottom: Reconstruction efficiency for signal particles as a function of β for different ATLAS muon reconstruction algorithms. Particles have to fulfill the selection criteria $p_T > 35$ GeV and $|\eta| < 2.5$ and are matched to truth. They count as reconstructed by an algorithm if the algorithm is one of their authors. Reconstruction algorithms without significant contribution have been omitted.

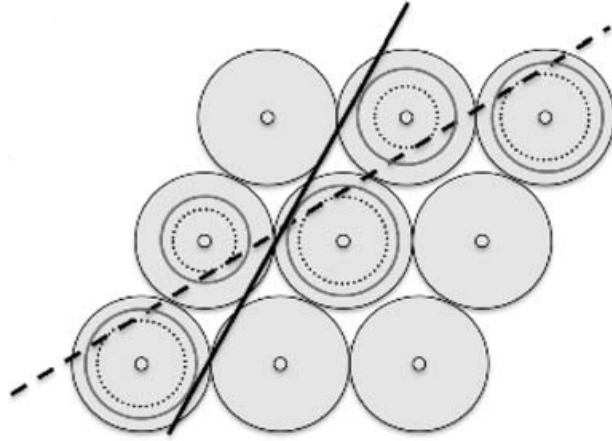


Figure 4.2: Cross section of an MDT multi-layer segment with track as reconstructed by nominal muon reconstruction algorithms with fixed hit timing information (solid black line) and as reconstructed by an algorithm dedicated to slow particles allowing for variable hit timing information (dashed black line). MDT tubes are drawn as grey circles. The drift circles as assumed by nominal muon reconstruction algorithms (solid black circles) and by the dedicated reconstruction algorithm (dotted black circles) are also given. Figure taken from [91].

(most) nominal muon reconstruction algorithms [91]:

- Hits — and especially trigger hits — are recovered for reconstruction by additionally considering the next bunch crossing.
- The reconstruction starts from Inner-Detector tracks, where the time of flight of a particle with low β does not yet differ a lot from a particle propagating at the speed of light and is thus easier to detect. Extrapolating the ID track towards the outer detector then allows to assign muon spectrometer hits to the track with high efficiency.
- The particle velocity β is estimated from the hit time in the RPCs, preventing a misidentification of the slow particle as a muon. In contrast, nominal reconstruction algorithms do not provide a β estimate at all as muons have most certainly $\beta \approx 1$.
- The particle velocity is used as a free parameter when fitting tracks to the MDT hits, allowing for variable drift radii. In the end, the track that minimises the χ^2 of the MDT segments is selected. This strongly improves the fit quality as shown in Figure 4.2.

With this setup, as is also indicated in Figure 4.1, the reconstruction efficiency of MUGIRL-STAU of muon-like particles for low β can exceed that of the nominal muon reconstruction algorithms by far.

4.3 Current results

The searches for charged SMPs of ATLAS use the observables and dedicated reconstruction algorithm explained in the previous sections. In 2015, ATLAS published a search for charged SMPs, and heavy charged LLPs in general, at $\sqrt{s} = 8 \text{ TeV}$ with an integrated luminosity of 19.1 fb^{-1} [80]. Long-lived staus in models with gauge-mediated symmetry breaking and LeptoSUSY models, directly produced charginos in simplified models [92–94] and R -hadrons¹ were investigated more closely. In 2016, a search at $\sqrt{s} = 13 \text{ TeV}$ for R -hadrons only and with $\mathcal{L} = 3.2 \text{ fb}^{-1}$ was performed [81]. At the time of writing, a search with $\mathcal{L} = 36.1 \text{ fb}^{-1}$ at $\sqrt{s} = 13 \text{ TeV}$ [82] is to be submitted to *Phys. Rev. D*.

Unfortunately, neither the searches in 2015 nor in 2016 observed significant excesses over the estimated background. Therefore, ATLAS provided upper exclusion limits on production cross sections and lower exclusion limits on particle masses. Exemplary, the results achieved for models with pair-produced long-lived charginos in 2015 shall be given here: Figure 4.3a shows the events observed for various masses as well as the estimated background and the expected signal in a signal region with one chargino candidate that fulfills loose selection criteria as defined in [80]. Figure 4.3b yields the according upper limits for the cross section as expected and observed. The observed limit is consistently above the expected limit due to the small excess of data events over the background estimate in Figure 4.3a. This corresponds to an exclusion of chargino masses below 620 GeV.

4.4 Upcoming searches

With the data-taking period Run 2 coming to an end in 2018, a search for charged SMPs as described above but with the full Run-2 dataset as recorded by ATLAS stands to reason. In Run 2, ATLAS recorded 149 fb^{-1} of data in pp collisions [56], raising hopes of finally observing charged SMPs or at least increasing the current lower mass limits.

But apart from the greater amount of recorded integrated luminosity, there is also another reason for a renewed attempt of this search: The analysis software of ATLAS is based on a software framework called ATHENA, which received a major revision during the last few years, going from release 20.7 (R20.7) to release 21 (R21). With this rework, also the MUGIRLSTAU algorithm — since then called MUGIRLLOWBETA — was rewritten from scratch.

4.4.1 Changes in the new reconstruction algorithm

One of the reasons for the rewrite of MUGIRLSTAU was to dispose the algorithm of bugs. The so-called *RPC-timing bug* [95] was the most extensive one of those. Hereby, RPC t_0 distributions as output by MUGIRLSTAU showed asymmetric tails towards negative values

¹ R -hadrons are hadrons where one SM particle is replaced by a SUSY particle, e.g., gluino, stop or sbottom.

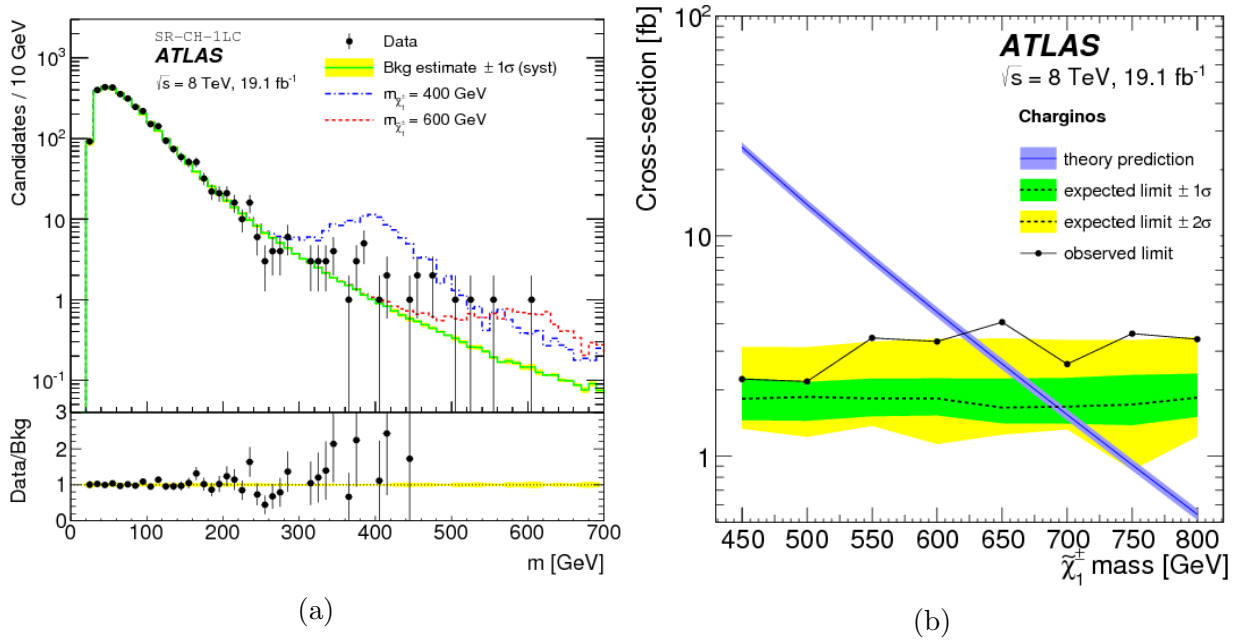


Figure 4.3: (a) Reconstructed mass in observed data, background estimate and expected signal (for masses $m_{\tilde{\chi}_1^\pm} = 400$ GeV and 600 GeV) of the search conducted in [80] in a signal region in which one chargino of a produced chargino pair is detected and fulfills loose selection criteria. (b) Upper limits for the cross section of the search conducted in [80] for various chargino masses in models with a long-lived chargino. The solid black line corresponds to the observed limit. The dashed black line is the expected limit with uncertainty bands at $\pm 1\sigma$ (green) and $\pm 2\sigma$ (yellow), respectively. The solid blue line is the theoretical cross section with a shaded $\pm 1\sigma$ uncertainty band. Figures taken from [80].

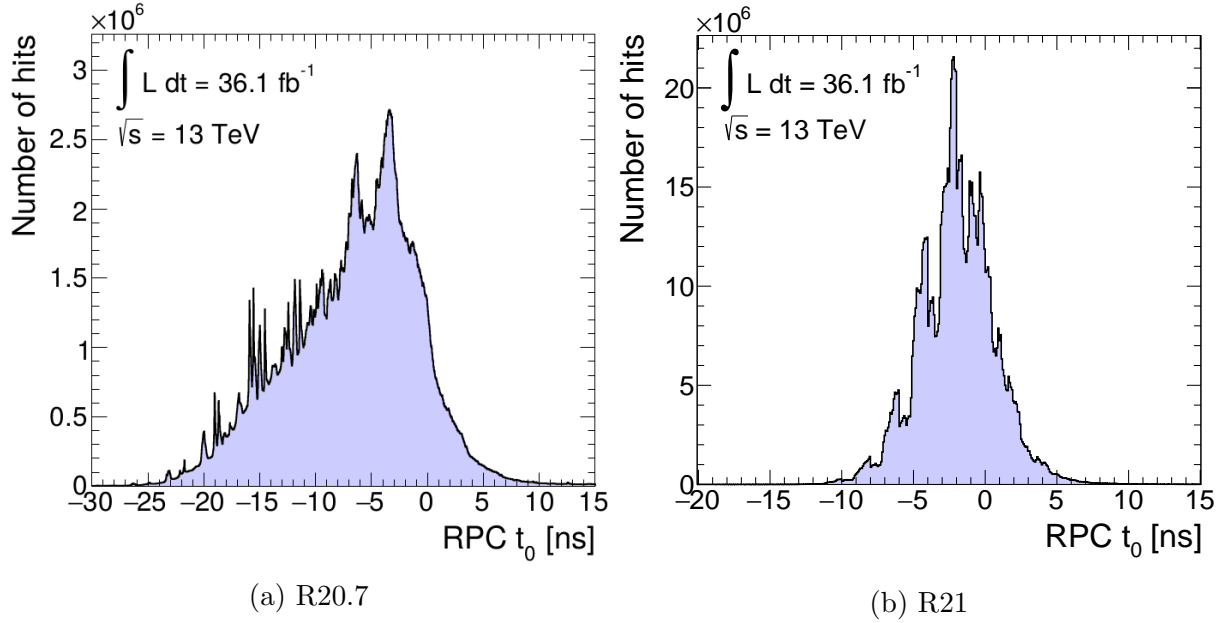


Figure 4.4: t_0 distribution for muons as output by MUGIRLSTAU in R20.7 (a) and MUGIRLLOWBETA in R21 (b). A Gaussian shape centred at $t_0 = 0$ ns is expected. This is not fulfilled for R20.7 where a tail towards negative t_0 values can be seen. The spiky structure in both distributions arises due to the RPC readout timing-granularity. Note that the number of hits is subject to different selection criteria, reconstruction techniques and binning, and therefore not comparable. Figure (a) was taken from [95].

as depicted in Figure 4.4a. The reason for this was found to be an incorrect calculation of the distance between a hit and the IP, taking only the distance in transverse plane into account and neglecting the z -direction. This could be approximately fixed during analysis, ensuring valid analysis results. Nevertheless, a fix on reconstruction-algorithm level is a much cleaner solution and was made for MUGIRLLOWBETA in R21. The success of this can be seen in the symmetric t_0 distribution in Figure 4.4b. The spiky structure of the distributions in Figure 4.4 arises due to the internal RPC readout timing-granularity which will be discussed in more detail in Section 5.3.

The changes apart from this bug fixing from MUGIRLSTAU to MUGIRLLOWBETA were intensely investigated for this work. One main advantage of MUGIRLLOWBETA over MUGIRLSTAU is that it has a significantly higher reconstruction efficiency, as can be seen in Figure 4.5.

To better understand where the gain in efficiency originates, a study was carried out, comparing the reconstruction results of MUGIRLSTAU and MUGIRLLOWBETA. For this, simulated stable-stau events were reconstructed with MUGIRLSTAU and identifiers on truth level of the reconstructed particles were stored. Afterwards, the procedure was repeated, this time reconstructing the stable-stau events with MUGIRLLOWBETA. Comparing the

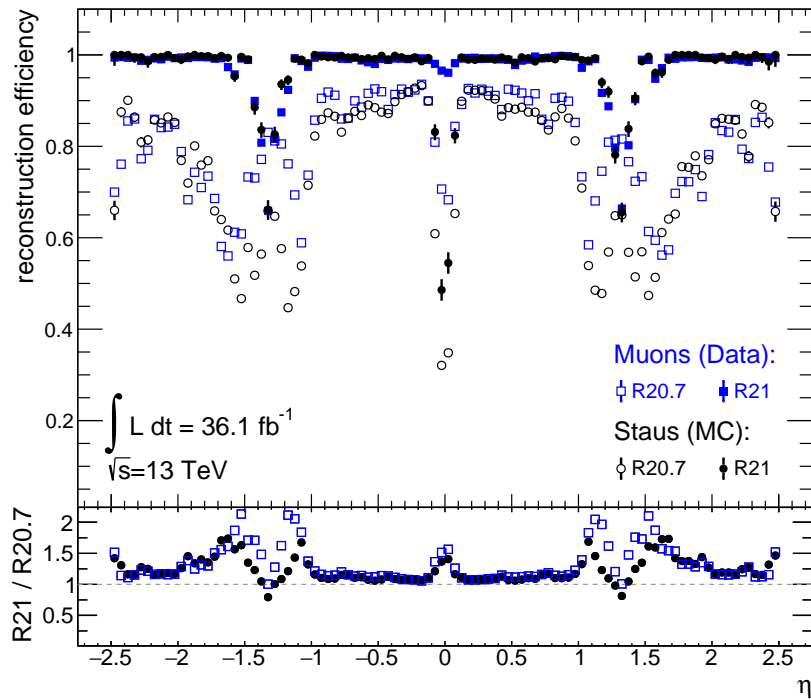


Figure 4.5: Reconstruction efficiency of muons (blue squares) and stable staus (black dots) in R20.7 (open symbols) and R21 (full symbols). The reconstruction efficiency uses matching to medium muons for data and to truth for MC. In the bottom plot, the ratios of the efficiencies in R20.7 and R21 are shown for muons (blue open boxes) and staus (black full dots).

Input type	Matched to	Rec. eff. $\pm \sigma_{\text{rec. eff.}}$ [%] in	
		R20.7	R21
Data	medium muons	80.715 ± 0.034	96.734 ± 0.009
MC: $Z \rightarrow \mu\mu$	medium muons	78.233 ± 0.033	97.49 ± 0.12
	truth	76.482 ± 0.034	95.51 ± 0.15
MC: Stable Staus	truth	74.91 ± 0.08	95.60 ± 0.10

Table 4.1: Reconstruction efficiencies of MUGIRLSTAU in R20.7 and MUGIRLLOWBETA in R21 for different types of input. Reconstructed candidates are thereby either matched to truth information or medium muons.

stored lists of reconstructed particles, it is possible to recognise differences in reconstruction. A summary of this study is shown in Figure 4.6. Here, the distributions of particles that were only reconstructed with MUGIRLLOWBETA but not with MUGIRLSTAU are shown for various quantities. This allows to highlight the differences in reconstruction, in contrast to comparing the distributions of all particles reconstructed in R20.7 to R21, where differences would be lost to the eye by the large amount of particles that were reconstructed in both releases. As a reference, also the distributions of the simulated particles on truth level are given.

In Figure 4.6, if no dependence of the gain in reconstruction on the variable plotted on the x -axis exists, the distributions for truth level and for particles that were only reconstructed in R21 should look similar, as is the case for ϕ and β . If the reconstruction in R21 is superior to that in R20.7 in dependency of the investigated quantity, a difference between the distributions is expected. This is marginally the case for p_T and clearly for η . Note that a bin entry of the R21-only distribution below the according truth value does not indicate a worse reconstruction in R21 for that bin as the distributions are normalised.

When analysing Figures 4.5 and 4.6, most strikingly the reconstruction of MUGIRLLOWBETA is especially in the crack regions $1.0 < |\eta| < 1.7$ and $\eta \approx 0$ better than that of MUGIRLSTAU. Unfortunately, it is hard to determine in more detail what gives rise to this superiority: Although they apply similar techniques, their code is completely different. Nevertheless, the integrated reconstruction efficiency can be quantified as shown in Table 4.1. Independent of which kind of input type or matching target is considered, MUGIRLLOWBETA has a much higher reconstruction efficiency than MUGIRLSTAU, which is a large improvement. In addition, for MUGIRLLOWBETA the reconstruction efficiencies are more uniform when considering the different input types and matching targets, indicating a more reliable reconstruction.

Hence, MUGIRLLOWBETA can be seen as a great success with many improvements compared to MUGIRLSTAU. Unfortunately, in the course of this work, it was also discovered that MUGIRLLOWBETA contains a bug of its own: In the barrel region of ATLAS' side C, less hits are assigned to reconstructed particles than in side A. This can be unambiguously

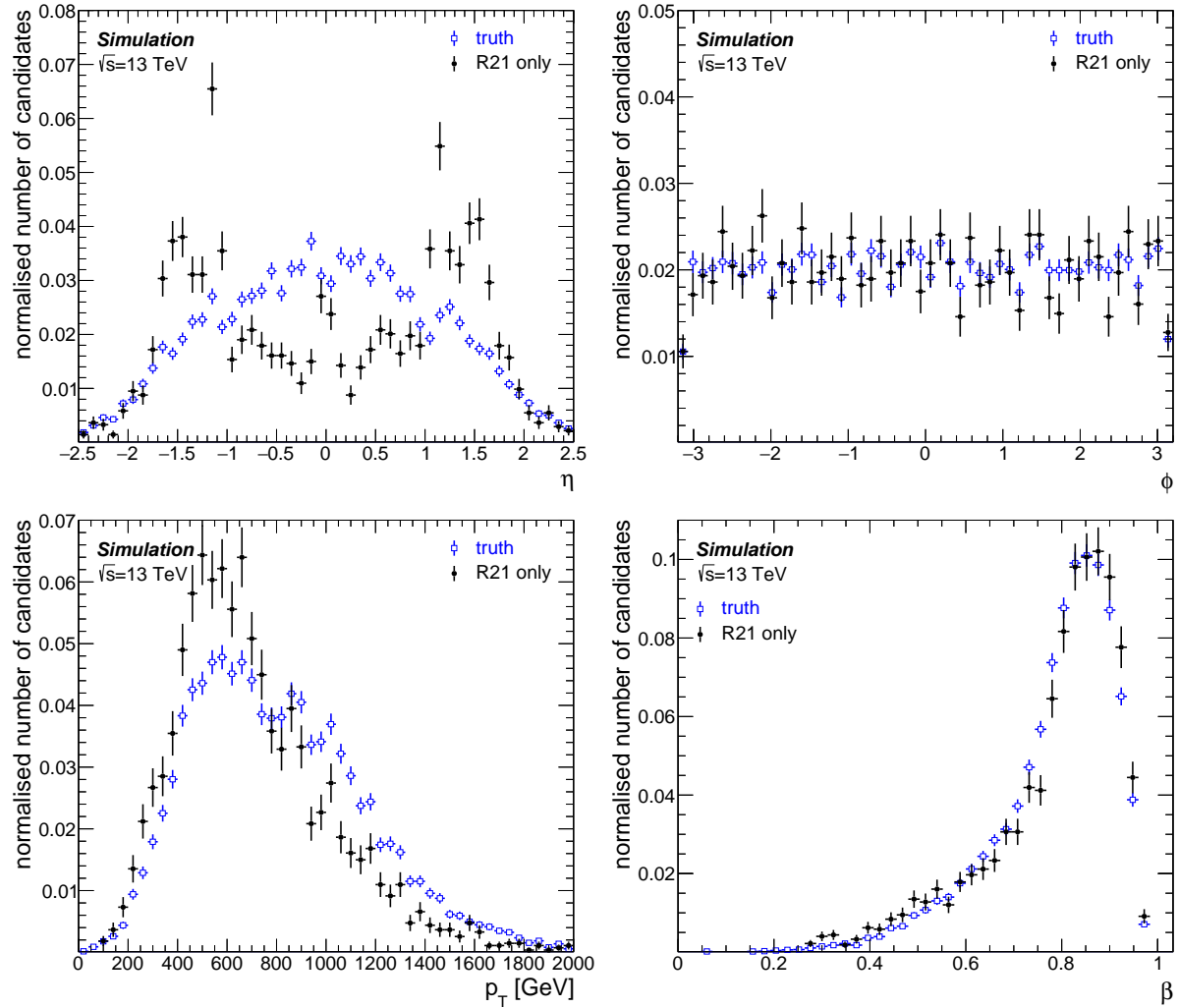


Figure 4.6: Distributions in η (top-left), ϕ (top-right), p_T (bottom-left) and β (bottom-right) for stable staus, on the one hand on truth level (blue open boxes) and on the other hand of those that were only reconstructed in R21 but not in R20.7 (full black dots).

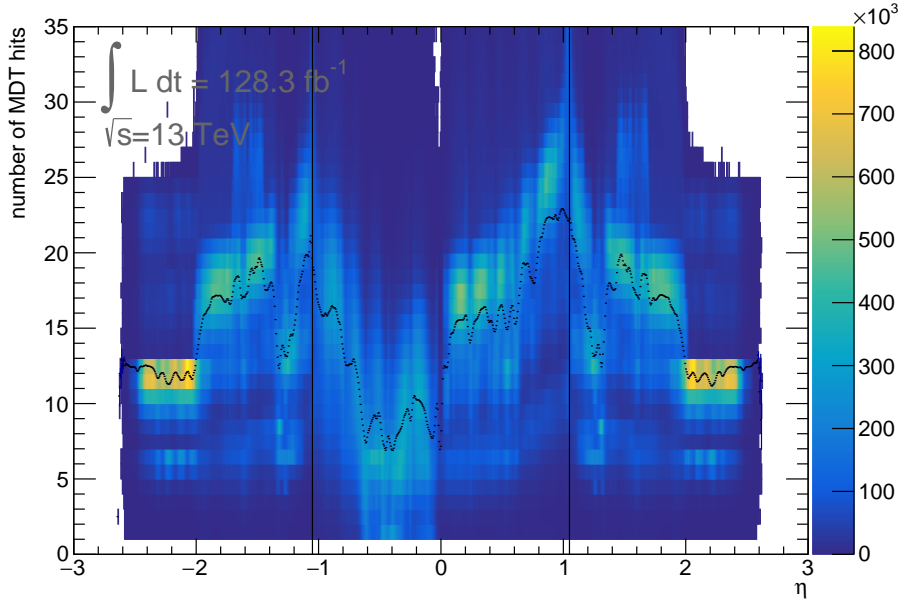


Figure 4.7: Number of MDT hits per muon registered by MUGIRLOWBETA versus η of the reconstructed muons. The mean number of hits per η -bin is drawn in black. Vertical black lines mark the approximate border at $|\eta| \approx 1.05$ of the ATLAS barrel region.

seen in Figure 4.7. Extensive studies have been carried out on this bug, the results of which are summarised in Appendix A. At the time of writing, the exact origin of the bug was not yet completely determined. Nevertheless, there are strong hints indicating the hits might be reconstructed and used for track fitting but are simply not assigned to the reconstructed particle afterwards. Thanks to the availability of RPC hits in the affected region, the combined β estimate for the muon spectrometer does not suffer massive losses in accuracy as will be shown in Section 5.11. Therefore, it still has to be clarified whether a reprocessing of data is needed at all, and setting up a procedure for calibrating the muon spectrometer continues to be necessary and sensible.

Except for this bug, a clear sign that MUGIRLOWBETA in general yields more reliable results than MUGIRLSTAU is the improved β estimate: When comparing to MC events, MUGIRLOWBETA's estimates are closer to the truth value than MUGIRLSTAU's. Despite this, a timing calibration of the muon spectrometer is indispensable to further improve the β measurement and achieve a meaningful uncertainty for it.

Apart from the changes from MUGIRLSTAU to MUGIRLOWBETA mentioned above, there was also a redefinition of the term "hit" for RPCs: While for MUGIRLSTAU a "hit" referred to the signal of an interaction in one η - or ϕ -strip, in MUGIRLOWBETA hits are *clustered*. For this, the signals at the two gas gaps within an RPC unit are combined in a weighted mean which increases the precision of position and timing measurement. Hereby,

η - and ϕ -strips are still treated separately. In consequence, in R21 an RPC unit does not yield four hits — one per gas gap and strip-type — for each track anymore, as was the case for R20.7. Instead, only two hits per RPC unit and track are expected.

Unfortunately, this clustering of hits also has two disadvantages: On the one hand, information on the individual hits, like the propagation time of the signal along the strip, is lost. On the other hand, less hits are available for calculating a β estimate. Arguably, more hits in the RPC system might be better for an accurate β estimate than a higher precision on the individual timing measurement of RPC hits.

Chapter 5

Timing calibration of the ATLAS muon spectrometer

In a search as outlined in the previous chapter, a thorough calibration of the detector systems and investigation of their β resolution is important. Only then, a meaningful statement on the precision of the β measurements can be made and as strong as possible exclusion limits obtained. While the calibration for dE/dx can be adopted from [84], no other search in ATLAS relies on the time of flight and β measured in the tile calorimeter and the muon spectrometer as much as the type of search outlined in Chapter 4. Thus, a calibration strategy for the mentioned detector systems has to be developed. This work is focussed on the timing calibration of time-of-flight and according β measurements in the muon spectrometer of ATLAS, which shall be described in the following chapter in detail. For a timing calibration of the tile calorimeter see Reference [96].

A calibration of the muon spectrometer is mandatory, as the timing information of a hit for a single detector element is subject to many influences. Aim of the calibration is to get rid of all factors which distort the measurements. For this, many different calibration steps are needed. In the following, uncalibrated distributions as well as distributions after certain calibration steps are abbreviated by key symbols. This simplifies stating the complete calibration chain applied for a shown distribution. Examples are "U" for uncalibrated distributions or "DP" for distributions that received first a drift-time calibration (D) and afterwards a propagation-time calibration (P).

It is optimal to use the timing information of muons for calibration, as they are charged and reach the MS, just like charged SMPs would. In addition, muons have a very low mass and therefore simple kinematic properties: They propagate through the detector with almost the speed of light, i.e., $\beta = 1$, and should therefore be measured with $t_0 = 0$ ns.

5.1 Data and simulated events

The data used for this calibration was taken in the years 2015–2018, whereby 2018 data could be taken into account up to 24th September. This corresponds to an integrated luminosity of $\mathcal{L} = 128.3 \text{ fb}^{-1}$. The uncertainty in the combined 2015–2017 integrated luminosity, $\mathcal{L} = 80.5 \text{ fb}^{-1}$, is 2.0%. It is derived, following a methodology similar to that detailed in Reference [97], and using the LUCID-2 detector for the baseline luminosity measurements [98], from the calibration of the luminosity scale using x - y -beam-separation scans. At the time of writing, no final uncertainty on the 2018 luminosity is available yet. The bunch spacing in the data-taking period 2015–2018 was 25 ns.

In addition to collision data, a number of different types of simulated events are used in this work, which shall be described in the following.

For calibration, events in which a Z boson decays into a muon–antimuon pair, $Z \rightarrow \mu\mu$, are simulated using the MC event generators PYTHIA8 v. 8.186 [99] and EvtGen v. 1.2.0 [100] interfaced with Powheg r2856 [101] and the CTEQ6L1 [102] and AZNLO [103] PDF set.

For the reconstruction efficiencies in Chapter 4 as well as investigations on the effects of the calibration on charged SMPs at the end of this chapter, MC generated events of stable staus and charginos are used. Pair produced stable staus, motivated by a SUSY model with gauge-mediated symmetry breaking (GMSB) [104–106] where $m_{\text{Messenger}} = 500 \text{ TeV}$, $C_{\text{grav}} = 100000$, $\tan\beta = 10$ and $\text{sgn}(\mu) = 1$, were simulated at leading order. For this, the MC event generators PYTHIA8 v. 8.212, MG5_aMC@NLO v. 2.3.3 [107] and EvtGen v. 1.2.0 using the NNPDF23LO [108] and A14 tune [109] PDF set are combined.

Stable charginos, inspired by a SUSY model with minimal anomaly-mediated symmetry breaking (mAMSB) [110, 111] where $m_0 = 5 \text{ TeV}$ and $\tan\beta = 5$, either pair-produced or produced in association with a neutralino, are simulated with the same setup.

After generation, all MC events are passed through a full detector simulation [112] that uses the GEANT4 framework [113]. The MC events also include the effect of in-time and out-of-time pile-up, simulated in PYTHIA8 v. 8.186 and EvtGen v. 1.2.0 with the A2 tune [114] and MSTW2008LO [115] PDF set. In addition, the MC events are reweighted according to the pile-up such that the distribution of the number of collisions per BC is the same in MC and collision data.

In consequence, the output of the MC simulation chain is equivalent to that of collision data and can be treated similarly afterwards. From this, particles are reconstructed and the corresponding information is saved as analysis-object data (xAOD).

5.2 Event selection

To reduce disk space and allow faster processing, for analyses with different demands derived xAODs (DxAODs) are produced, in which information unnecessary for this type of analysis is removed. For searches for charged SMPs of ATLAS as well as for the work at hand, an xAOD format called SUSY8 is used. SUSY8 applies a preselection on events,

requiring those to have fired an E_T^{miss} or muon trigger. While events added by the E_T^{miss} trigger are required for searches for charged SMPs, they are not useful for this calibration if they contain no actual muon. This is, among others, one of the reasons to apply some selection criteria on the available particles reconstructed by the algorithm MUGIRLLowBETA: In the end, only muons are supposed to be used for calibration. The first set of selection criteria is of a more general nature:

1. Only those muons are considered for which the full information is available. This requires that all links between the different representations of the muon in data are valid.
2. Muons with a $p_T < 26$ GeV are rejected, the reason for which is twofold: On the one hand, the p_T threshold for the muon trigger was changed multiple times during the data-taking period 2015–2018 to retain a constant data rate despite the different pile-up conditions. As the highest p_T threshold was 26 GeV, a cut at $p_T = 26$ GeV yields a more uniform lower p_T limit. On the other hand, due to their large mass, charged SMPs are expected to have a high p_T and therefore low- p_T muons could cause calibration constants unfavorable for charged SMPs.
3. As muons are reconstructed with higher precision by reconstruction algorithms aiming at muons, rather than MUGIRLLowBETA aiming at charged SMPs, only those muons are considered for calibration that are reconstructed by MUGIRLLowBETA and can be ΔR -matched to medium muons of the nominal muon reconstruction algorithms.

Many muons emerging from a collision can be affiliated to $Z \rightarrow \mu\mu$ decays, which have a clear decay signature. With $Z \rightarrow \mu\mu$ selection criteria in addition to the previous set of selection criteria, it can therefore be assured that indeed only muons are used for calibration. At the same time, this increases the agreement with the distributions from simulated $Z \rightarrow \mu\mu$ events used for deriving a procedure for simulation treatment in Chapter 6. Thus, the following $Z \rightarrow \mu\mu$ selection criteria are applied:

4. An event with muons for calibration has to contain exactly two muons.
5. The invariant mass $m_{\mu\mu}$ of those two muons has to be close to the Z boson mass, i.e., $|m_{\mu\mu} - m_Z| < 10.0$ GeV with $m_Z = 91.2$ GeV.
6. The two muons have to be of opposite charge as the Z boson decays into a muon–antimuon pair.

Unless stated otherwise, e.g., if large statistics is needed for a calibration step, the $Z \rightarrow \mu\mu$ selection is also required for muons for calibration. The full cut-flow for the available data is shown in Figure 5.1.

In the used 2015–2018 dataset with $\mathcal{L} = 128.3$ fb⁻¹, 2.52×10^9 muon candidates are reconstructed by MUGIRLLowBETA. Of these, 1.71×10^9 (67.8%) fulfill the first set of

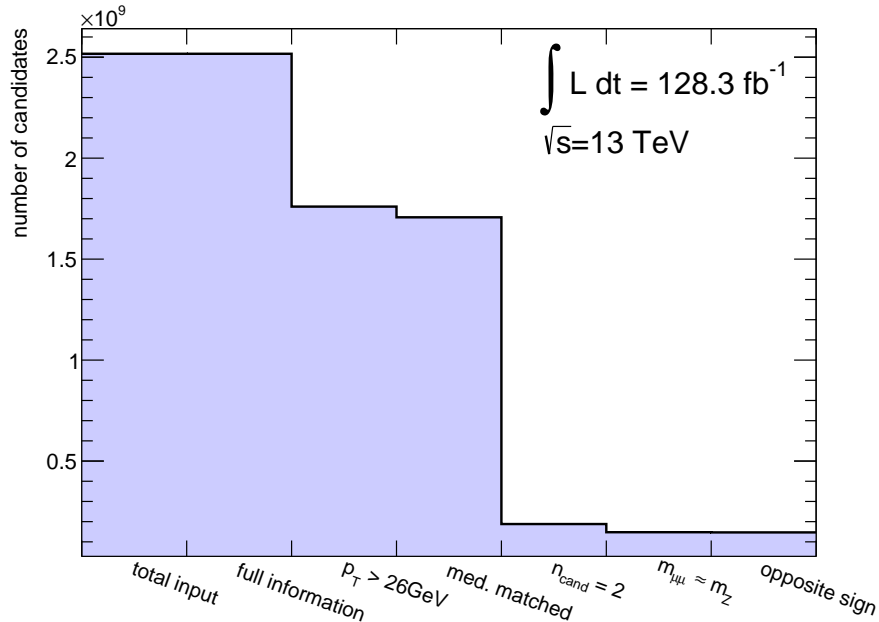


Figure 5.1: Cut-flow for the event selection by the criteria described in the text.

selection criteria. The $Z \rightarrow \mu\mu$ selection criteria are met by 0.15×10^9 candidates (5.8%). For those, in total 3.55×10^9 hits are registered, which are distributed over 359,291 MDT tubes, 118,732 RPC η -strips and 257,932 RPC ϕ -strips. On average, a muon leaves 15.1 hits in the MDT system and 5.5 in the RPC system if it is within the subdetector's acceptance. Thus, about 8,400 hits are expected for an average MDT tube, 2,200 hits for RPC η -strips and 1,000 hits for RPC ϕ -strips.

For the MC calibration, the simulated $Z \rightarrow \mu\mu$ events are used. A total weight of 3.39×10^8 events is available, whereof 1.76×10^8 (51.7%) fulfill all of the above selection criteria. Naturally, this is a higher percentage than in data, since the $Z \rightarrow \mu\mu$ selection criteria are more easily met for those MC events.

5.3 Uncalibrated distributions

Although intrinsically the detector already measures t_0 , this information is lost for analyses and only the time-of-flight (ToF) values calculated from t_0 measurements are available. The ToF distributions of the hits in the MDTs and RPCs can be seen in Figure 5.2. For MDTs, the positions of the distinct detector layers can be observed: The detector layers of the barrel region as well as the inner end-cap layers are merged into the first peak; the middle and outer detector layers of the end-caps form the second and third peak, respectively. As RPCs are only located in the barrel region, the measured ToF is in general lower and no distinct peaks can be observed as the distance between chambers is smaller than for MDTs.

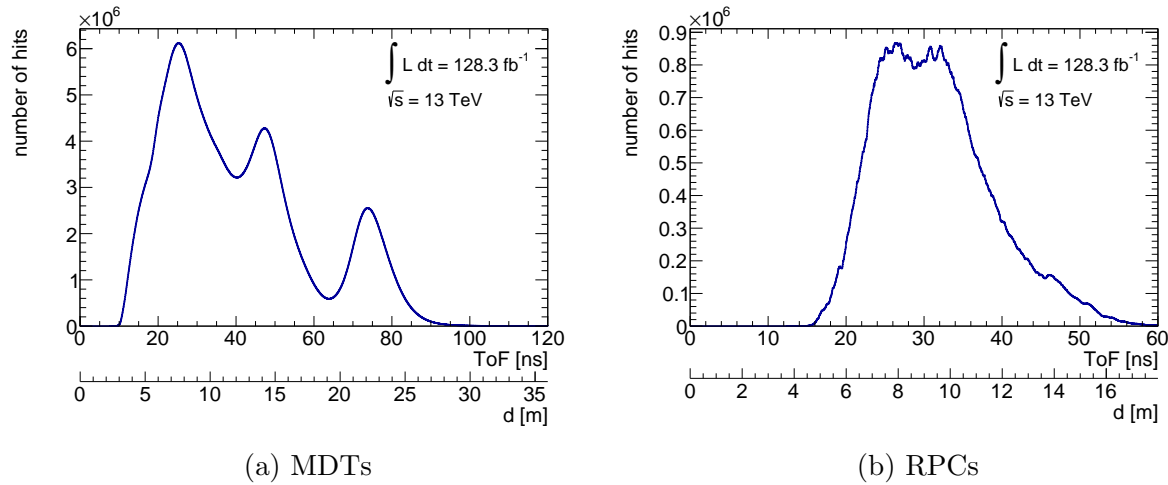


Figure 5.2: ToF distribution of the hits in the MDT (a) and RPC (b) system, respectively. As RPCs are only located in the barrel region, smaller ToF values are observed than for MDTs. The distance of the hits to the IP, d , assuming the detected particle to propagate at speed of light is also given.

From the ToF and the distance of the hit to the IP, t_0 of a hit then has to be calculated anew following equation (4.3). The t_0 distributions before the calibration for MDTs and RPC η - and ϕ -strips can be seen in Figure 5.3. The most striking feature is the spiky structure for RPCs, which is a result of the readout timing-granularity: As RPCs are only read out every 3.125 ns (see Section 3.2.3), in fact discrete peaks with a temporal distance of 3.125 ns are measured. From this, a calculated *propagation time* of the signal along the strip is artificially subtracted afterwards to account for the position of the hit along the strip. This could be made visible in R20.7 by adding the propagation time anew as shown in Figure 5.4. In R21, due to the clustering of RPC hits, the propagation-time information is lost, unfortunately, so it cannot be demonstrated with data reconstructed in R21.

Apart from this spikiness, the t_0 distributions in Figure 5.3 resemble Gaussian distributions, which is expected due to small deviations in the detector electronics and in reconstruction. Those distributions can be fitted with a Gaussian functional parametrisation

$$f(x) = a \cdot e^{-\frac{(x-\mu)^2}{2\sigma^2}}. \quad (5.1)$$

The mean \bar{t}_0 and resolution σ quoted in Figure 5.3 and other figures of this kind in this work then correspond to μ and σ of equation (5.1), respectively. a is a parameter ensuring the correct normalisation of the function and can be ignored in most cases. To make the results less dependent on outliers of the distribution, only a window of (unfitted) distribution mean \pm the RMS is fitted.

Another fact that can be seen in Figure 5.3 is that RPCs have evidently a better timing resolution than MDTs. The very good timing resolution of RPCs is of course also required

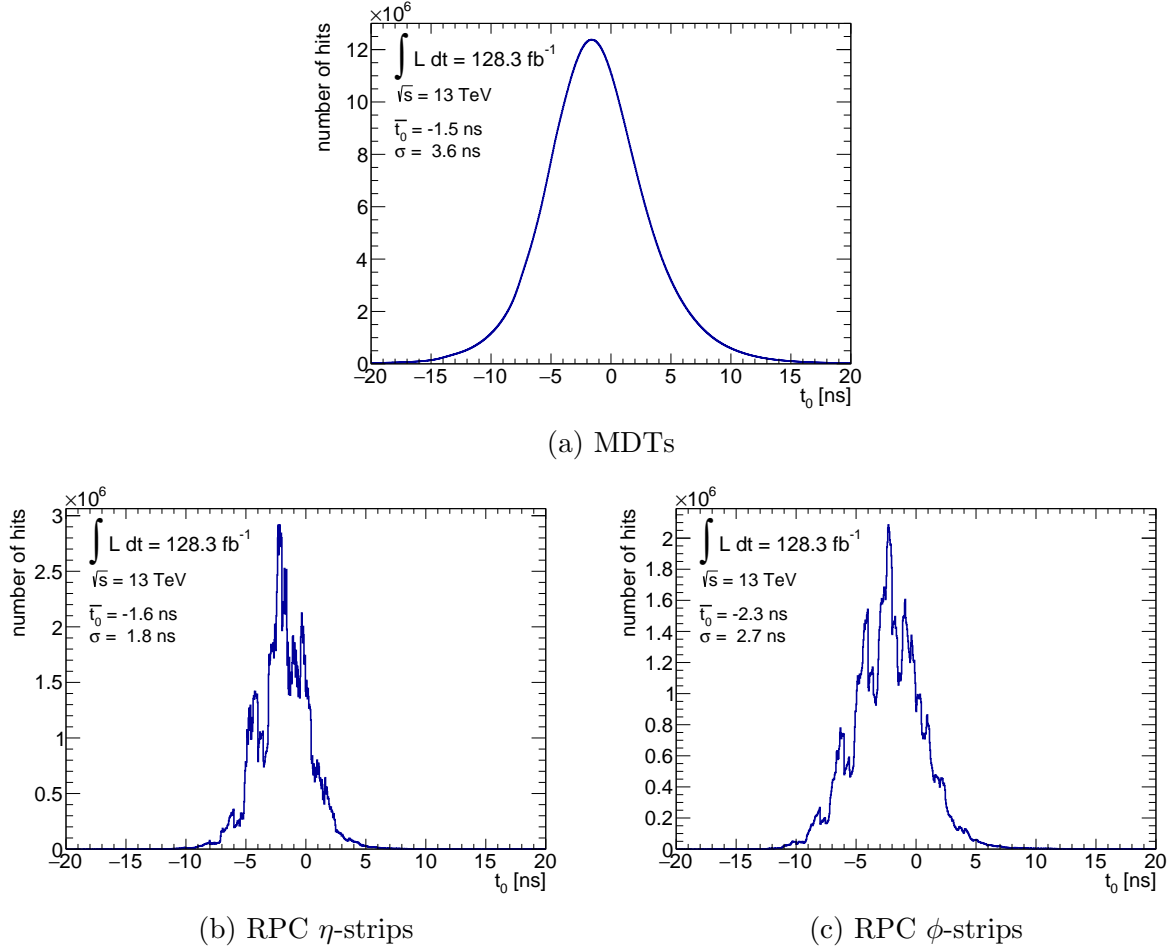


Figure 5.3: Uncalibrated t_0 distributions for MDTs as well as RPC η - and ϕ -strips. The distributions resemble Gaussian distributions as expected, although merely roughly for RPCs. Here, the spiky structure arises due to the readout timing-granularity. Given are also the mean and standard deviation of Gaussian fits using a reduced fitting window mean \pm RMS to the distributions.

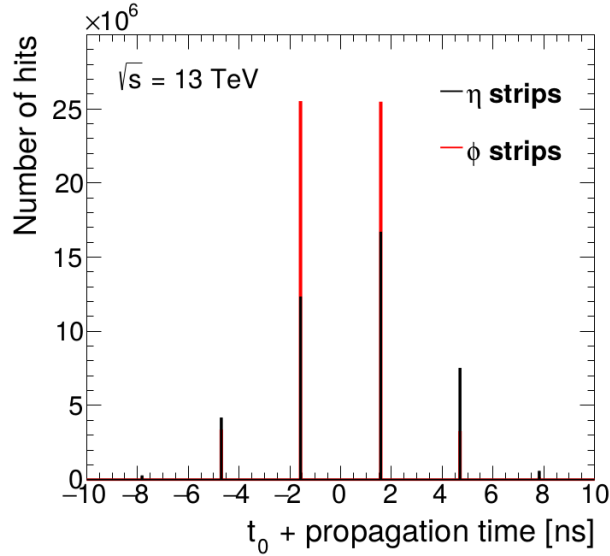


Figure 5.4: Timing measurements by RPCs in R20.7. If the previously subtracted, calculated propagation time is added to t_0 anew, the timing-granularity of the RPC readout can be made visible. Figure adapted from [95].

as they are part of the trigger system. However, RPC η - and ϕ -strips possess individual readout electronics, which lead to differences in the shapes that become obvious when comparing Figure 5.3b and Figure 5.3c. Therefore, it is sensible to treat η - and ϕ -strips as separate systems in the calibration steps described in this chapter.

In Figure 5.3, the distributions are broad and clearly not centred at $t_0 = 0$ ns. The aim of the calibration is to correctly centre the distributions and make them as sharp as possible. For this, many corrections are introduced later in this chapter. As those are considered to be independent, the final $t_{0,i}^{\text{out}}$ value of a hit i can be calculated as

$$t_{0,i}^{\text{out}} = t_{0,i}^{\text{in}} - \sum_{\text{corrections}} t_{0,i}^{\text{corr}}.$$

Hereby, $t_{0,i}^{\text{in}}$ is the uncalibrated t_0 value and $t_{0,i}^{\text{corr}}$ are the appropriate corrections applied to this hit.

For β distributions, at first the inverse of β_i is calculated for each hit, as according to equation (4.4) $\beta_i \propto t_{0,i}^{-1}$. Therefore, β_i^{-1} can take the uncertainty of $t_{0,i}$, $\sigma_{t_{0,i}}$, more easily into account:

$$\begin{aligned} \beta_i^{-1} &= \frac{t_{0,i}}{d_i} \cdot c + 1, \\ \sigma_{\beta_i^{-1}} &= \left| \frac{\partial \beta_i^{-1}}{\partial t_{0,i}} \right| \cdot \sigma_{t_{0,i}} = \frac{c}{d_i} \cdot \sigma_{t_{0,i}}. \end{aligned} \quad (5.2)$$

Due to the large distance of MDTs and RPCs from the IP, the uncertainty of the distance measurement, σ_d , can be neglected in equation (5.2): Even taking the worst nominal spatial resolution for the muon spectrometer, $\sigma_d \approx 10$ mm for RPCs (see Section 3.2.3), into account, the ratio of distance to distance uncertainty is of the order 10^{-3} and therefore negligible compared to the uncertainty of the timing measurement.

The final value for β^{-1} is not calculated per hit but incorporates the information of all hits of the reconstructed particle, weighted according to their uncertainty:

$$\beta^{-1} = \frac{\sum_i \beta_i^{-1} / \sigma_{\beta_i}^2}{\sum_i 1 / \sigma_{\beta_i}^2}. \quad (5.3)$$

The uncertainty of β^{-1} , in turn, can be calculated as

$$\sigma_{\beta^{-1}}^2 = \frac{1}{\sum_i 1 / \sigma_{\beta_i}^2}.$$

β can then be obtained by inverting β^{-1} .

For β , RPC η - and ϕ -strip measurements are combined into a system-wide weighted mean. The uncalibrated distributions (symbol U) for β of the RPC and MDT system are shown in Figure 5.5. The expected shape of a Gaussian distribution is clearly visible. Like for t_0 , it is the aim of the calibration to make the shapes as sharp as possible, but centred at $\beta = 1$, of course. It is noticeable that, although RPCs have a better timing resolution than MDTs, their initial β estimate is worse than that of MDTs. The reason for this is that there are less than six hits available for the β estimate in the RPC system, while there are more than 15 for MDTs on average.

5.4 Previous calibration

As also the previous searches for charged SMPs with ATLAS required a timing calibration of the muon spectrometer, such a calibration was already conducted previous to the work at hand. However, the previous calibration was based on MUGIRLSTAU instead of MUGIRLLOWBETA, making a new calibration inevitable. In addition, while at the time of the previous calibration only $\mathcal{L} = 36.1 \text{ fb}^{-1}$ of data were available, this new approach for a calibration can make use of $\mathcal{L} = 128.3 \text{ fb}^{-1}$. That allows to require more restrict selection criteria on the particles used for calibration and to apply different techniques at some places.

A complete description of the previous calibration can be found in [95]. The first step of it was to apply an online-timing correction to RPCs. As RPCs are part of the trigger system, their timing measurements are adjusted on a regular basis. This splits the data-taking period 2015–2016 into different intervals for each of which a correction constant was derived. MDTs are not part of the trigger system and were therefore disregarded in this step.

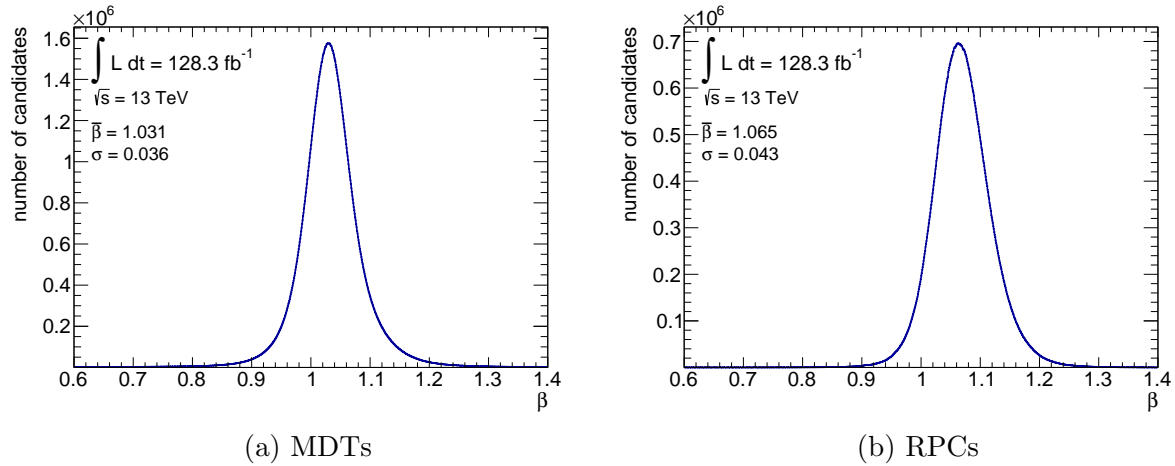


Figure 5.5: Uncalibrated β distributions for MDTs (a) as well as RPCs (b). Given are also the mean and standard deviation of Gaussian fits using a reduced fitting window mean \pm RMS to the distributions.

The second step was to derive a correction constant for each MDT tube and RPC strip, the third to determine the correction needed for each run. Finally, the pull (see also Section 5.10) was corrected to represent the uncertainties of the measurements correctly. The improvements by the single calibration steps as well as the final results of the data calibration for MDTs and RPCs are shown in Figure 5.6.

It can be noted that the initial β resolution for RPCs in the previous calibration and the calibration at hand are equivalent. For MDTs, however, it is significantly better in the previous calibration than it is for this renewed attempt. The reasons for this are manifold: First and foremost, the reconstruction is carried out by two different algorithms that naturally yield different output. As only one consequence, the number of MDT hits is overall different in R21 than in R20.7, as shown in Figure 5.7. In a sort, also the missing MDT hits in the barrel region of side C in R21 are part of this difference, causing the β resolution on side C ($\eta < 0$) to be clearly lower than on side A ($\eta > 0$) or when taking the whole barrel region into account. This can be seen in Figure 5.8a. However, for the β resolution of MDTs in the whole detector this has only a small impact, as shown in Figure 5.8b.

In addition, also other effects matter when trying to compare the β resolutions in R20.7 and R21, e.g., the considered data-taking period: As will be discussed in Section 5.7, the mean t_0 varies on a run-wise basis, especially when comparing the data-taking period 2015–2016 to 2017 or 2018 data-taking. Like the generally different output of the algorithms, this has an impact on the β resolution, albeit a small one: The β resolution in R21 for the data-taking period 2015–2016 of $\sigma_\beta = 0.035$ is closer to the β resolution in R20.7 ($\sigma_\beta = 0.030$) than when considering the whole data-taking period 2015–2018 in R21 ($\sigma_\beta = 0.036$).

Hence, there are a number of reasons preventing direct comparability between the β resolution in R20.7 and in R21 and consequently, differences are in fact expected.

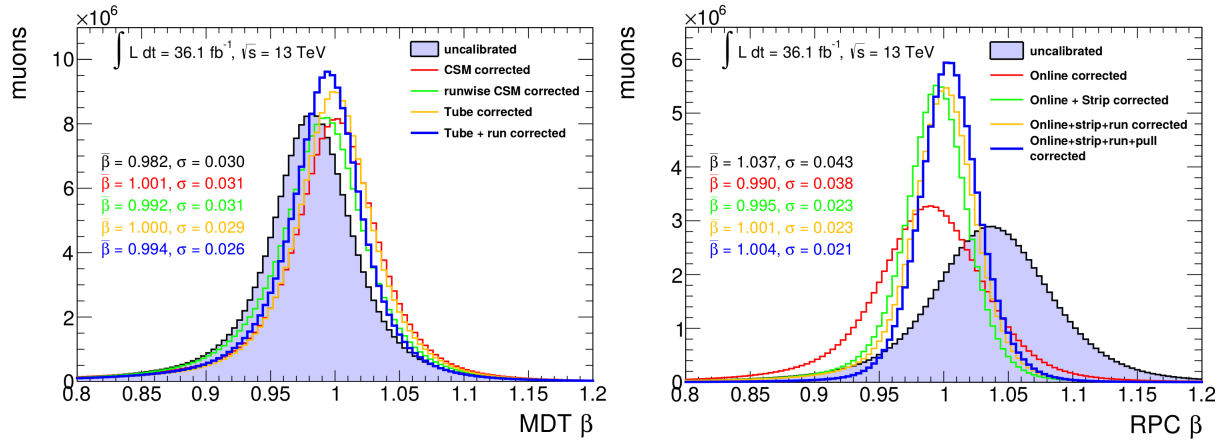


Figure 5.6: β distributions for MDTs and RPCs for the different calibration steps in the previous calibration. Figures taken from [95].

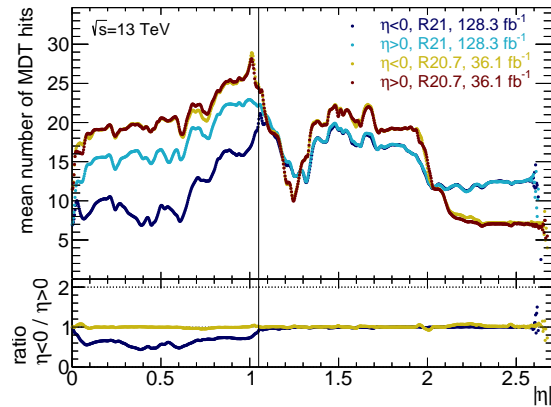


Figure 5.7: Mean number of registered MDT hits versus $|\eta|$ for R21 (dark and light blue) compared to R20.7 (yellow and red), separated into $\eta < 0$ and $\eta > 0$. The vertical black line marks the approximate border of the ATLAS barrel region. Given is also the ratio for corresponding $\eta < 0$ and $\eta > 0$ graphs.

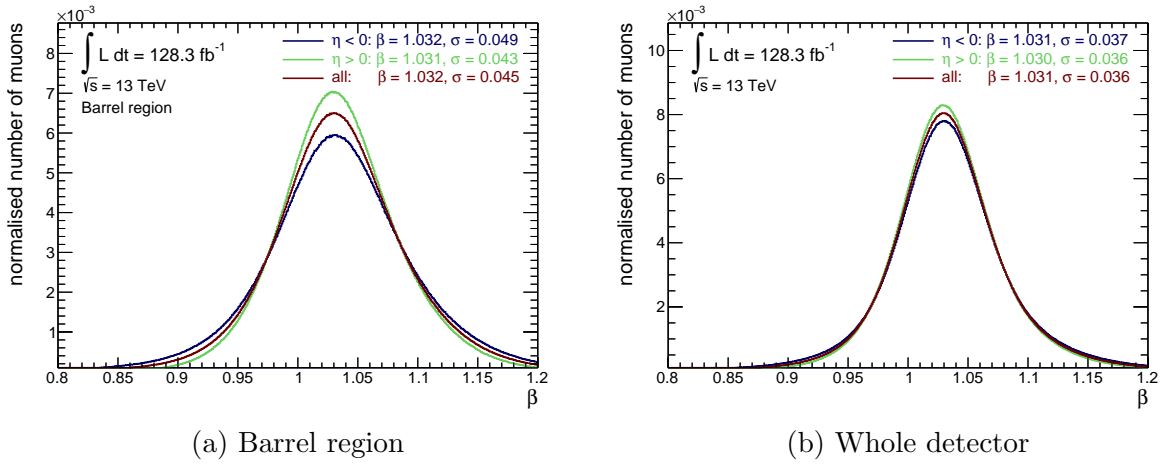


Figure 5.8: β distributions for MDTs of muons registered in R21 for the barrel region (a) and the whole detector (b). Shown are the full distribution (red) as well as distributions taking only into account $\eta < 0$ (blue) and $\eta > 0$ (green). Given are also the mean and standard deviation of Gaussian fits using a reduced fitting window $\text{mean} \pm \text{RMS}$ to the distributions.

In the previous calibration, after calibrating the data, the distributions from simulated $Z \rightarrow \mu\mu$ events were treated to match the distributions acquired for data. The success of this can be seen in Figure 5.9. Here, also the final achieved β resolution in data, $\sigma_\beta = 0.021$, when combining MDT and RPC system is shown.

5.5 Drift-time calibration

With the previous calibration as an orientation, from here on calibration constants and techniques for particles reconstructed by MUGIRLLLOWBETA in R21 shall be derived. As t_0 distributions in R21 do not show an interval structure suggesting an RPC online-timing correction as done in the previous calibration, this calibration step is abandoned.

However, one of the first obvious dependencies that are present in the measured data is the correlation between the drift time t_{drift} of charges in MDTs and t_0 as shown in Figure 5.10a. To highlight the correlation, each t_{drift} -bin is fitted with a Gaussian distribution, the mean of which is drawn in black. There are a number of features within this figure that attract attention.

First, although the physical maximum drift time is at about 700 ns, clearly also hits with $t_{\text{drift}} > 700$ ns are registered. At the same time, there are no hits registered which exhibit simultaneously very large t_{drift} and very small t_0 as well as no hits with simultaneously very small t_{drift} and very large t_0 . The reason for all of this is that t_{drift} cannot actually

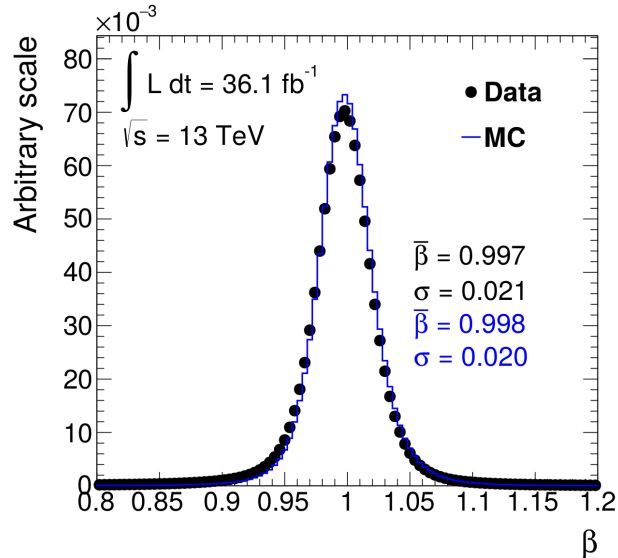


Figure 5.9: β distributions for RPC and MDT system combined in data (black dots) and in treated MC (blue line) in the previous calibration. Figure taken from [95].

be measured but has to be recalculated from t_0 and the track fit during reconstruction. Hereby, also t_{drift} values beyond the physical border are allowed. If a very large t_0 is registered, a very large t_{drift} can be assigned. Meanwhile, it does not make sense to assume a small t_0 simultaneously to a large t_{drift} . Similarly, very low t_0 values can cause very low values of t_{drift} , while low t_{drift} values are not allowed for high t_0 . This reconstruction behaviour is also the reason for the decrease in the mean of t_0 for $t_{\text{drift}} < 10$ ns and the increase in the mean for $t_{\text{drift}} > 720$ ns.

Secondly, while most hits are registered with $20 \text{ ns} < t_{\text{drift}} < 100 \text{ ns}$ and $-6 \text{ ns} < t_0 < 2 \text{ ns}$, there is a second highly populated region at $t_0 > 2 \cdot t_{\text{drift}}$. This can be best seen when enlarging the region with low t_{drift} and low $|t_0|$ as done in Figure 5.10c. Unfortunately, no convincing explanation for this feature could be found.

Thirdly, the mean of t_0 is shifted overall by about 2 ns towards negative values. In addition, for approximately $10 \text{ ns} < t_{\text{drift}} < 40 \text{ ns}$, values of t_0 are in general lower than for different t_{drift} . This is presumably caused by the fact that MDTs use a drift gas with a highly non-linear space–drift-time-relation as explained in Section 3.2.3: The dependencies between drift time and distance of a track from the wire as shown in Figure 3.10a, as well as between electron drift velocity and drift radius shown in Figure 3.10b, are supposedly not completely accounted for during reconstruction.

Lower-than-average values for t_0 are also registered in the region $680 \text{ ns} < t_{\text{drift}} < 720 \text{ ns}$. This may as well be caused by erroneous modelling of the drift gas during reconstruction or the fact that t_{drift} is recalculated from t_0 .

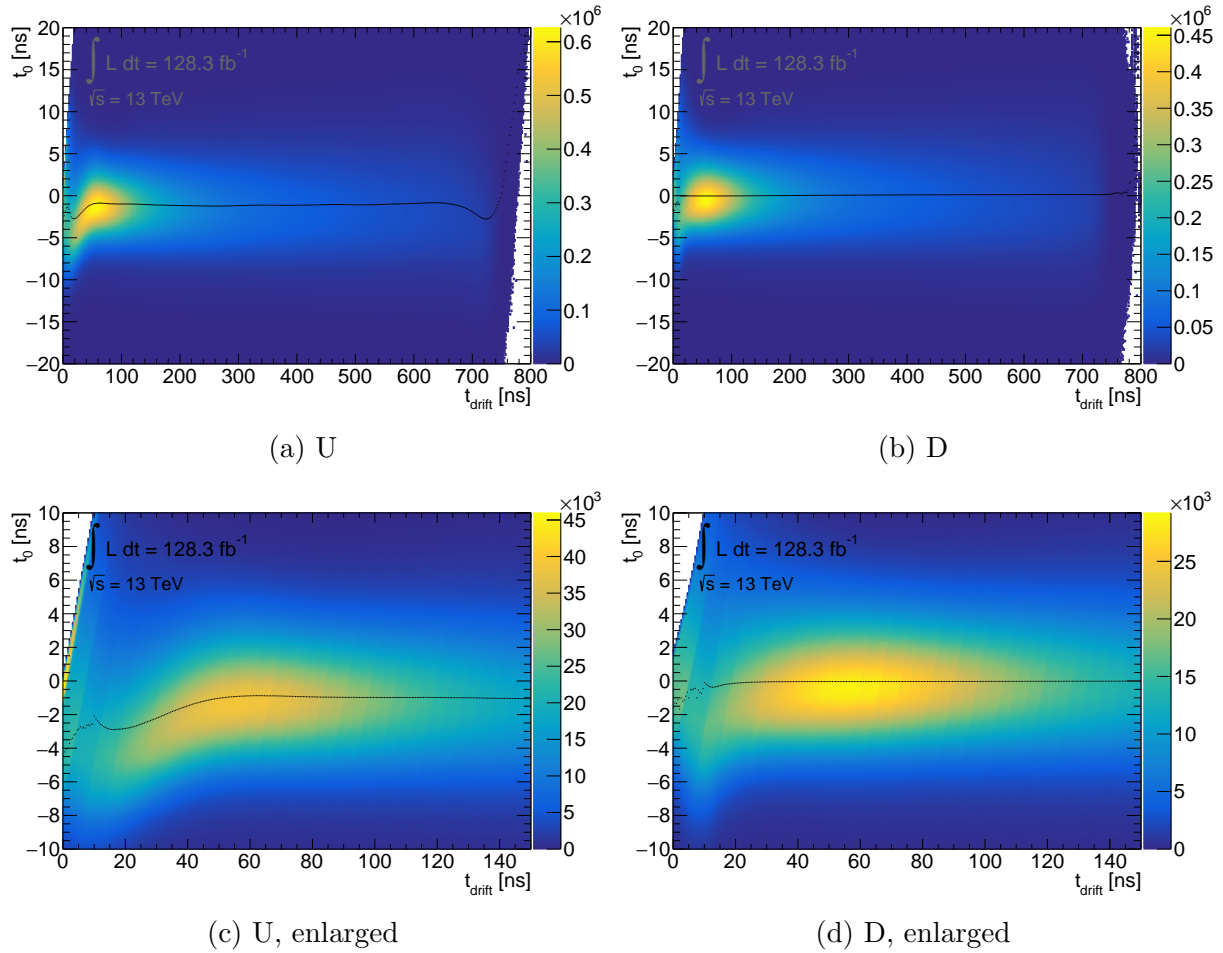


Figure 5.10: t_0 versus t_{drift} of hits in MDT tubes before (a) and after (b) drift-time calibration (U and D, respectively). (c) and (d) show the same distributions but with the region at low t_{drift} and simultaneously low $|t_0|$ enlarged. For each t_{drift} -bin, the mean of a Gaussian fit is drawn in black.

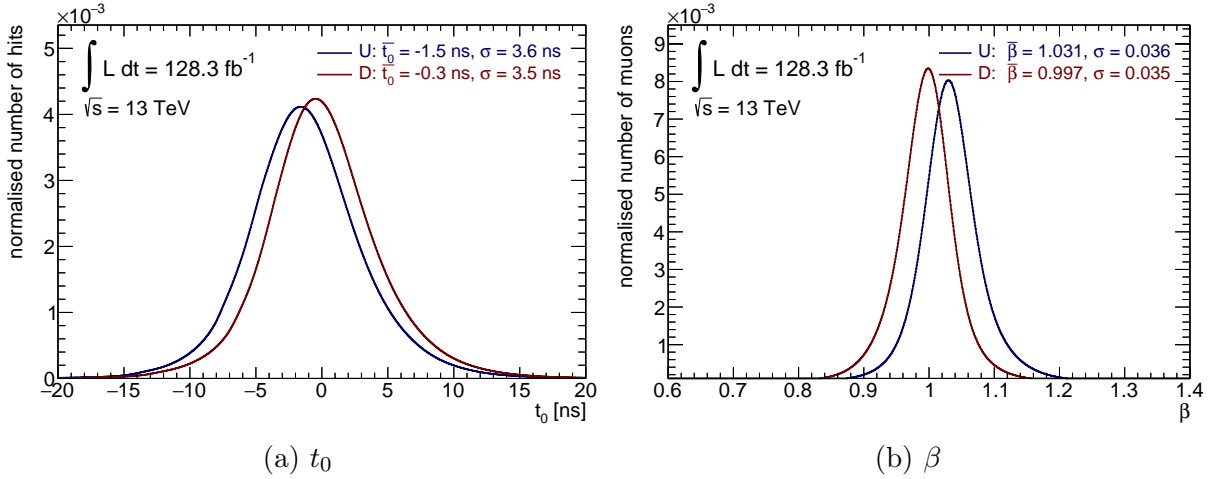


Figure 5.11: Comparison between uncalibrated (U, blue) and drift-time calibrated (D, red) MDT distributions for t_0 (a) and β (b). Given are also the mean and standard deviation of Gaussian fits using a reduced fitting window mean \pm RMS to the distributions.

Thus, there are a lot of effects that should be corrected for in this drift-time calibration step (symbol D). As the highly populated region at $t_0 > 2 \cdot t_{\text{drift}}$ is not understood and presumably not of physical origin, a cut is applied on t_0 rejecting all hits in the MDTs with $t_0 > 2 \cdot t_{\text{drift}}$. Thereby, 5.2% of MDT hits and 0.1% of candidates are lost.

Furthermore, as the other effects mentioned above cannot be corrected analytically, the means of the Gaussian fits, $\bar{t}_0(t_{\text{drift}})$, are taken as correction constants. The t_0 value after the drift-time calibration, t_0^{out} , can then be calculated from the t_0 value before the calibration, t_0^{in} , according to

$$t_0^{\text{out}} = t_0^{\text{in}} - \bar{t}_0(t_{\text{drift}}).$$

The t_0 - t_{drift} -distribution after this drift-time calibration is shown in Figures 5.10b and 5.10d. The overall mean of t_0 is clearly much more uniform than before the calibration. Only in the region with low t_{drift} and simultaneously low $|t_0|$ some distortions remain. The large improvements in t_0 and β can be seen in Figure 5.11: With the calibration, the means of the distributions get closer to expectation and the standard deviations of the Gaussian distributions decrease.

5.6 Propagation-time calibration

5.6.1 MDTs

Similar to the drift-time calibration, also a correction for the ϕ -dependence of the timing measurements in MDTs is needed: In Figure 5.12a the t_0 - ϕ -distribution shows a periodical sawtooth structure with a long and a short leg. The different lengths of the legs arise from

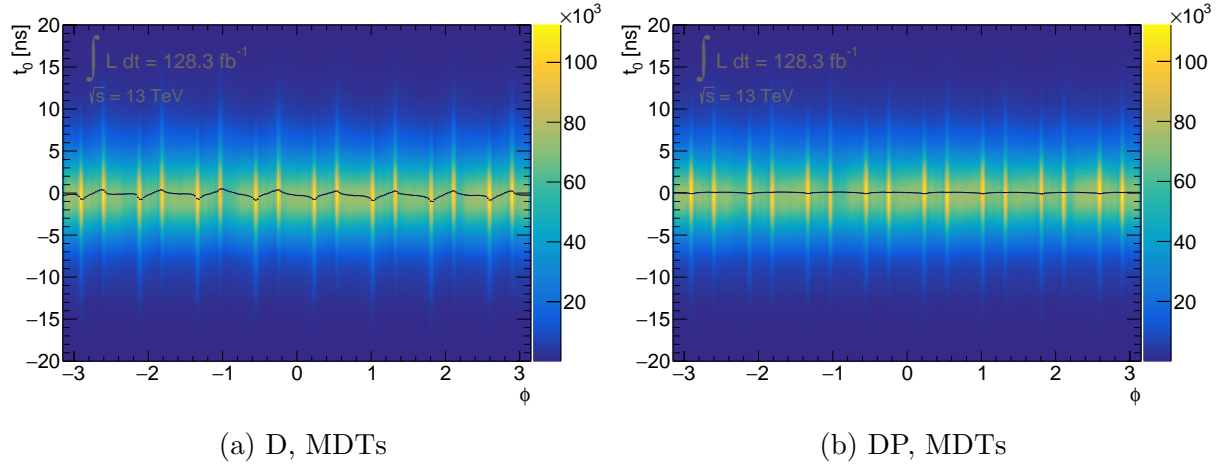


Figure 5.12: t_0 versus ϕ in the MDT end-caps after calibration of drift time only (a) and drift time as well as propagation time (b), denoted as D and DP, respectively. For each ϕ -bin, the mean of a Gaussian fit is drawn in black.

measurements in small (short legs) and large (long legs) sectors. In the overlap regions of these sectors naturally more hits are registered and the sawtooth structure is slightly distorted.

The sawtooth structure in the first place can be explained by the distance of a hit from the readout. As was mentioned in Section 3.2.3, in the end-caps, for example, the readout of neighbouring sectors are next to each other [67, 68], i.e., the readouts are located between large and small chambers. Thus, a hit registered at the maximum ϕ of a large chamber is very close to the readout and receives a small t_0 , while a hit at minimum ϕ of the same chamber is assigned a large t_0 , as the propagation time along the wire in the chamber is erroneously not taken into account. The same holds for small chambers, except the readout is located at the low- ϕ side of the chamber and the behaviour is therefore mirrored along ϕ . The picture is similar for the MDT barrel region but since the sawtooth structure depends on the position of the readout, which is not as periodic in ϕ in the barrel region as it is in the end-caps, the structure is less clearly visible.

The propagation-time calibration (symbol P) to correct for this effect is carried out station-wise to take into account the dependency of the readout position: For each MDT station, the mean per ϕ -bin, $\bar{t}_0(\phi)$, as derived from a Gaussian fit is taken as a correction function, i.e.,

$$t_0^{\text{out}} = t_0^{\text{in}} - \bar{t}_0(\phi).$$

After this calibration, $\bar{t}_0(\phi)$ is clearly more uniform, as can be seen in Figure 5.12b. While this does not cause a visible improvement in the overall MDT t_0 distribution, the β distribution becomes better compared to the β distributions before any as well as after drift-time

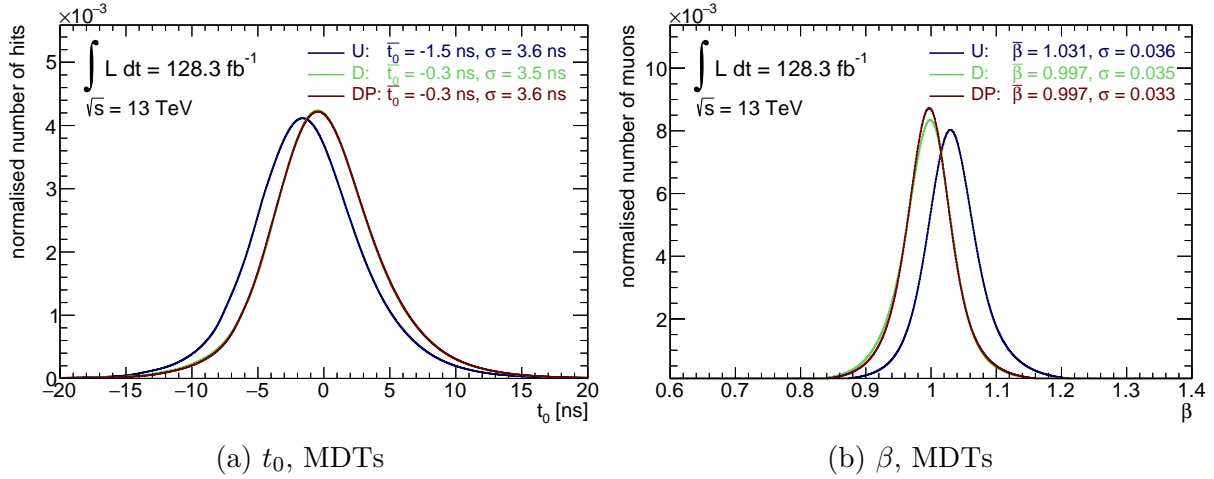


Figure 5.13: Comparison between uncalibrated (U, blue), drift-time calibrated (D, green) and propagation-time calibrated (DP, red) distributions for t_0 (a) and β (b) of MDT hits. Given are also the mean and standard deviation of Gaussian fits using a reduced fitting window $\text{mean} \pm \text{RMS}$ to the distributions.

calibration, as shown in Figure 5.13. The reason for this is that the timing information t_0 of some outlying hits in the distribution may be pushed towards values further away from zero, thereby preventing a numeric improvement of the fit. At the same time, β is much more sensible to values in the centre as an averaging over many timing measurements is performed. This allows the improvement to be seen in a decrease of the Gaussian fit's standard deviation.

5.6.2 RPCs

Also for RPCs, a correlation between t_0 and propagation time can be observed. Extensive studies have been carried out on this that are summarised in Appendix B. For RPC η -strips, such a correlation is shown in Figure 5.14a. A sawtooth structure is visible along ϕ , that is repeated multiple times along t_0 . When investigating this more closely, one observes that the structure is actually made of "V"-like shapes that are repeated periodically for each sector, i.e., 16 times, along ϕ . The bottom tip of the "V" thereby always corresponds to the centre of the sector in ϕ . This is caused by an imperfect calculation of the propagation time of the signal along the strip. As this calculation takes into account the splitting of RPC modules along ϕ in two RPC units, the sign of the slope for the left and right leg of the "V" arises. The repetition of the "V"s along t_0 is caused by the intrinsic RPC readout timing-granularity of 3.125 ns. There exists a substructure with a spacing of about 1.2 ns in t_0 , however, that is of unknown origin.

For RPC ϕ -strips, the readouts are not periodical in η but in z . Therefore, correlations

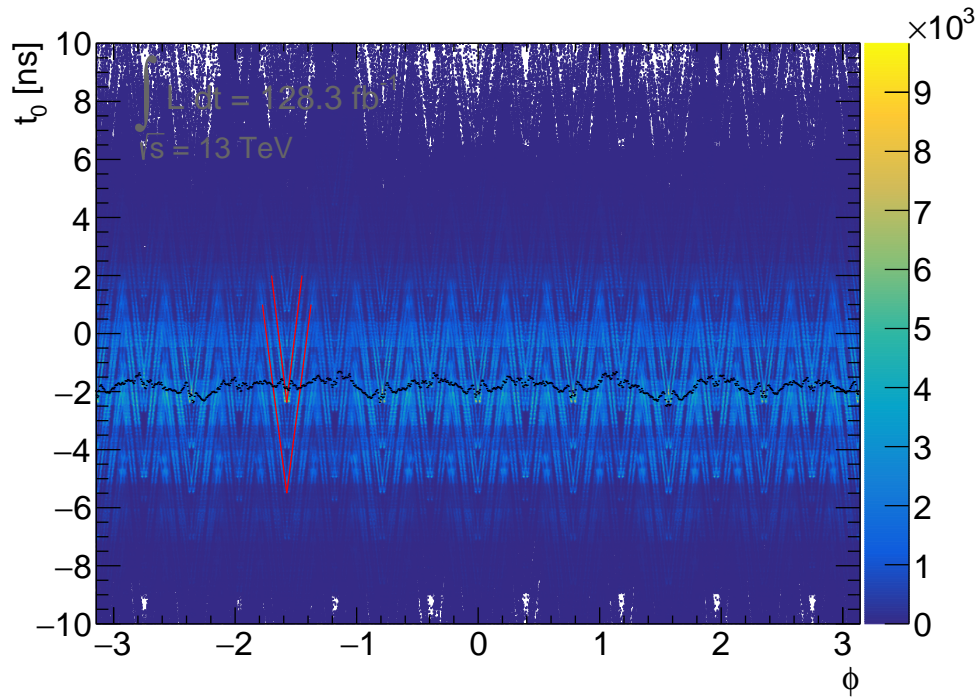
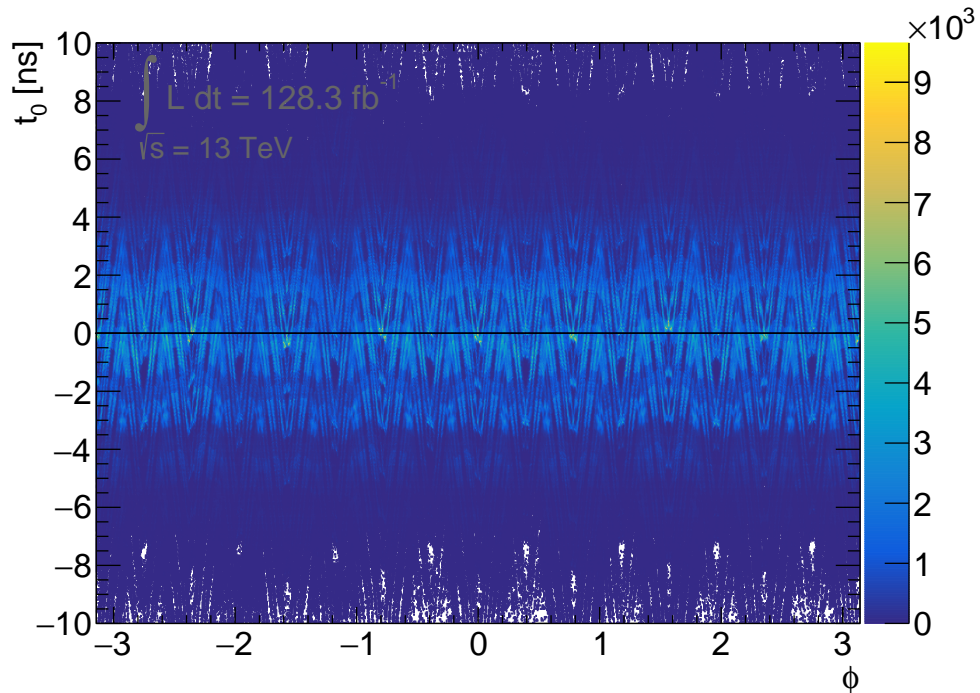
(a) U, RPC η -strips(b) P, RPC η -strips

Figure 5.14: t_0 versus ϕ of hits in RPC η -strips before (a) and after (b) propagation-time calibration (U and P, respectively). In (a) two of the periodically repeated, "V"-like structures along ϕ are marked in red. The means of the ϕ -bins are drawn in black.

exist between t_0 and z , as shown in Figure 5.15a. In contrast to RPC η -strip readouts, the location of the readouts for RPC ϕ -strips is different for the three detector layers as well as large and small sectors. Therefore, the structure is less clear for ϕ -strips than for η -strips. Nevertheless, a clear dependency of t_0 on z can be observed.

An attempt was made to fix these complex propagation-time dependencies analytically, which is also described in Appendix B. As it was unsuccessful, unfortunately, at least a slight reduction in the correlations is performed by subtracting the means of t_0 of these distributions as previously done for the MDTs. Hereby, the correction constants are derived in ϕ for η -strips and in z for ϕ -strips, of course. A splitting of the distributions by station did not yield any improvement and was therefore not carried out. Furthermore, the distributions per x -axis bin are undeniably not of a Gaussian shape. Therefore, no fit is attempted and just the mean per bin is taken as a correction constant.

The removal of the strongest correlations can be seen in Figure 5.14b for η -strips and in Figure 5.15b for ϕ -strips. This results in a small improvement in the standard deviations of the overall t_0 distributions, as shown in Figures 5.16a and 5.16b, as well as a large improvement in the β resolution (Figure 5.16c). In all three cases, also the mean is much closer to expectation than before the calibration.

5.7 Run-wise calibration

From here on, MDT tubes and RPC strips can be treated similarly. For a unification of the terms, in the following an *element* refers to the smallest unit of a MS system used for calibration, i.e., tubes for the MDT system and strips for the RPC systems.

Apart from the previous calibrations, the timing measurement is also subject to many effects that have a less defined behaviour and change from run to run and element to element. In principle, it would therefore be necessary in this step to derive calibration constants for each element and run simultaneously. This approach falls to two distinct obstacles, though. First, even when dropping the $Z \rightarrow \mu\mu$ selection criteria defined in Section 5.2, the amount of hits an element gets during a single run varies broadly. Thus, most often not enough hits are registered in data to allow for a meaningful calibration.

Second, with more than 735,000 elements that have registered hits and 560 runs available for calibration, the amount of data that would have to be processed in total for a substantial run-wise calibration for each element is just too large to be handled by memory and computing power at the time of writing.

Thus, the run-wise and element-wise calibration are not carried out simultaneously but in an iterative procedure.

Since the number of hits per run exceeds the number of hits per element by far, the run-wise distributions are less sensitive to outliers due to uncalibrated elements and the run-wise calibration (symbol R) is chosen to be the first calibration step of the two in question.

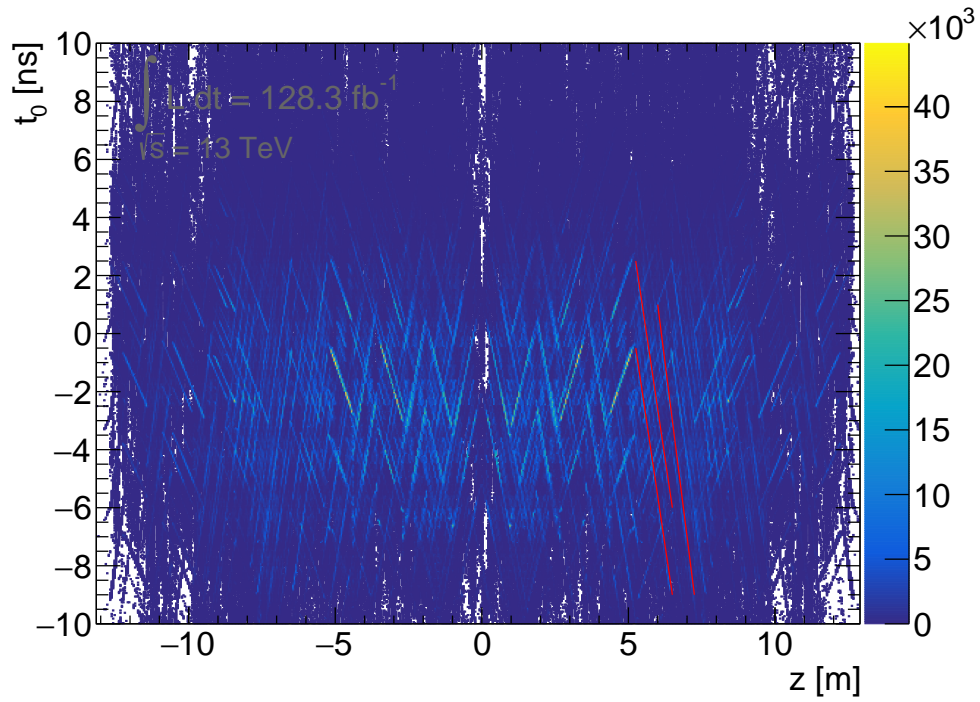
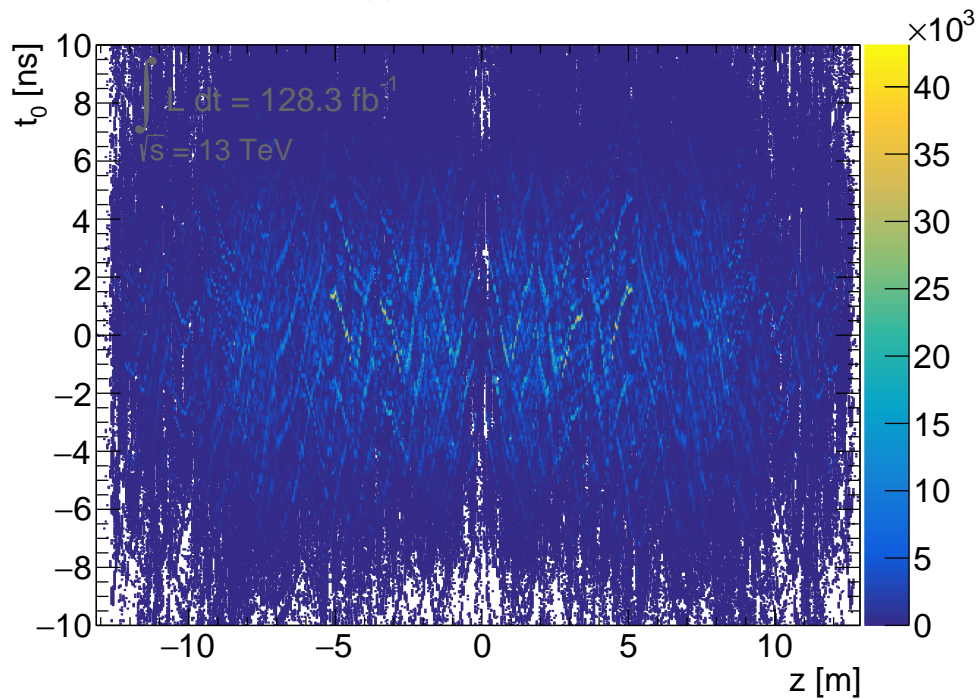
(a) U, RPC ϕ -strips(b) P, RPC ϕ -strips

Figure 5.15: t_0 versus z of hits in RPC ϕ -strips before (a) and after (b) propagation-time calibration (U and P, respectively). A few selected dependencies of t_0 on z are marked in red.

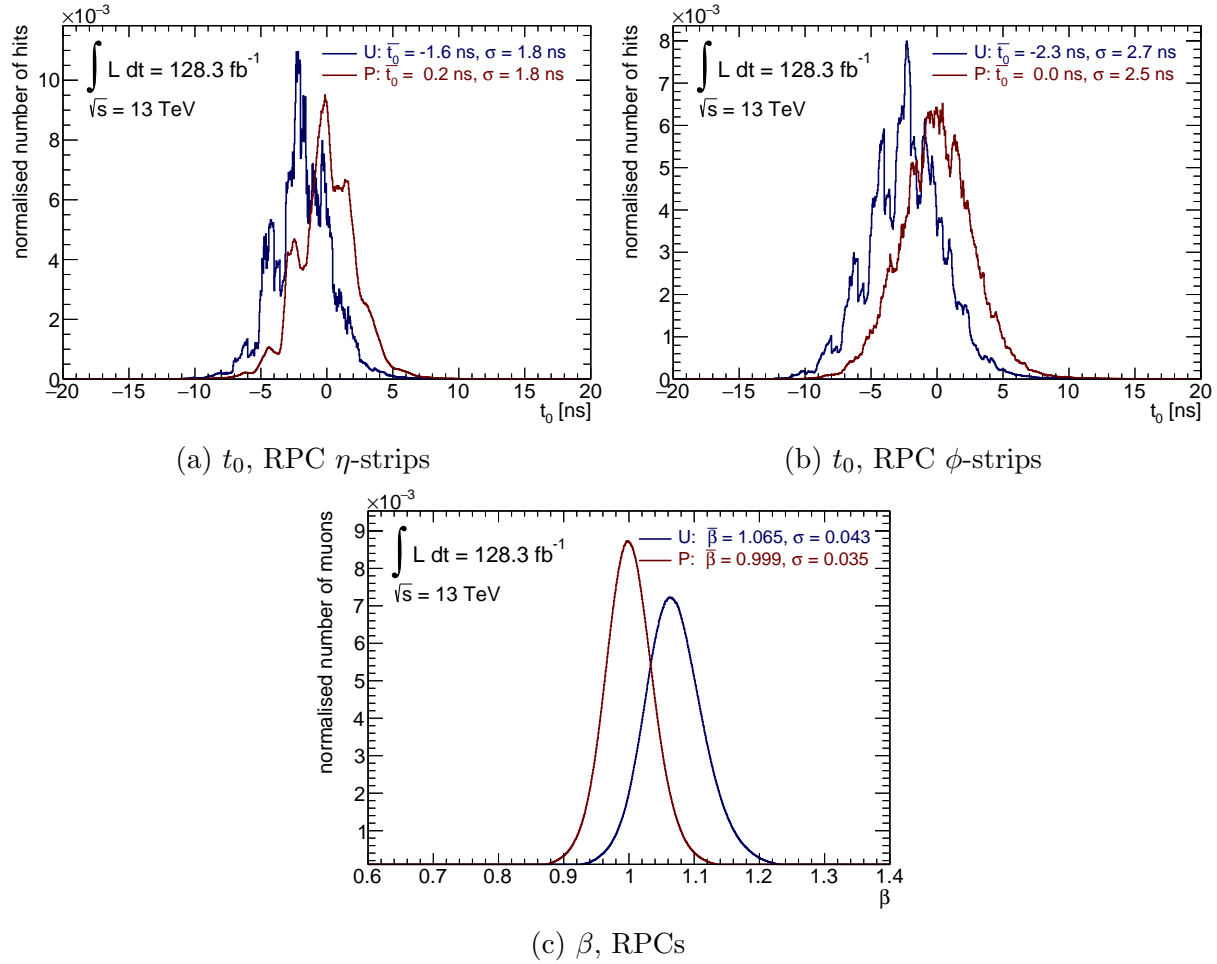


Figure 5.16: Comparison between uncalibrated (U, blue) and propagation-time calibrated (P, red) distributions for t_0 of hits in the RPC η -strips (a), t_0 of hits in the RPC ϕ -strips (b) and β of muons in the combined RPC systems (c). Given are also the mean and standard deviation of Gaussian fits using a reduced fitting window $\text{mean} \pm \text{RMS}$ to the distributions.

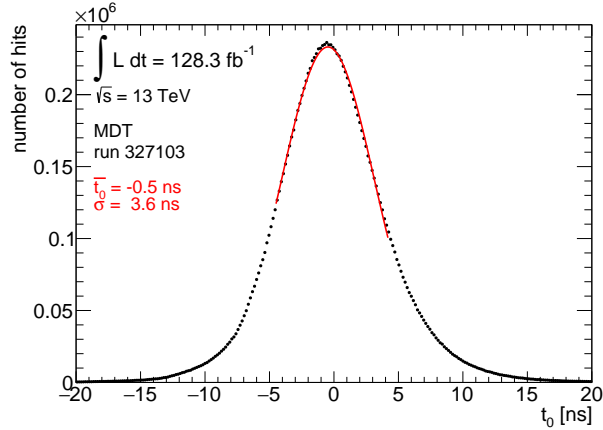


Figure 5.17: t_0 distribution (black dots) for a randomly chosen run. A Gaussian distribution (red line) is fitted within the range $\text{mean} \pm \text{RMS}$ to the t_0 distribution, providing the given standard deviation and mean.

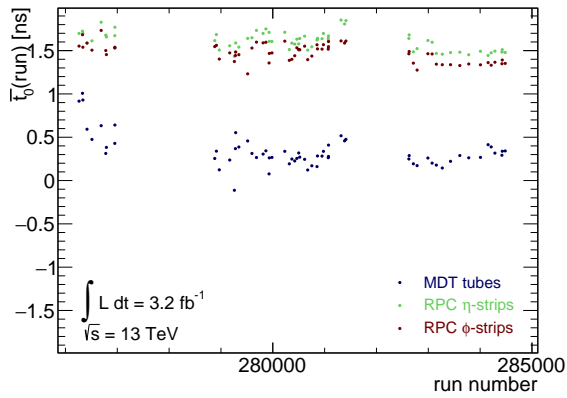
This helps in harmonising hits for the single elements before the imminent element-wise calibration.

As large differences are expected between MDTs, RPC η - and RPC ϕ -strips, those systems are treated separately. Accordingly, for each run and each of the three systems, the timing information t_0 of all hits are registered. Then, Gaussian fits with the reduced fitting window $\text{mean} \pm \text{RMS}$ are applied. The means of those, $\bar{t}_0(\text{run})$, are taken as calibration constants, i.e.,

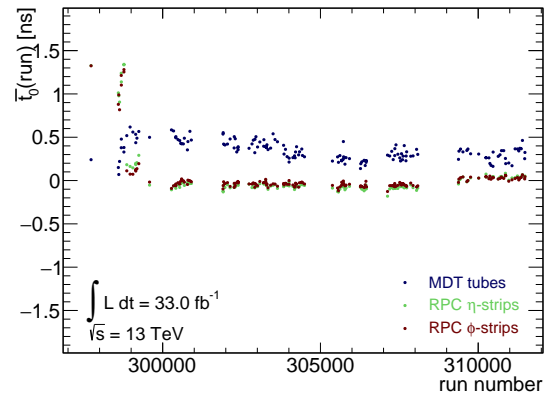
$$t_0^{\text{out}} = t_0^{\text{in}} - \bar{t}_0(\text{run}).$$

The t_0 distribution for a randomly chosen run and the fitted curve is shown in Figure 5.17. Figure 5.18 depicts the arising calibration constants.

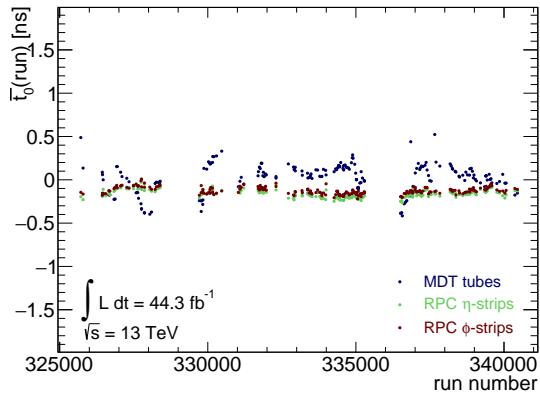
With this, no visible improvement in the standard deviation and mean of the t_0 distribution for each of the three system is achieved, as shown in Figure 5.19. However, this calibration step causes a minor improvement in the β resolutions that does not express itself in the numerical values but is visible to the eye, as shown in Figure 5.20.



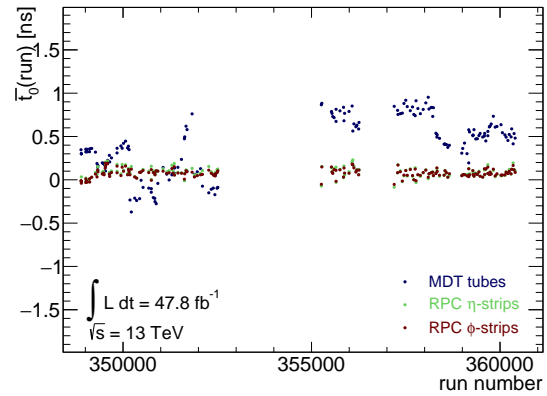
(a) 2015 runs



(b) 2016 runs



(c) 2017 runs



(d) 2018 runs (up to 24th September)

Figure 5.18: Mean t_0 (\bar{t}_0) per run for the MDT tubes (blue), RPC η -strips (green) and RPC ϕ -strips (red), separated into the different years in which the runs took place.

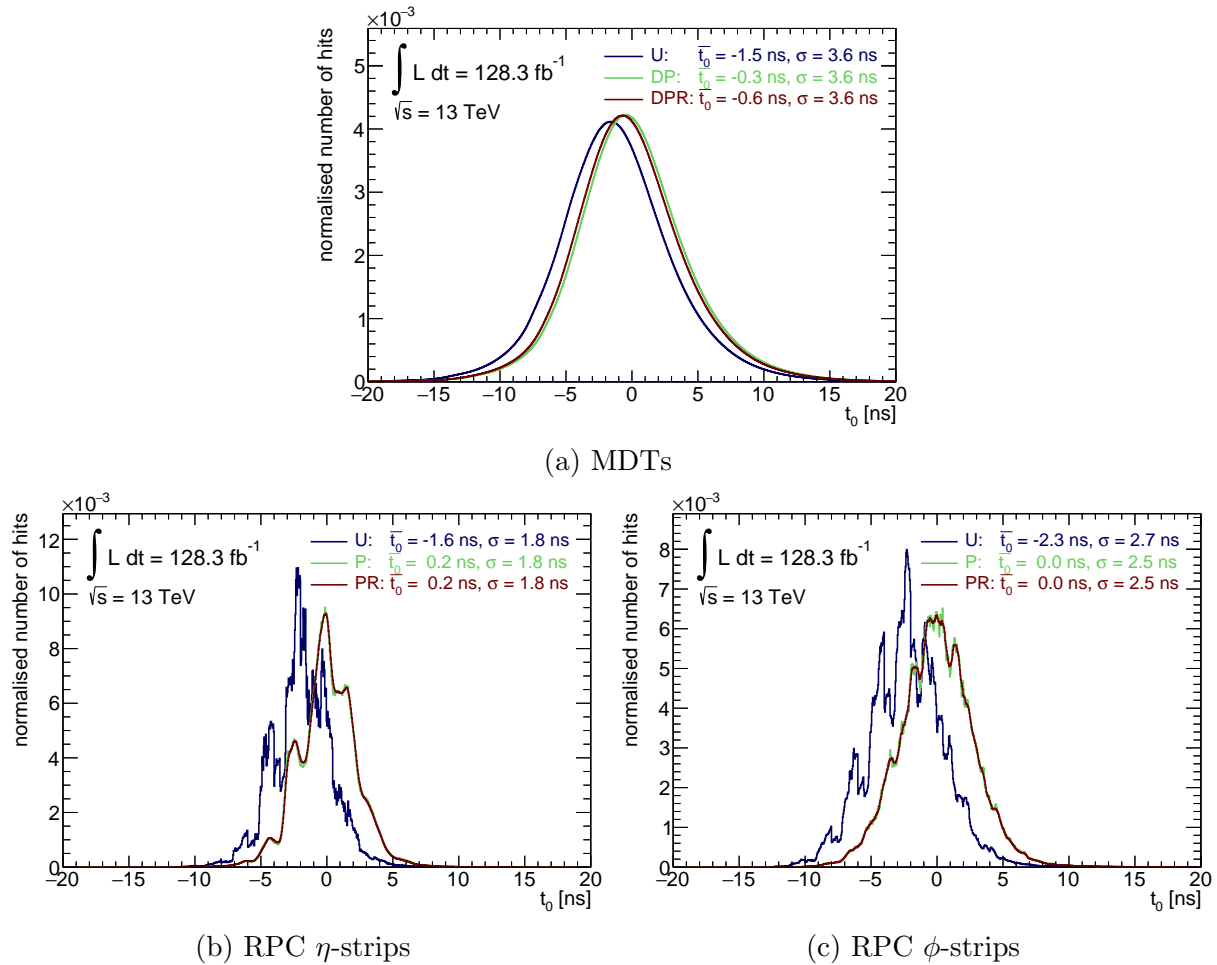


Figure 5.19: Comparison between uncalibrated (U, blue) t_0 distributions as well as t_0 distributions directly before (DP or P, green) and after (DPR or PR, red) run-wise calibration. Drawn are the distributions for MDTs (a), RPC η -strips (b) and RPC ϕ -strips (c). Given are also the mean and standard deviation of Gaussian fits using a reduced fitting window $\text{mean} \pm \text{RMS}$ to the distributions.

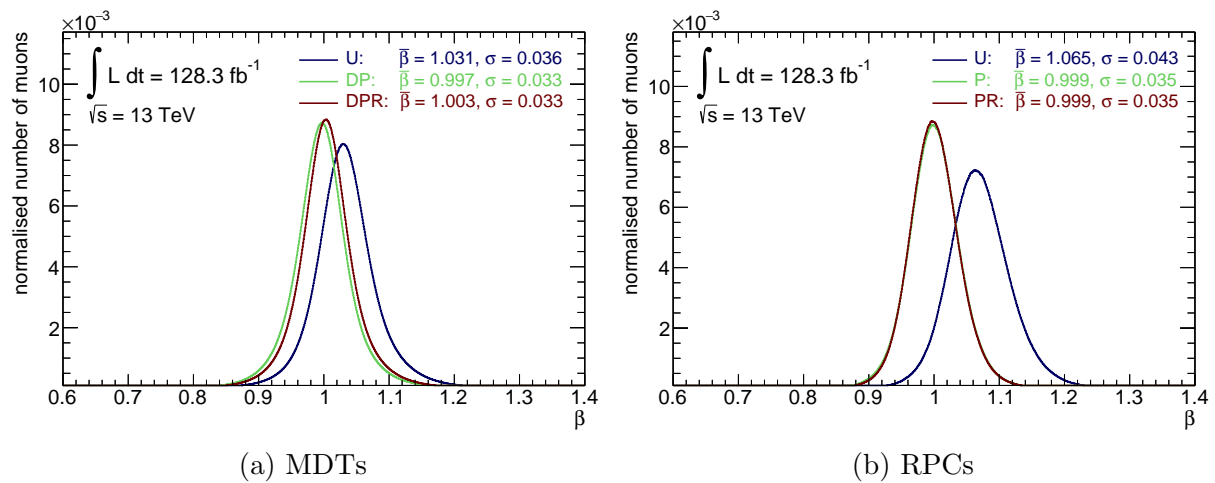


Figure 5.20: Comparison between uncalibrated (U, blue) β distributions as well as β distributions directly before (DP or P, green) and after (DPR or PR, red) run-wise calibration. Drawn are the distributions for the MDT (a) and RPC (b) system. Given are also the mean and standard deviation of Gaussian fits using a reduced fitting window $\text{mean} \pm \text{RMS}$ to the distributions.

5.8 Element-wise calibration

Each detector system consists of several elements: Tubes for the MDT system and strips for the RPC system, respectively. To adjust for minor differences between detector elements, an element-wise calibration (symbol E) is carried out. For this, the timing information t_0 of all hits across all runs is stored for each element.

To derive calibration constants from those timing distributions can be difficult because in contrast to the run-wise timing distributions, much less hits are registered. To compensate at least for some of this, the $Z \rightarrow \mu\mu$ selection criteria defined in Section 5.2 have to be dropped, enabling much larger statistics. In fact, the average number of hits per MDT tube increases from about 8,400 to 71,000, the average number of hits per RPC η -strip from approximately 2,200 to 18,000 and per RPC ϕ -strip from about 1,000 to 7,900. Still, the t_0 distributions are less smooth than for the previous calibration steps, outliers can bias the fitting procedure more easily and a too refined binning can affect the fit negatively.

To account for all of this, a multi-fit procedure has been developed that works as follows.

1. Elements that have less than 40 registered hits in total are rejected because neither a stable fitting procedure nor a reliable mean can be assured for those. An example for such a t_0 distribution of an element can be found in Figure 5.21a.
2. RPC strips with an RMS larger than 10 ns are rejected because those show a peculiar timing distribution, as can be seen in Figure 5.21b, for example. Since the timing resolution of MDTs is worse than that of RPCs and thus the expected RMS for MDTs is larger, no cut on the RMS is applied for MDTs.
3. The timing distributions of all remaining elements are fitted five times with different fitting conditions:
 - (a) A plain Gaussian fit over the full permitted t_0 range $[-80 \text{ ns}; 80 \text{ ns}]$. This can be considered the default procedure and usually looks like the example given in Figure 5.21c.
 - (b) A Gaussian fit within the range $[-18 \text{ ns}; 18 \text{ ns}]$. This takes care of elements, which have registered a considerably large number of outliers. The choice of the range is motivated by the bunch spacing of 25 ns, giving rise to a range of $[12.5 \text{ ns}; 12.5 \text{ ns}]$ per bunch crossing. The fitting windows was then enlarged beyond this to take the width of the t_0 distributions of up to several nanoseconds into account. The exact value of $[-18 \text{ ns}; 18 \text{ ns}]$ was determined empirically by choosing the range which resulted in the most successful fits for elements the other fit methods did not converge for.
 - (c) A Gaussian fit centred at the bin with the maximum content and within the range $\pm \text{RMS}$. This allows for stable fitting of elements with a strongly displaced mean or a second peak due to misadjustments in the timing measurements for some period of time. The distribution for an example element that exhibits both of this is shown in Figure 5.21d.

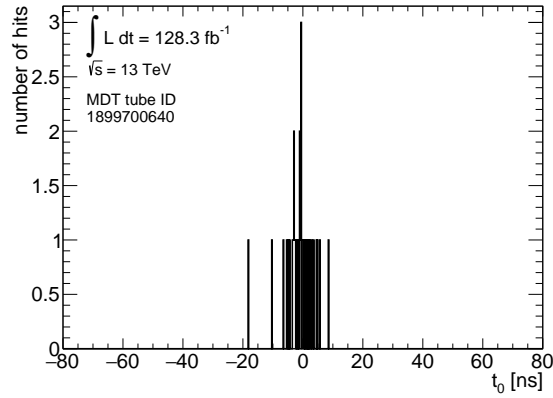
- (d) A rebinning of the histogram summing neighbouring bins is carried out. Afterwards a plain Gaussian fit over the full range is applied. This accounts for elements with small statistics that are spread out over a large range of t_0 values.
 - (e) The same procedure as in the previous rebinning method but always four bins are summed into a new one. This allows to take elements with even smaller statistics into account.
4. Fits which fail or have $\chi^2/\text{ndof} > 300$, where ndof is the fit's number of degrees of freedom, are discarded. For RPCs, also those with a suspiciously high resolution, i.e., σ_{t_0} almost as small as the bin width ($\sigma_{t_0} < 0.2 \text{ ns}$), are not considered. This is not necessary for MDTs because of the intrinsically worse resolution.
 5. Of the remaining fits, for each element the one with the least χ^2/ndof is chosen and its mean and σ_{t_0} are taken as calibration constants. In general, fits with a similarly low χ^2/ndof are observed to also exhibit comparable values for mean and σ_{t_0} . If no fit passed the above criteria, the mean of the histogram and the RMS are taken.

Figure 5.22 shows the fraction of elements and hits that are completely rejected or fitted with one of the above explained fit methods. It can be noted that in general the fraction of elements that can be fitted with a certain method or have to be rejected is dependent on the number of hits for those element: For MDT tubes, which receive most hits, the need for specialised treatment or no valid treatment is lower than that for RPC η -strips, which receive the second most hits. The highest fraction of specially treated elements is in RPC ϕ -strips, which have the lowest average number of registered hits. Still, the fraction of elements that have to be treated with a special method or rejected is always in the percent or subpercent level.

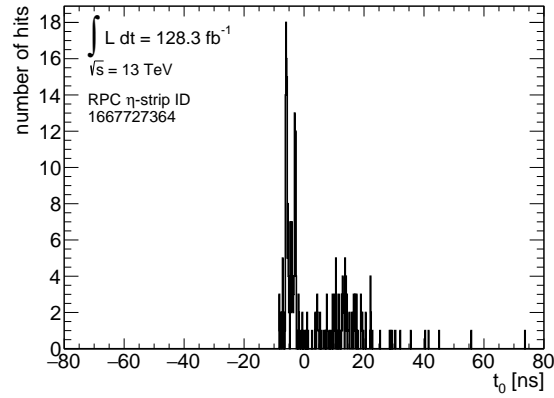
As the special treatment requirement or rejection for an element is dependent on the number of hits for this element, naturally, the fraction of hits that are rejected or registered by a special-treated element is even lower. All in all, only a very small amount of hits has to be rejected in this calibration step. The large improvement in standard deviations and means of the t_0 distributions can be seen in Figure 5.23. Noticeable is that with this calibration step the visibility of the RPC readout timing-granularity disappears because lots of strips receive small corrections that wash out the previously visible peaks.

After this fitting step, for each non-rejected element the width of the t_0 distribution is known, either by σ of the fit or by taking the RMS, which is in general larger. These values can then be considered the uncertainty σ_{t_0} of the timing measurements for a certain element. In consequence, it is now also possible to apply a consistency cut and reject those timing measurements for a muon that are in complete disagreement with the other measurements for the same muon. For this, the mean β^{-1} of all β_i^{-1} values for the different hits of each muon is calculated for each system according to equation (5.3). Afterwards, only hits fulfilling

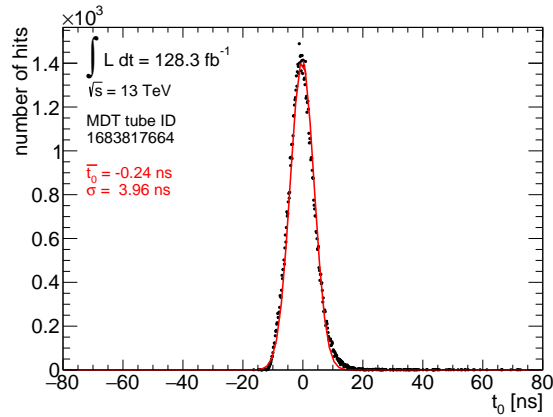
$$|\beta^{-1} - \beta_i^{-1}| \leq 3 \cdot \sigma_{\beta^{-1}},$$



(a) rejected: too few hits



(b) rejected: too large RMS



(c) default fit

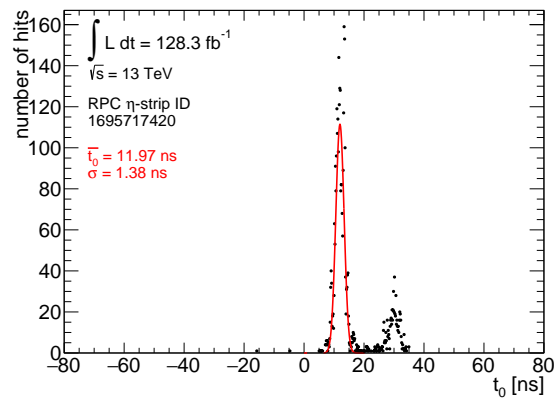
(d) fit with fixed mean and in range \pm RMS

Figure 5.21: Example t_0 distributions (black) as obtained for randomly chosen detector elements. Elements are rejected because of too few hits (a) or a too large RMS (b). Others are fitted with a plain Gaussian distribution (c) or specially treated, e.g., by a fit with a Gaussian distribution centred at the bin with maximum content and in the range \pm RMS (d). Observed distributions are marked in black. The fit, if performed, is drawn in red and the according fit parameters are stated.

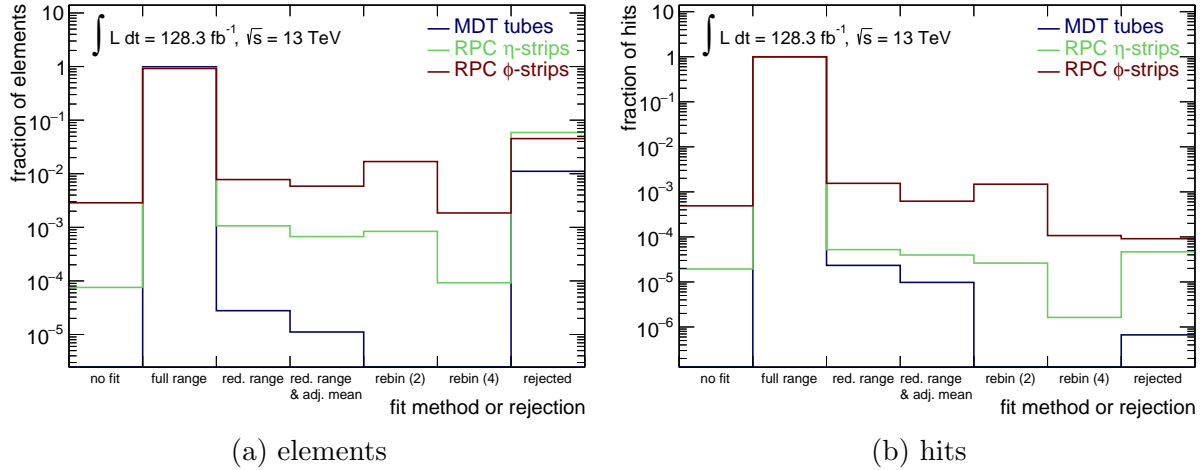


Figure 5.22: Fraction of elements (a) and hits (b) that a certain fit method is chosen for or that are rejected. Fractions are given for MDT tubes (blue), RPC η -strips (green) and RPC ϕ -strips (red). Note the logarithmic scale on the y -axis.

where $\sigma_{\beta^{-1}}$ is the uncertainty of β^{-1} , are considered for the final β distribution. For MDTs, 5.0% of hits are discarded this way, for RPCs 1.3%. Naturally, this number is lower for RPCs as there are less available hits and therefore the weight of each hit is higher. In total, 0.1% of candidates are lost in this calibration step due to the various cuts.

With the consistency check in addition to the calibration constants derived for each detector element, another large progress in optimising standard deviations and means of the β distributions is achieved as is shown in Figure 5.24. In this step, the better timing resolution of RPCs comes into effect, surpassing the β resolution of MDTs, at last.

5.9 Second run-wise calibration

As run-wise and element-wise calibration should be carried out in parallel, ideally, it is imaginable that a second run-wise calibration after the element-wise calibration is needed to obtain the full correction power of the run-wise calibration. However, when calculating the correction constants $\bar{t}_0(\text{run})$, one immediately recognises that this is not the case: While in the first run-wise calibration the correction constants could exceed 1.8 ns, as was shown in Figure 5.18, the correction constants for the second run-wise calibration are consistently below 0.3 ns. Indeed, when investigating the β distributions before and after the second run-wise calibration, as is done in Figure 5.25, no improvement in the β resolution can be observed. In fact, for MDTs even a slight over-calibration can be noted.

Apart from this, in principle, it is also possible that conducting the element-wise calibration before the first run-wise calibration (and without a second run-wise calibration), i.e., a

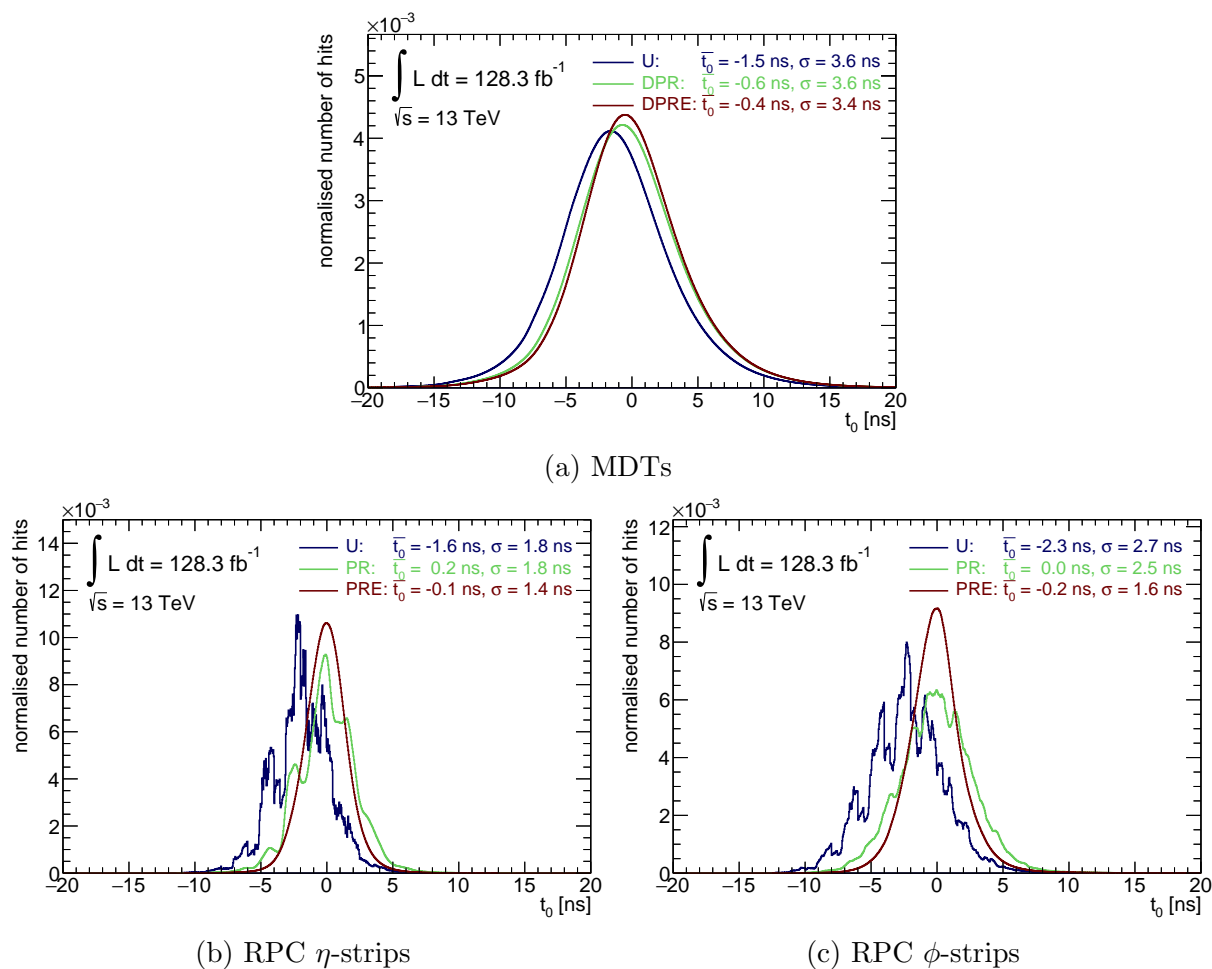


Figure 5.23: Comparison between uncalibrated (U, blue) t_0 distributions as well as t_0 distributions directly before (DPR or PR, green) and after (DPRE or PRE, red) element-wise calibration. Drawn are the distributions for MDTs (a), RPC η -strips (b) and RPC ϕ -strips (c). Given are also the mean and standard deviation of Gaussian fits using a reduced fitting window mean \pm RMS to the distributions.

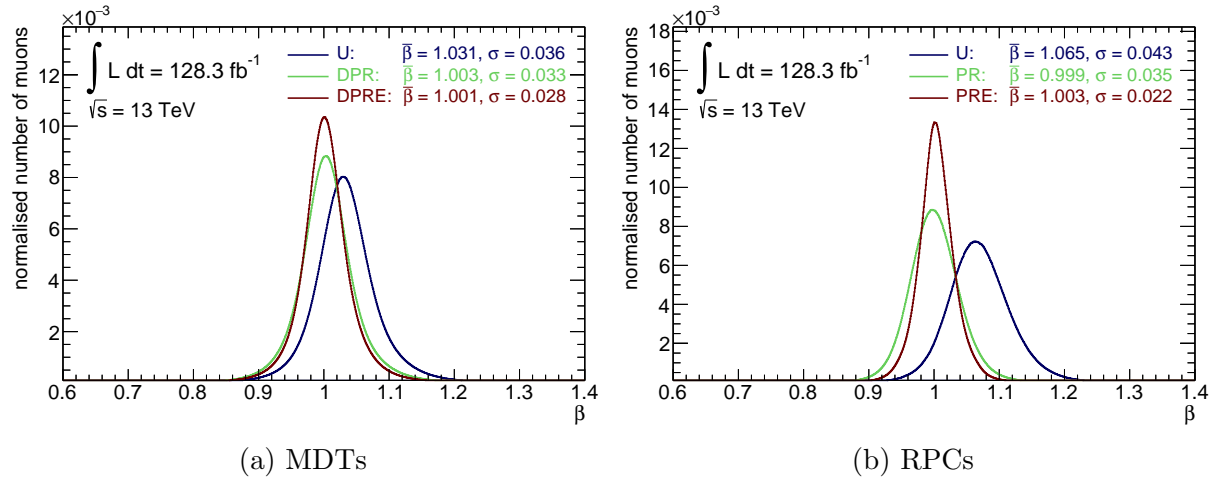


Figure 5.24: Comparison between uncalibrated (U, blue) β distributions as well as β distributions directly before (DPR or PR, green) and after (DPRE or PRE, red) element-wise calibration. Drawn are the distributions for the MDT (a) and RPC (b) system. Given are also the mean and standard deviation of Gaussian fits using a reduced fitting window $\text{mean} \pm \text{RMS}$ to the distributions.

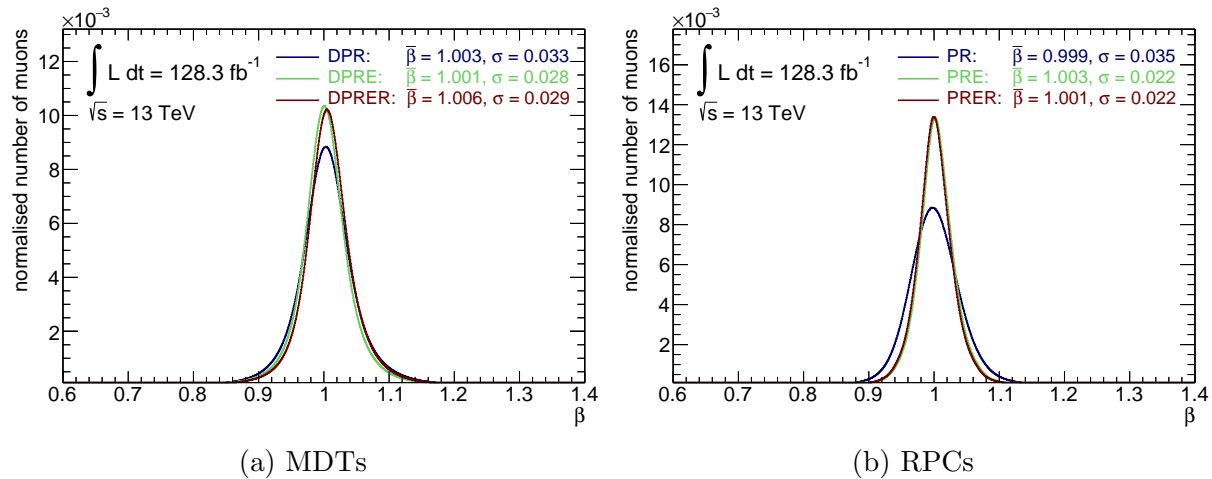


Figure 5.25: Comparison between β distributions directly after first run-wise calibration (DPR or PR, blue), after element-wise calibration (DPRE or PRE, green) and after second run-wise calibration (DPRER or PRER, red). Drawn are the distributions for the MDT (a) and RPC (b) system. Given are also the mean and standard deviation of Gaussian fits using a reduced fitting window $\text{mean} \pm \text{RMS}$ to the distributions.

DPER calibration procedure, would yield a better β resolution than the order as presented in the sections above (DPRE). Switching the order of run- and element-wise calibration step was already tested in the previous calibration but did not yield better results. The same is apparently true for the new calibration: Given the first run-wise calibration does not worsen the distributions, an improvement in the distributions for the DPRER calibration order can be expected if DPER obtained an improvement. As this is not the case, the presented order of calibrations is kept and the second run-wise calibration omitted in the following.

5.10 Pull correction and final β resolution

Before combining the results of the RPC and MDT system in a meaningful way is possible, it has to be assured that the σ_β of the β measurements accurately represent the measurement uncertainties. For this, the *pull* distributions,

$$p := \frac{1 - \beta_i^{-1}}{\sigma_{\beta_i^{-1}}},$$

are analysed and calibrated (symbol S, for σ). If the measurement uncertainties are reflected correctly by $\sigma_{\beta_i^{-1}}$, the pull distributions are known to be Gaussian shaped with mean zero and standard deviation one.

The pull distributions for MDT tubes as well as RPC η - and ϕ -strips can be found in Figure 5.26. As they do not agree perfectly with expectation, a correction constant for σ_β^{-1} for each of the three systems is derived. They range from $\sigma_p = 0.94$ for MDTs over $\sigma_p = 1.09$ for RPC η -strips to $\sigma_p = 1.15$ for RPC ϕ -strips. Applying those to the β measurements results in much better pull distributions as is also shown in Figure 5.26. However, this does not visibly affect the β distributions for MDTs or RPCs, as can be seen in Figure 5.27. There, also the β distribution for the combined muon spectrometer systems is shown. Accordingly, the calibration procedure described in this work yields the final result

$$\beta^{\text{MS}} = 1.002, \quad \sigma_\beta^{\text{MS}} = 0.022.$$

This is better than the β resolution of $\sigma_\beta = 0.024$ used in searches for charged SMPs in 2015 [80]. In comparison to the most recent calibration, which was presented in [95] and achieved a nominal β resolution of $\sigma_\beta^{\text{MS}} = 0.021$, this is nominally worse by about 5%. However, this is presumably well within the uncertainties of the β resolutions. Nevertheless, even a worse β resolution would not be completely unexpected: On the one hand, due to the clustering of hits in R21 less hits are available for calibration. This could explain a slightly worse β resolution for RPCs. On the other hand, the uncalibrated β distributions exhibited a significantly worse β resolution in R21 than in R20.7 from the beginning, partly due to the missing MDT hits, as will be discussed in the following section. In consequence, only a final β resolution of $\sigma_\beta = 0.028$ for MDTs was achieved. This is significantly

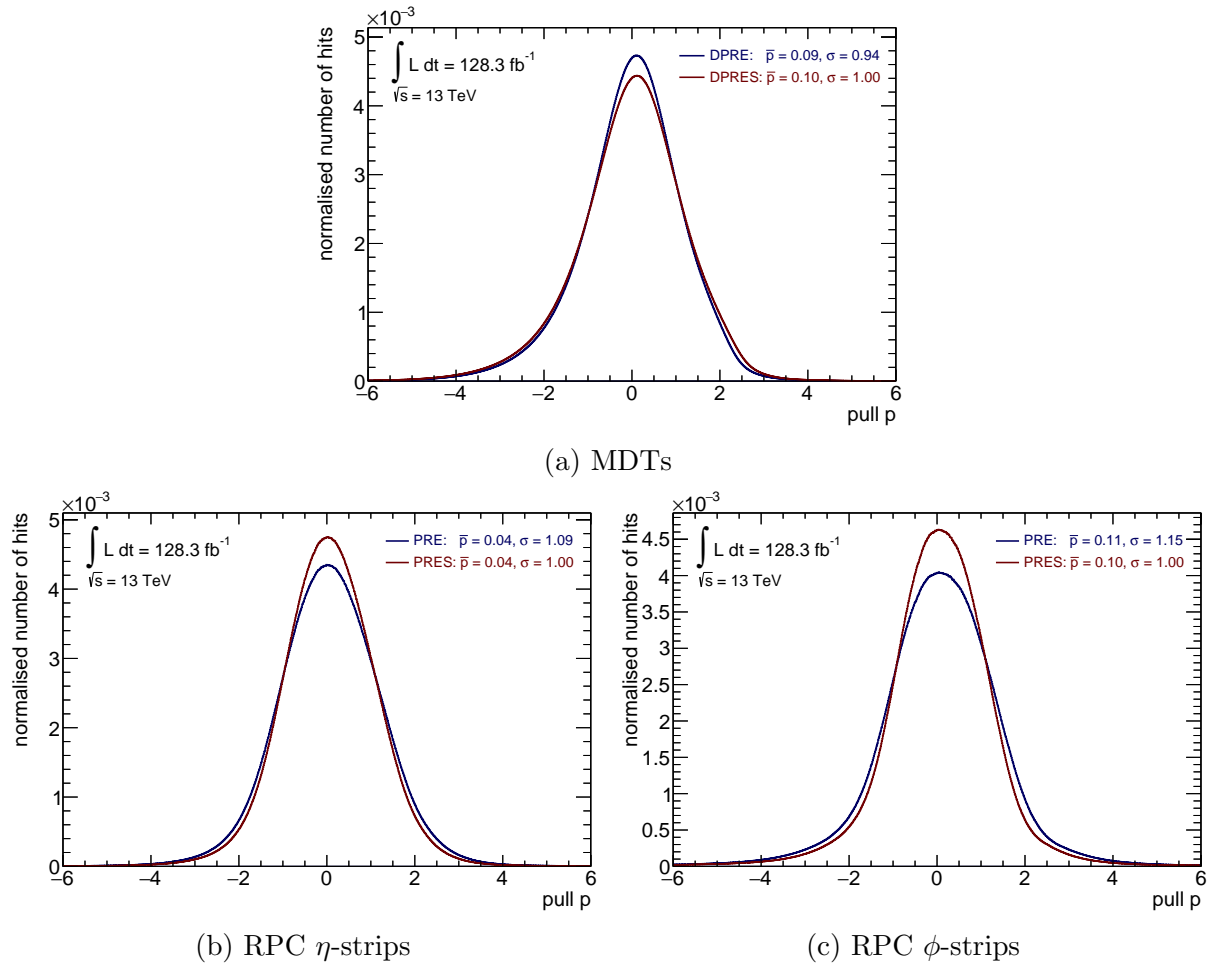


Figure 5.26: Comparison between pull distributions directly before (DPRE or PRE, blue) and after (DPRES or PRES, red) pull correction. Drawn are the distributions for MDTs (a), RPC η -strips (b) and RPC ϕ -strips (c). Given are also the mean and standard deviation of Gaussian fits using a reduced fitting window $\text{mean} \pm \text{RMS}$ to the distributions.

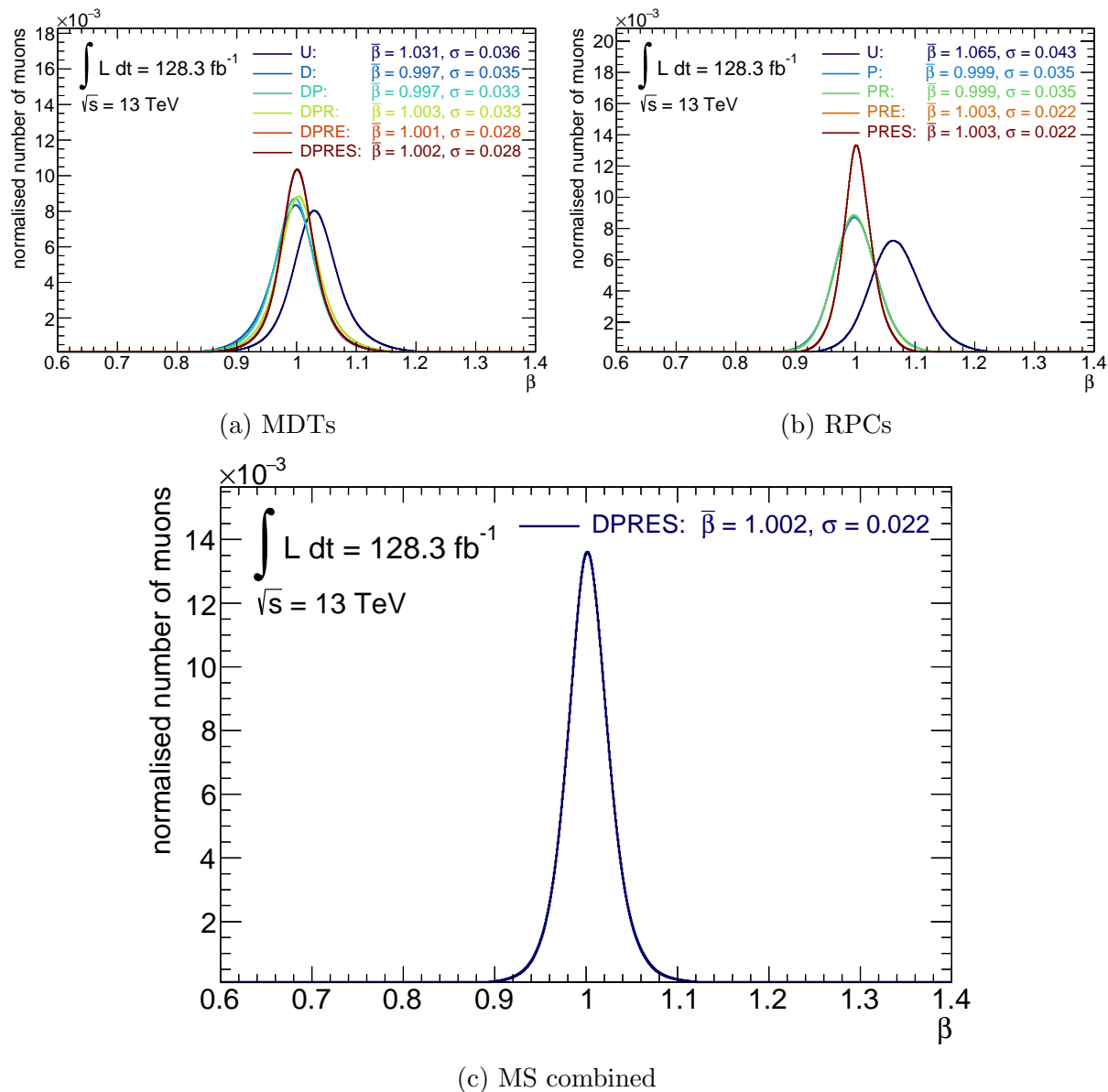


Figure 5.27: Comparison between uncalibrated β distributions as well as β distributions after each intermediate calibration step. Drawn are the distributions for MDTs (a) and RPCs (b). For the combined β estimate (c) only the β distribution after the last calibration step is given as no meaningful combination of systems is possible before the pull calibration step. Given are also the mean and standard deviation of Gaussian fits using a reduced fitting window mean \pm RMS to the distributions.

lower than in the most recent calibration presented in [95], where $\sigma_\beta = 0.026$ could be obtained for MDTs. Nevertheless, this is a much smaller discrepancy than it was before the calibration ($\sigma_\beta = 0.030$ in [95], $\sigma_\beta = 0.036$ in this work), which can be seen as a success of the calibration procedure described in the work at hand. Unfortunately, however, the low final β resolution in MDTs completely prevents an improvement in the β resolution when combining MDT and RPC system.

5.11 Evaluation of the impact of missing MDT hits

As was mentioned in Section 4.4.1, in the course of this work it was discovered that for particles reconstructed with MUGIRLLOWBETA in R21 less hits are registered in MDTs in the barrel region of ATLAS' side C than of side A. This has a large influence on the final β resolution for MDTs in the barrel region achieved by the calibration and can also impact the combined β resolution. Therefore, the β distribution obtained in the barrel region in ATLAS' side C is compared with the β distribution in side A as shown in Figure 5.28. Note that the distribution labelled as "all" is still derived only from hits in the barrel and therefore differs from the distributions shown in previous plots. When considering only MDTs, the β resolution achieved on side A is clearly — by about 18% — better than that on side C. The overall β distribution lies in-between those two extremes. When combining the MDT β estimate with that obtained in the RPC system, however, much of the lost accuracy can be recovered on side C: Here, the difference between the side-A and side-C β resolution is much smaller. Nevertheless, the β resolution on side C is still by about 5% lower than that of side A, which could explain a slightly lower β resolution achieved in this calibration compared to the previous one. It is to be decided in the future if this difference is worth a reprocessing of the data as soon as the bug is fixed in reconstruction.

5.12 Comparison between the years

Between the years 2015–2018, the mean number of interactions per bunch crossing, i.e., the pile-up profiles, changed drastically, as can be seen in Figure 5.29a. As this also has an impact on the background for reconstruction, it is plausible that also the β resolution is actually some function of time. Thus, it is sensible to compare the results for the β resolution for the different periods of data-taking. The largest differences in the pile-up can be seen between the data-taking period 2015–2016 and the period 2017–2018. Therefore, in a first step the whole calibration chain is conducted separately for the data taken in 2015–2016. An even more meaningful result could be expected from separating only the data taken in 2015, of course, but unfortunately, the integrated luminosity of merely 3.2 fb^{-1} does not allow for a successful calibration as described in this chapter based on just this dataset. The final β resolution achieved for the period 2015–2016 can be seen in Figure 5.29b. Apparently, a decrease in the mean pile-up from the whole data-taking period 2015–2018, $\langle\mu\rangle = 34.0$, to the mean pile-up $\langle\mu\rangle = 23.7$ of the years 2015–2016

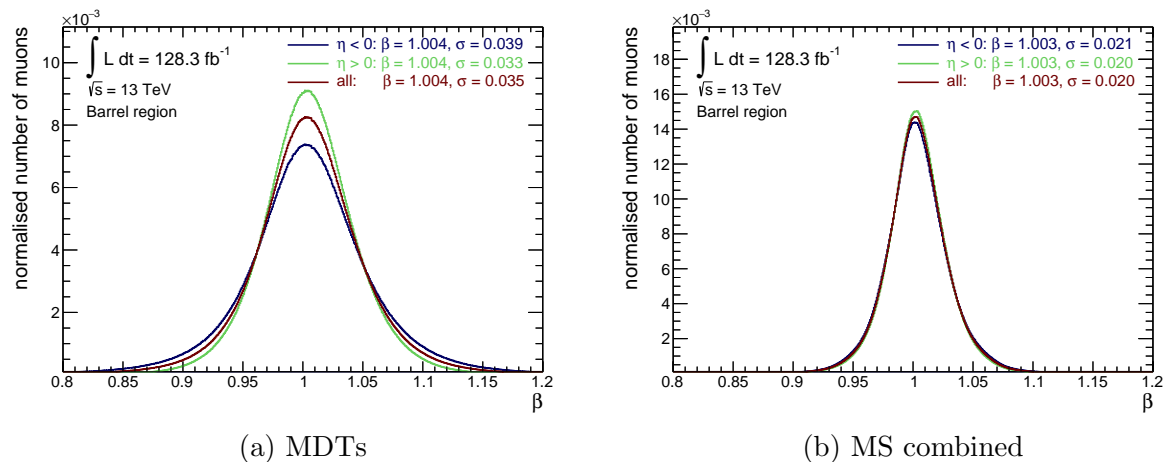
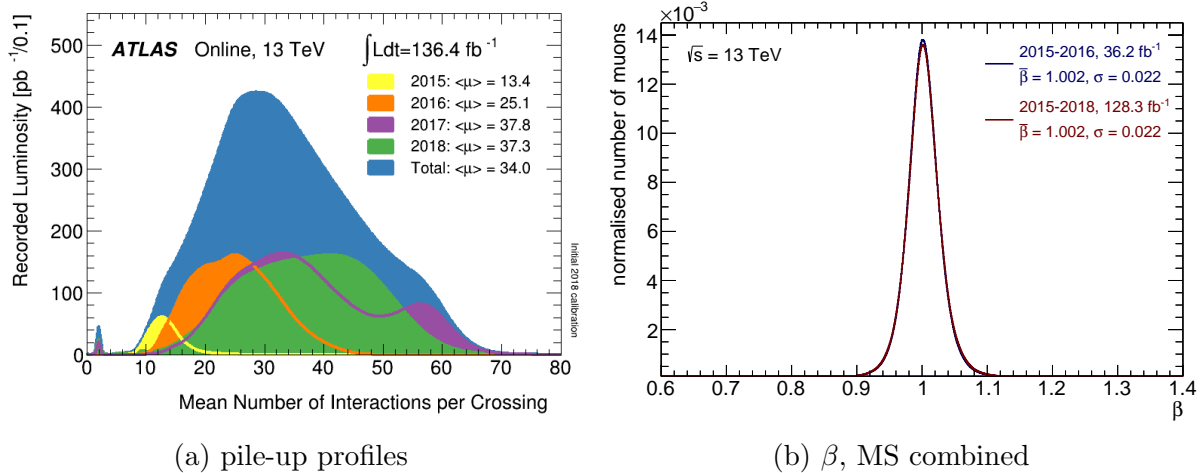


Figure 5.28: Comparison between β distributions after calibration as obtained in the barrel region in the ATLAS side C (blue) and side A (green) as well as in the whole barrel region (red). Drawn are the distributions for the MDT system (a) and the combination of the muon spectrometers systems, i.e., MDT and RPC system, (b). Given are also the mean and standard deviation of Gaussian fits using a reduced fitting window mean \pm RMS to the distributions.

does not yield any increase in the β resolution. This is positive, as it prevents later analyses making use of this calibration from having to account for a β resolution varying with time. As based on this result, no further insight can be expected from treating also the data-taking periods 2017 and 2018 separately, no additional comparisons between the years are conducted.



(a) pile-up profiles

(b) β , MS combined

Figure 5.29: (a) Luminosity recorded by ATLAS versus mean number of interactions per bunch crossing μ , separated by the year of data-taking and in total. Figure taken from [56]. (b) Comparison of the β distributions for the combined muon spectrometer after calibration as obtained from the data-taking period 2015–2016 (blue) and 2015–2018 (red). Given are also the mean and standard deviation of Gaussian fits using a reduced fitting window mean \pm RMS to the distributions.

Chapter 6

Simulation treatment

After the successful calibration of the ATLAS muon spectrometer with data, it is necessary to also derive calibration constants for simulated events as those are used by searches for charged SMPs with ATLAS to obtain exemplary exclusion limits on cross sections and particle masses for selected SUSY models. As the calibration process for MC events has to be analogous to that for data, the $Z \rightarrow \mu\mu$ MC events, generated as described in Section 5.1 and selected as described in Section 5.2, are used. Those are then treated in the exact same way as described for data in the previous chapter, starting with drift-time calibration and ending with pull correction.

While the thus obtained β distributions, shown in Figure 6.2, exhibit in general acceptable agreement between fully-calibrated data and simulation, for the t_0 distributions (Figure 6.1) this is not the case: The mean of the MDT t_0 distribution is slightly shifted in MC compared to data. For RPCs, it is even worse, as the t_0 distributions exhibit spiky structures and for RPC ϕ -strips, the standard deviation does not even closely match that in data. The spiky structure in this case is again caused by the RPC readout timing-granularity as described in Section 5.3. However, while in data it disappeared with the element-wise calibration step, this is obviously not the case in MC. The reason for this is presumably that, while during data-taking RPCs repeatedly receive timing corrections between runs, only one detector simulation setup is used for all MC events. Therefore, no small corrections exist that can wash out the peaks.

Therefore, it is worth to try to achieve better agreement between the distributions in data and MC by applying some additional treatment to MC events. The steps carried out for that shall be described in this chapter. The general approach is oriented by the procedure described in Reference [116].

6.1 Element-wise treatment

The additional treatment for MC events is ideally done on element level as this also allows to correct on low scale for various mismodellings of the detector in simulation. Usually, a method called *smearing* can be used for this purpose. Hereby, each timing measurement

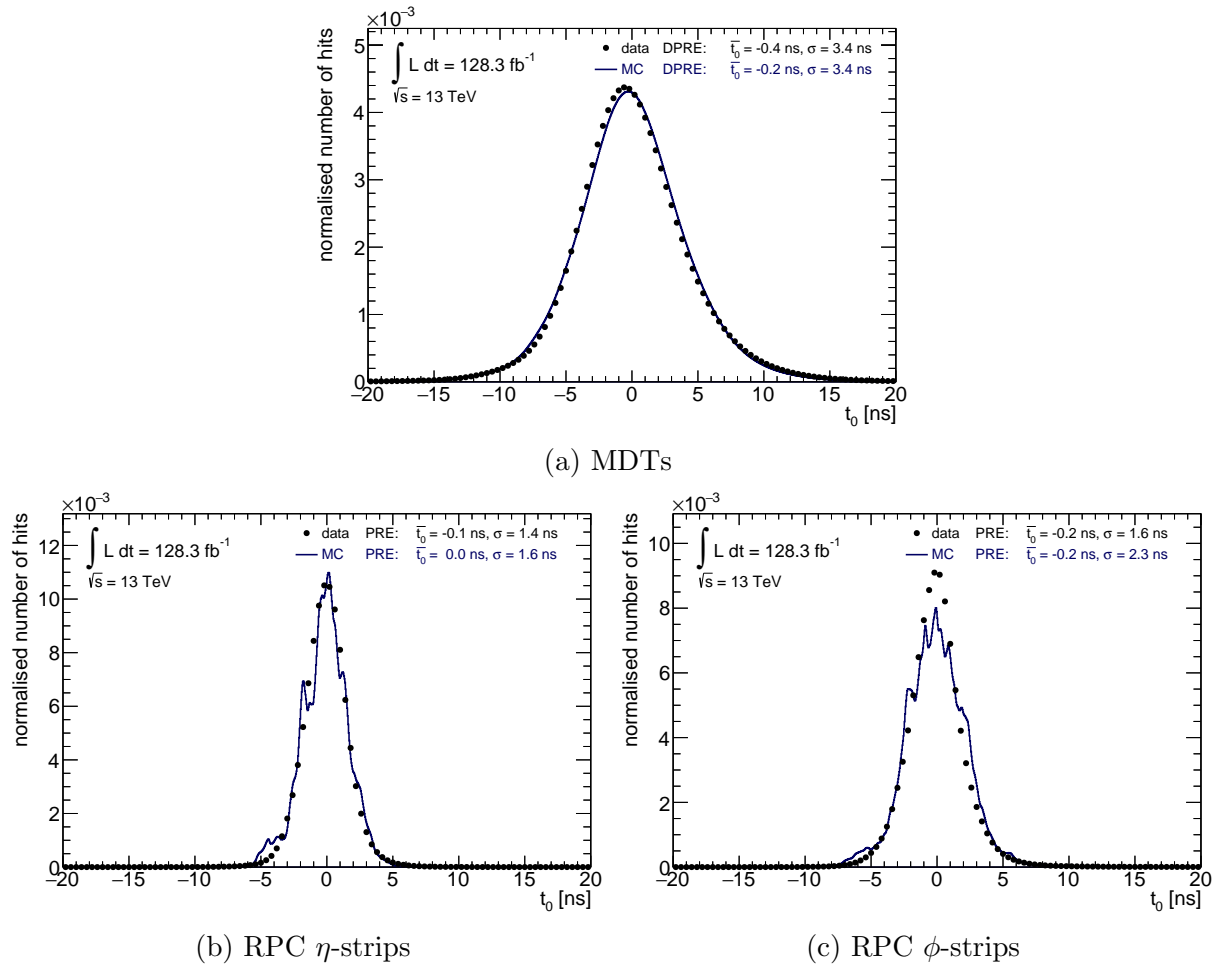


Figure 6.1: Comparison between t_0 distribution as obtained from fully calibrated data (black dots) and as obtained for data calibration steps applied to MC (blue line). Drawn are the distributions for MDTs (a), RPC η -strips (b) and RPC ϕ -strips (c). Given are also the mean and standard deviation of Gaussian fits using a reduced fitting window mean \pm RMS to the distributions.

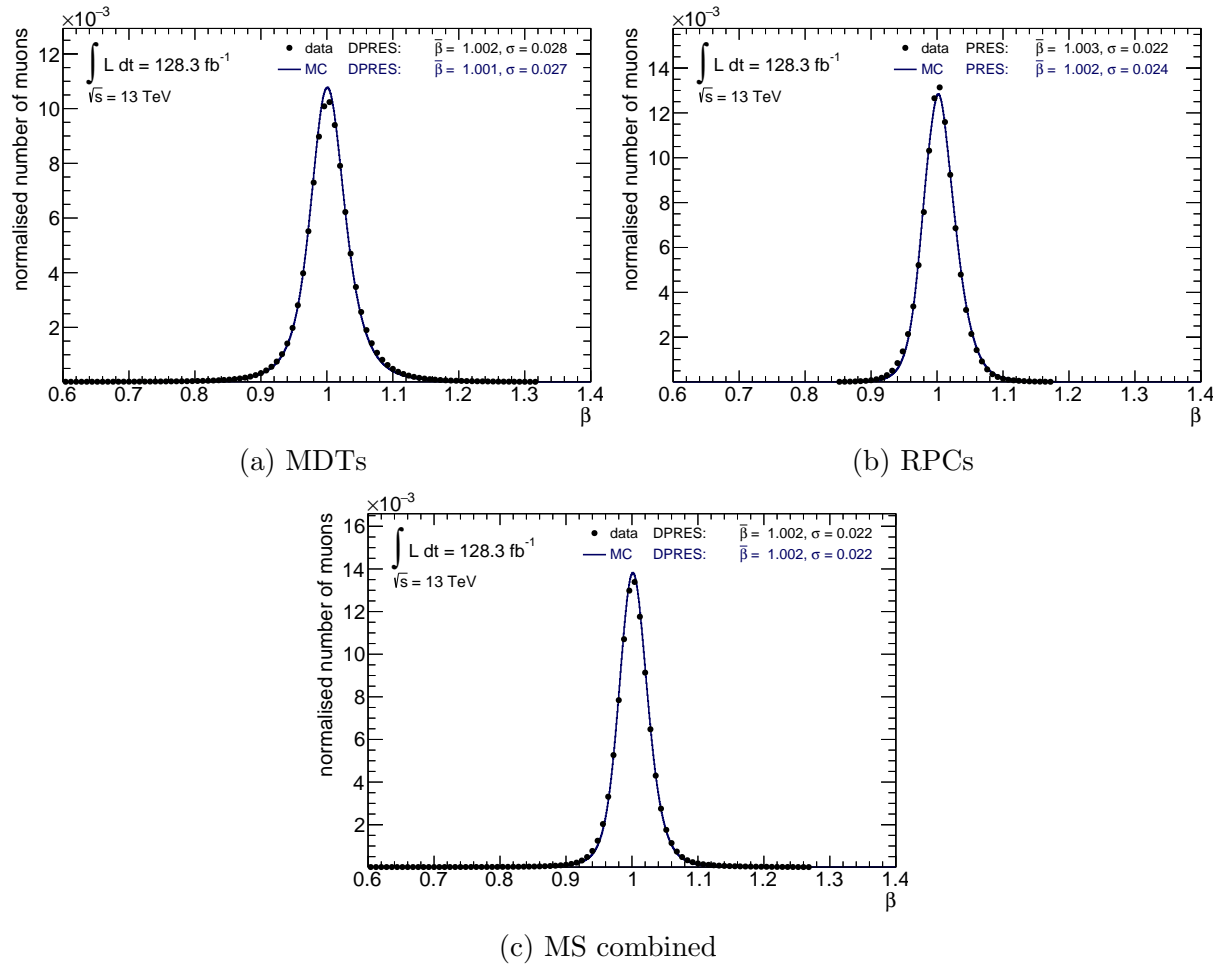


Figure 6.2: Comparison between β distribution as obtained from fully calibrated data (black dots) and as obtained for data calibration steps applied to MC (blue line). Drawn are the distributions for the MDT (a) and RPC (b) system as well as the combined MS (c). Given are also the mean and standard deviation of Gaussian fits using a reduced fitting window $\text{mean} \pm \text{RMS}$ to the distributions.

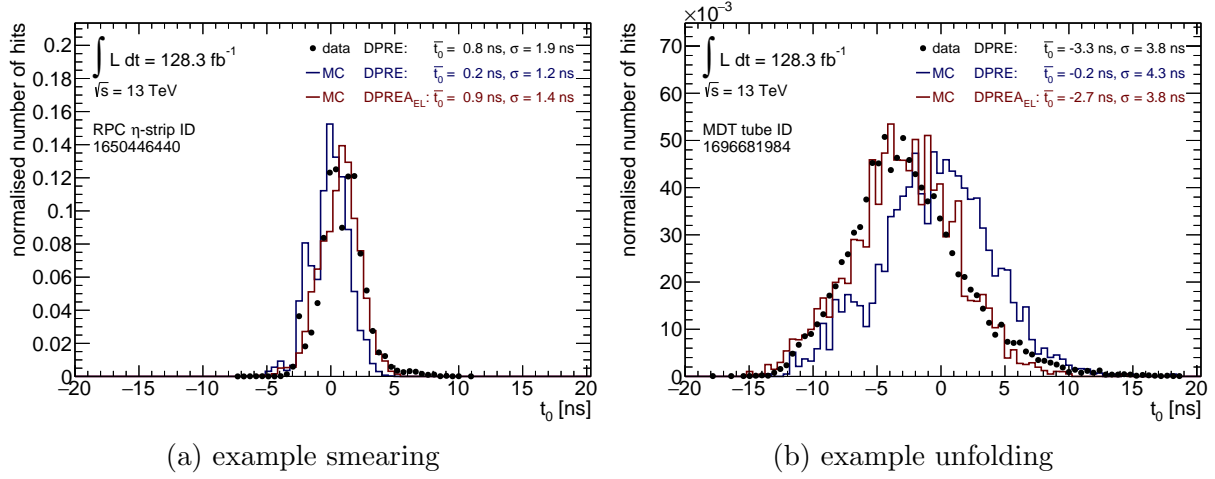


Figure 6.3: Comparison between t_0 distribution as obtained from fully calibrated data (black dots) as well as in MC before (blue line) and after (red line) element-wise adjustment, for randomly chosen elements. Drawn are the distributions for an RPC η -strip that receives a smearing procedure (a) and an MDT tube whose distribution is unfolded (b). Given are also the mean and standard deviation of Gaussian fits using a reduced fitting window mean \pm RMS to the distributions.

t_0^{in} is corrected by

$$t_{0,\text{MC}}^{\text{out}} = t_{0,\text{MC}}^{\text{in}} - (\bar{t}_{0,\text{MC}} - \bar{t}_{0,\text{data}}) + \text{Gauss} \left(0, \sqrt{\sigma_{\text{data}}^2 - \sigma_{\text{MC}}^2} \right),$$

where $\text{Gauss}(\mu, \sigma)$ corresponds to drawing a random number from a Gaussian distribution with mean μ and standard deviation σ . σ_{data} and σ_{MC} are the standard deviations of the t_0 distributions as observed in data and MC, respectively. This procedure ensures that $t_{0,\text{MC}}^{\text{out}}$ follows a Gaussian distribution with mean $\bar{t}_{0,\text{data}}$ and standard deviation σ_{data} , i.e., is similar to the distribution observed in data. Of course, this method can only be applied if $\sigma_{\text{data}}^2 > \sigma_{\text{MC}}^2$. Example t_0 distributions in data as well as in MC before and after smearing for a randomly chosen RPC η -strip are shown in Figure 6.3a.

It is not possible to apply a smearing procedure to each detector element, however, as for many detector elements the t_0 uncertainty in MC overestimates the t_0 uncertainty in data, i.e., $\sigma_{\text{data}}^2 < \sigma_{\text{MC}}^2$. This becomes especially evident when investigating the distribution of the difference between the t_0 uncertainty in MC and data for each detector element, as done in Figure 6.4. Here, a Gaussian distribution centred at zero is expected as of course some disagreements between the t_0 uncertainty in MC and data are expected but they should cancel out in the mean. However, a strong asymmetry of the difference $\sigma_{\text{data}} - \sigma_{\text{MC}}$ can be noted, showing that there are more than expected detector elements for which MC underestimates the high t_0 resolution achieved in data. This is especially the case for RPC ϕ -strips, but also the distribution for RPC η -strips is problematic as it exhibits a shift

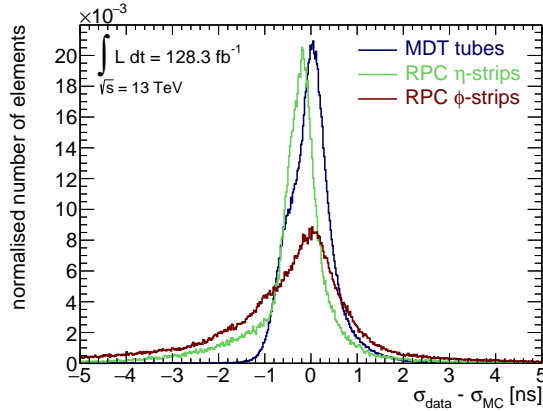


Figure 6.4: Distribution of the difference between the t_0 uncertainty as obtained in data, σ_{data} , and in MC, σ_{MC} , for each detector element after the full calibration but without adjustment for MC. Drawn are the distributions for the MDT tubes (blue), RPC η -strips (green) and RPC ϕ -strips (red).

towards negative values.

Thus, for each detector element of the three systems overestimating in MC the t_0 uncertainty achieved in data, a technique with the purpose to get those uncertainties to match is applied. As the smearing procedure works only for elements with $\sigma_{\text{data}} > \sigma_{\text{MC}}$, a different technique has to be used. The one chosen for this work is called *unfolding* and was originally developed to remove the effects of a detector from an observed distribution and thereby reveal the true nature of the distribution. The idea behind this is that the measured distribution can be considered as the true distribution folded with the detector response. For the unfolding procedure, at first the *response matrix* of a detector element is calculated by mapping the t_0 distribution obtained in MC to the t_0 distribution obtained in data. One entry in the matrix, R_{ij} , then gives the fraction of candidates with a certain value $t_{0,j}$ of the data distribution that were simulated as $t_{0,i}$ of the MC distribution. To allow for a computable response value, the distributions are idealised to be Gaussian shaped and are therefore replaced by Gaussian distributions with matching mean and standard deviation. An example response matrix can be seen in Figure 6.5a for a randomly chosen MDT tube.

This response matrix is then processed with the RooUnfold v. 1.1.1 [117] software framework for ROOT [118], giving an unfolding matrix like that in Figure 6.5b as output. This matrix can be used to generate an unfolded value $t_{0,\text{MC}}^{\text{out}}$ by drawing a random number from the y -projection of the bin corresponding to a given $t_{0,\text{MC}}^{\text{in}}$. As it is not possible to store an unfolding matrix for each of the more than 735,000 detector elements, the unfolding matrix is parametrised by fitting a linear function $f(t_{0,\text{MC}}^{\text{in}}) = m \cdot t_{0,\text{MC}}^{\text{in}} + n$ to it and measuring the standard deviation σ_{unf} of the Gaussian distribution for each $t_{0,\text{MC}}^{\text{in}}$ -bin. $t_{0,\text{MC}}^{\text{out}}$ can then be calculated according to

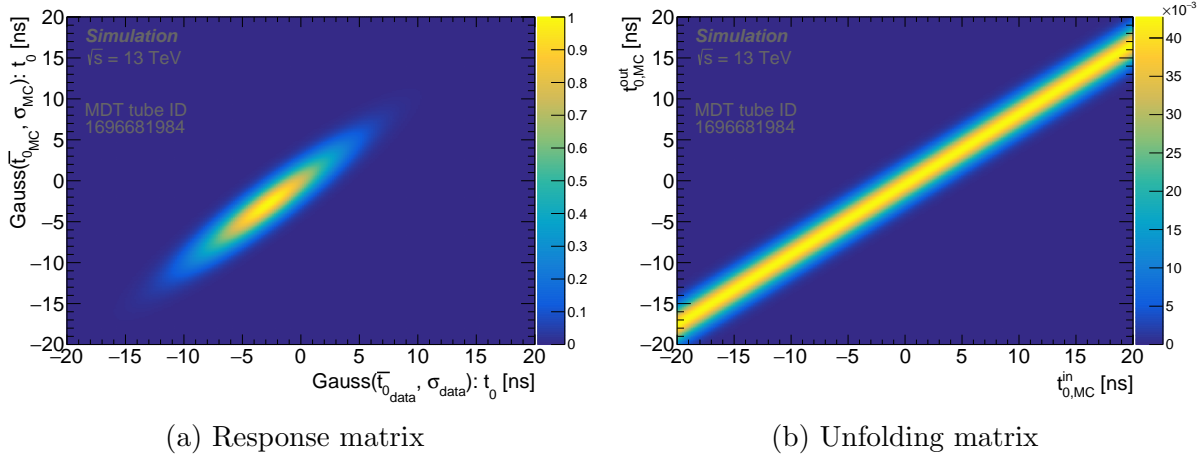


Figure 6.5: (a) Response matrix for a randomly chosen MDT tube. The projection on the x -axis follows a Gaussian distribution with mean $\bar{t}_{0,\text{data}}$ and standard deviation σ_{data} , the projection on the y -axis a Gaussian distribution with mean $\bar{t}_{0,\text{MC}}$ and standard deviation σ_{MC} . (b) The corresponding unfolding matrix for the same MDT tube. An unfolded value $t_{0,\text{MC}}^{\text{out}}$ can be obtained by drawing a random number from the y -projection of the bin corresponding to a given $t_{0,\text{MC}}^{\text{in}}$. To allow for a better recognition of the features, the matrices have been limited to the range $[-20 \text{ ns}; 20 \text{ ns}]$ in both figures.

$$t_{0,\text{MC}}^{\text{out}} = \text{Gauss} \left(m \cdot t_{0,\text{MC}}^{\text{in}} - (\bar{t}_{0,\text{MC}} - \bar{t}_{0,\text{data}}) + n, \sigma_{\text{unf}} \right).$$

This gives in general good agreement between the t_0 distribution in data and the t_0 distribution in MC, as can be seen exemplary in Figure 6.3b for the same MDT tube as in Figure 6.5.

Applying this element-wise adjustment (symbol A_{EL}), i.e., a smearing or unfolding, to each detector element as needed results in the t_0 distributions for the whole systems shown in Figure 6.6. A better agreement between data and MC can be observed than before the MC treatment for MDTs. However, while the spiky structure for RPCs is finally washed out by this step, the difference in the standard deviations between MC and data increased drastically, unfortunately. The reason for this can be found in the low statistics for MC: The difference between σ_{MC} and σ_{data} depends largely on the number of registered hits, as is shown in Figure 6.7. For about 50,000 hits per element a good agreement between the t_0 uncertainty in data and MC can be expected. However, this is a lot more than the available average hits per element: Weights for only about 8,000 hits per MDT tube, 2,100 hits per RPC η -strip and 1,000 hits per RPC ϕ -strip are registered on average per detector element. Thus, no good agreement between the t_0 distributions in data and MC is achieved for many elements. This of course also results in less agreement when looking at the β distributions, which can be found in Figure 6.8. In consequence, a slightly different

approach is needed to achieve agreement between data and simulated events.

6.2 Chamber-wise treatment

As the adjustment by smearing and unfolding described in the previous section would work in principle if enough statistic was available, instead of adjusting element-wise a chamber-wise procedure (symbol A_{CH}) is carried out. This makes use of the exact same techniques for smearing and unfolding described in the previous section but applies them on the about 1,200 MDT and 600 RPC chambers. Hereby, RPC η - and ϕ -strips are still treated separately. However, the larger statistics comes at the expense of the granularity. This is disadvantageous as, using an element-wise adjustment, mismodellings of the detector in simulation could be reduced on a very low scale. On chamber level, less error correction can be achieved.

The resulting t_0 distributions, which are shown in Figure 6.9, again match well for MDTs. In addition, for RPC η -strips the achieved agreement between data and MC is not perfect but significantly increased. However, there is still a large discrepancy between the t_0 distributions for RPC ϕ -strips in MC and data. The reason for this is presumably the worse granularity of the chamber-wise approach, not being able to correct for low-level mismodellings of the detector. Therefore, a more detailed treatment of RPC ϕ -strips in MC would be necessary, which shall not be covered in this thesis, however.

In Figure 6.10, the corresponding β distributions can be found. While the element-wise adjustment lead to a slight underestimation of the β resolution for MDTs in MC, the chamber-wise adjustment now overestimates it a little. For RPCs, the discrepancies seen in the timing measurements for RPC ϕ -strips are compensated by the RPC η -strips, resulting in a good agreement between MC and data, overall. Both of this causes a β distribution for the combined MS in MC that matches that in data altogether well. Therefore, the chamber-wise adjustment as outlined in this section is chosen as the method for MC treatment.

It was considered to retain the element-wise adjustment instead of the chamber-wise treatment for MDTs as they show an equally good agreement between data and MC in both adjustment strategies. In consequence, a χ^2 test was conducted, comparing the data distributions in t_0 and β to the corresponding distributions obtained from element-wise and chamber-wise adjustment. As the χ^2/ndof for the chamber-based approach is lower for the t_0 as well as for the β distribution, the chamber-wise adjustment is also adopted for MDTs.

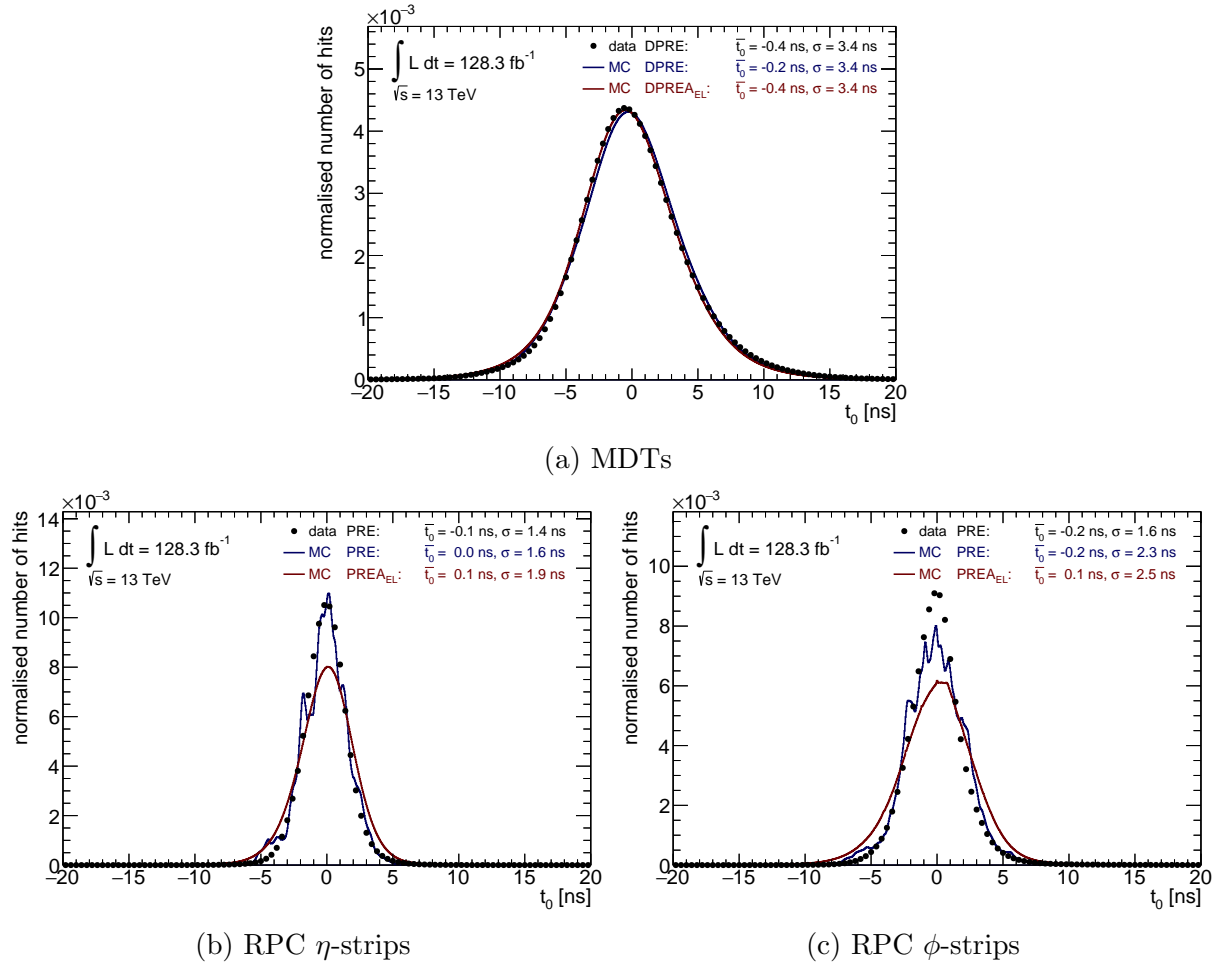


Figure 6.6: Comparison between t_0 distributions as obtained from fully calibrated data (black dots) as well as obtained for MC without (blue line) and with (red line) element-wise adjustment. Drawn are the distributions for MDTs (a), RPC η -strips (b) and RPC ϕ -strips (c). Given are also the mean and standard deviation of Gaussian fits using a reduced fitting window mean \pm RMS to the distributions.

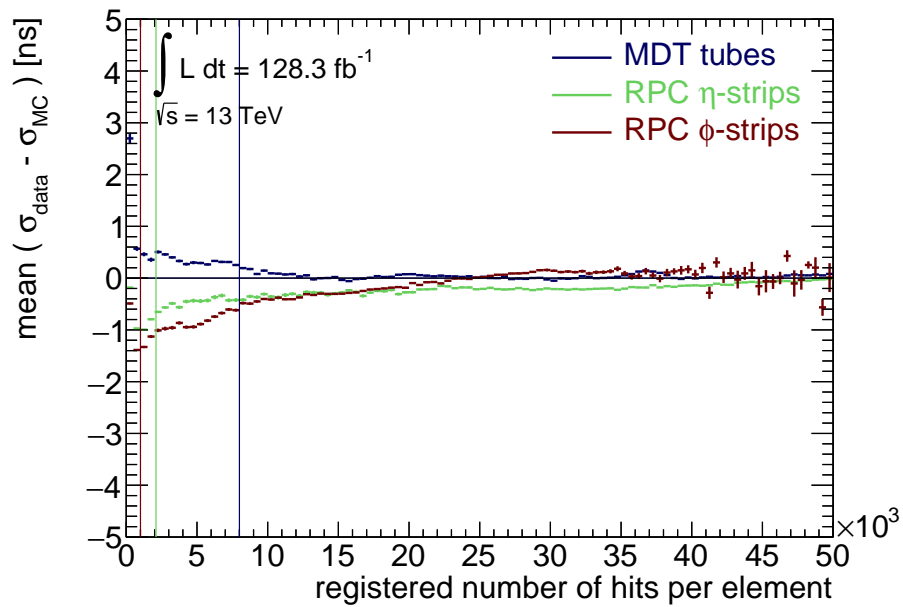
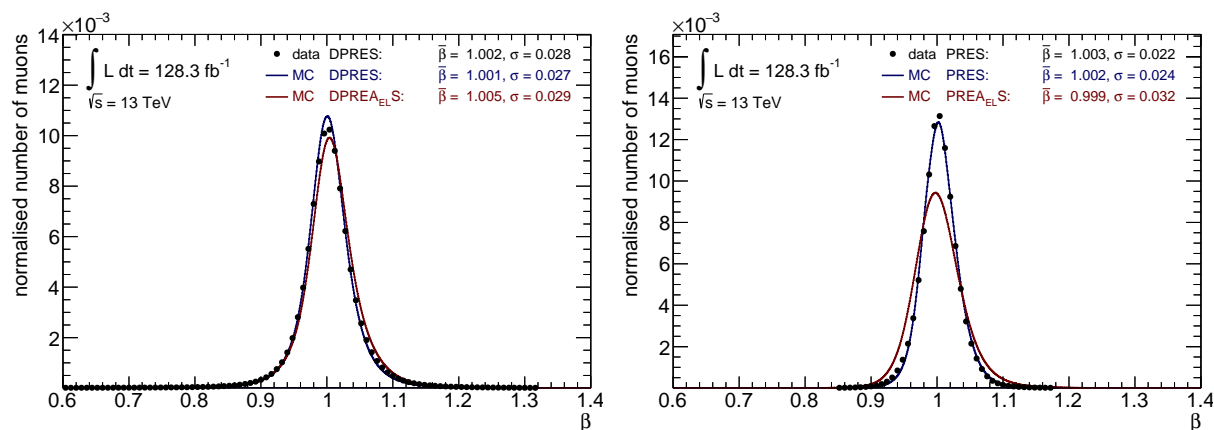
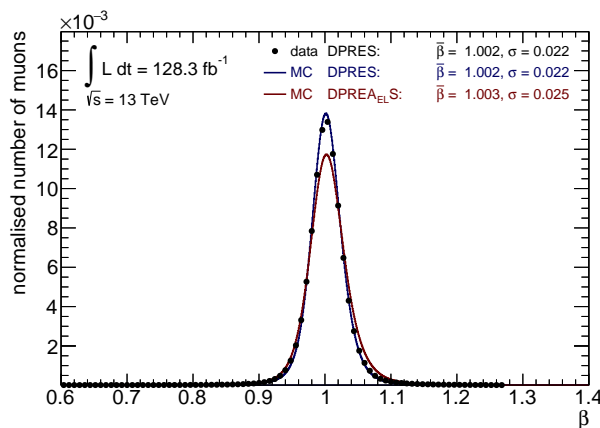


Figure 6.7: Mean of $\sigma_{\text{data}} - \sigma_{\text{MC}}$ for all detector elements with a certain number of registered hits versus the number of registered hits. σ_{data} is taken after the full calibration chain, σ_{MC} after the full calibration chain as well as element-wise adjustment. Drawn are the distributions for MDTs (blue), RPC η -strips (green) and RPC ϕ -strips (red). The average number of hits per element of a detector system is marked by a vertical line in the corresponding color.



(a) MDTs

(b) RPCs



(c) MS combined

Figure 6.8: Comparison between β distributions as obtained from fully calibrated data (black dots) as well as obtained for MC without (blue line) and with (red line) element-wise adjustment. Drawn are the distributions for MDTs (a), RPCs (b) and the combination of both systems (c). Given are also the mean and standard deviation of Gaussian fits using a reduced fitting window mean \pm RMS to the distributions.

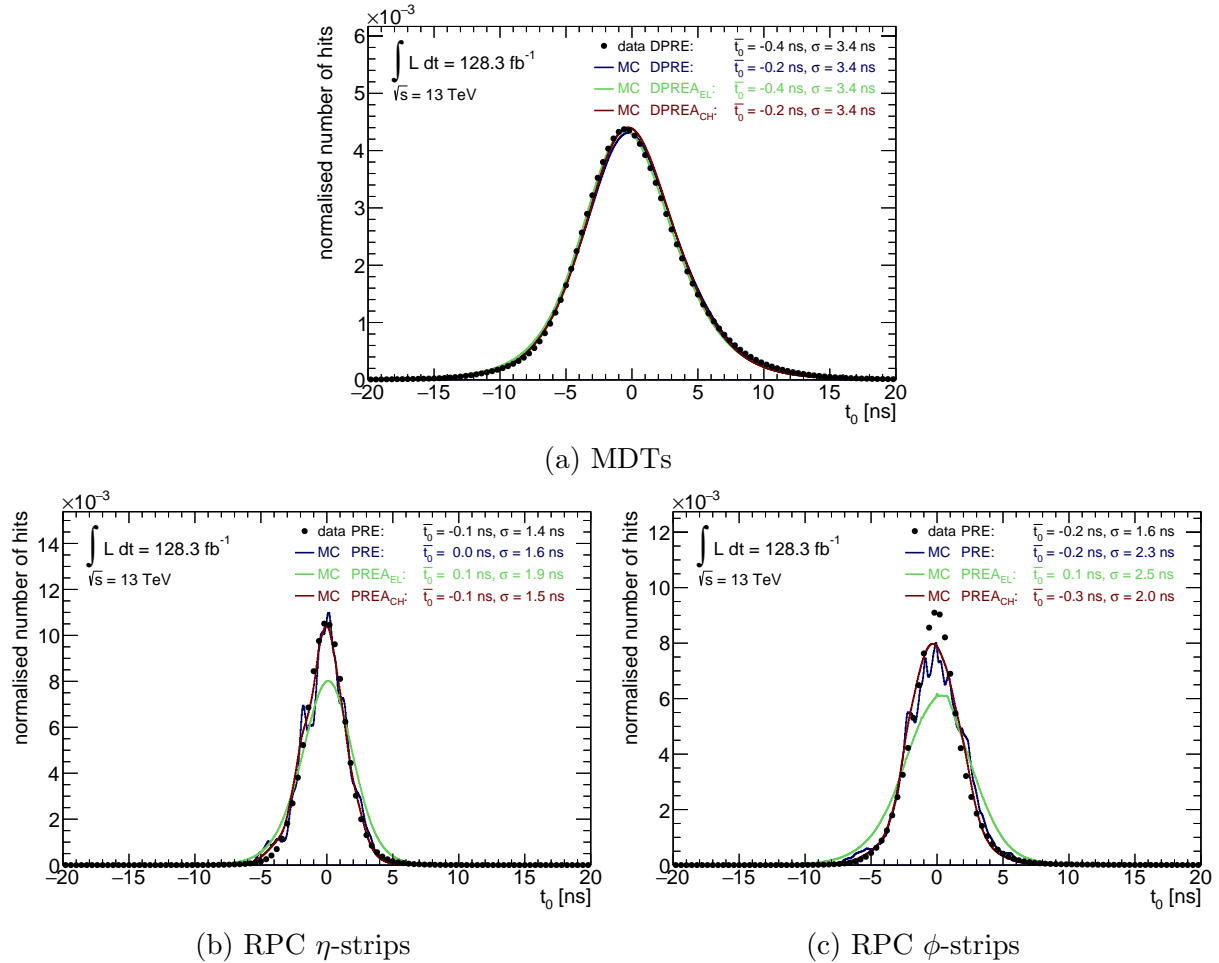


Figure 6.9: Comparison between t_0 distributions as obtained from fully calibrated data (black dots) and from MC without adjustment (blue line) as well as from element-wise (green line) and chamber-wise (red line) adjusted MC. Drawn are the distributions for MDTs (a), RPC η -strips (b) and RPC ϕ -strips (c). Given are also the mean and standard deviation of Gaussian fits using a reduced fitting window mean \pm RMS to the distributions.

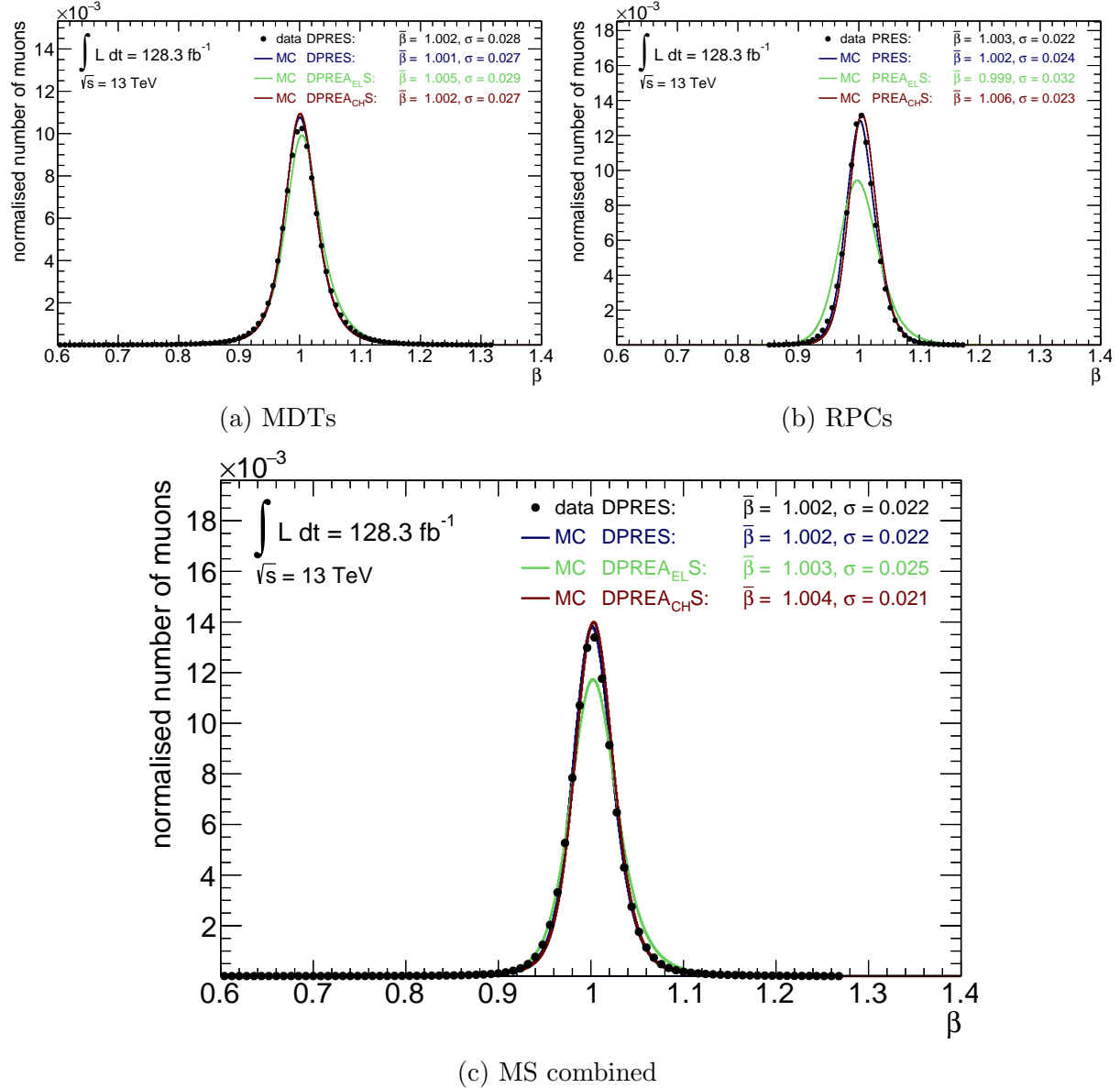


Figure 6.10: Comparison between β distributions as obtained from fully calibrated data (black dots) and from MC without adjustment (blue line) as well as from element-wise (green line) and chamber-wise (red line) adjusted MC. Drawn are the distributions for MDTs (a), RPCs (b) and the combination of both systems (c). Given are also the mean and standard deviation of Gaussian fits using a reduced fitting window mean \pm RMS to the distributions.

6.3 Signal treatment

The calibration and adjustment constants as derived for simulated $Z \rightarrow \mu\mu$ events can then be applied to simulated signal events to allow setting exclusion limits on upper production cross sections and on particle masses in a future search for charged SMPs. Here, the stable-chargino and stable-stau events, generated as described in Section 5.1 are used as signal events. As those have $\beta < 1$ and t_0 is accordingly expected to be larger than zero, the last adjustment step can of course not be applied directly to t_0 . Therefore, in this step t_0 is replaced by the difference between measured and truth ToF,

$$\Delta\text{ToF} := \text{ToF}_{\text{measured}} - \text{ToF}_{\text{truth}}.$$

For data and simulated $Z \rightarrow \mu\mu$ events, due to the definition of t_0 in equation (4.3), ΔToF is essentially the same as t_0 . For simulated signal events, ΔToF is different from signal t_0 but gives rise to distributions similar to that of t_0 for muons, as shown in Figure 6.11. There, ΔToF distributions are compared for calibrated data, $Z \rightarrow \mu\mu$ MC and signal MC. Naturally, the overall agreement between $Z \rightarrow \mu\mu$ MC and data is better than between signal MC and data as the calibration was carried out based on muons.

The corresponding β distributions before and after calibration and chamber-wise adjustment for signal MC are compared to the truth β distributions in Figure 6.12. For MDTs, discrepancies between truth and uncalibrated reconstructed β distribution can be noted. After calibration and adjustment, those discrepancies are significantly reduced. For RPCs, the allowed range for truth particles has been limited to $|\eta| < 1.05$ as the β distribution of the signal depends on η but there are not RPCs in the end-caps, i.e., at about $|\eta| > 1.05$. The agreement between the distribution in reconstruction before any treatment and truth is very good, already. In consequence, no visible improvement is achieved by calibration and adjustment for RPCs. When combining MDTs and RPCs, however, now again considering the full η -range, the β estimate in reconstruction is significantly improved by the calibration and adjustment.

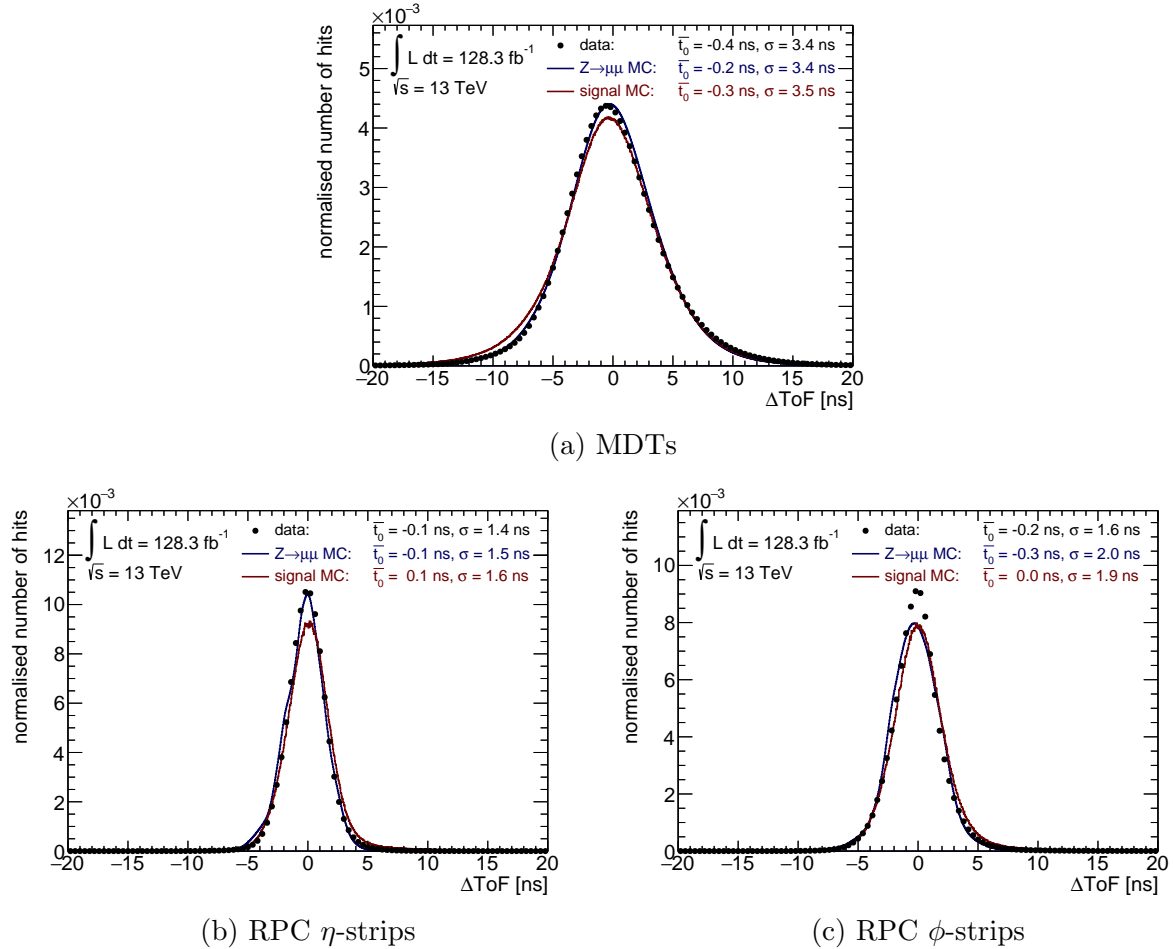


Figure 6.11: Comparison between ΔToF distributions as obtained from fully calibrated data (black dots) as well as fully calibrated and adjusted $Z \rightarrow \mu\mu$ (blue line) and signal (red line) MC events. Drawn are the distributions for MDTs (a), RPC η -strips (b) and RPC ϕ -strips (c). Given are also the mean and standard deviation of Gaussian fits using a reduced fitting window mean \pm RMS to the distributions.

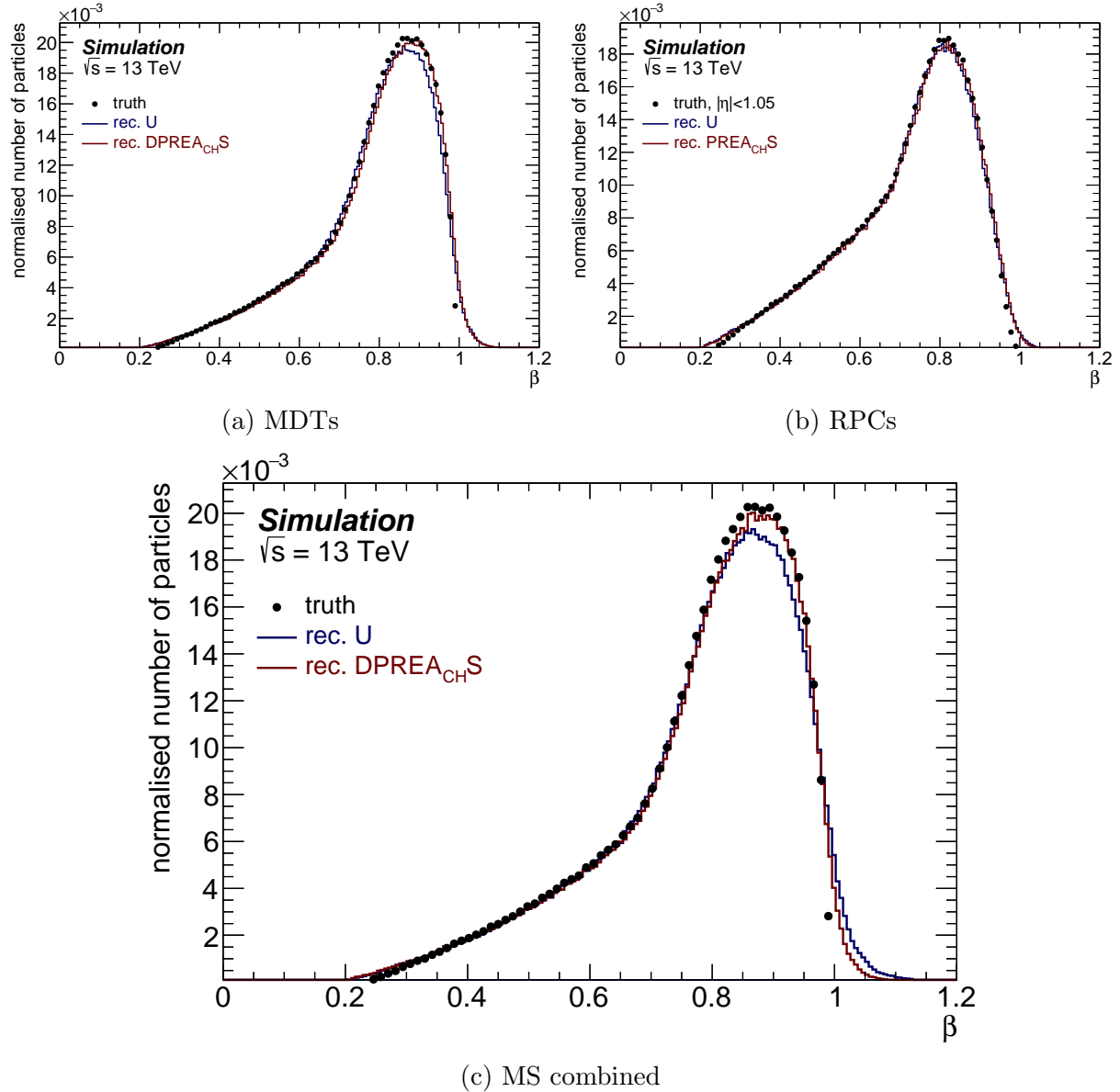


Figure 6.12: Comparison between β distribution for MC-generated stable charginos and stable staus on truth level (black dots) and as obtained from reconstructed particles before (blue line) and after calibration and adjustment (red line). Drawn are the distributions for MDTs (a), RPCs (b) and the combination of both systems (c). For RPCs, the truth distribution has been limited to the range $|\eta| < 1.05$ as the β distribution of the signal is η -dependent and there are no RPCs in the end-caps, i.e., at about $|\eta| > 1.05$.

Chapter 7

Conclusion and Outlook

In this thesis, a timing calibration procedure of the MDT and RPC system in the ATLAS muon spectrometer was presented. In the future, this calibration can be used for searches for charged stable massive particles with the ATLAS detector. Although there had been a previous timing calibration of the ATLAS muon spectrometer, based on the dataset taken in 2015 to 2016, a renewed approach was necessary as the reconstruction algorithm for charged stable massive particles of ATLAS had received a major revision over the last years. This revision of the algorithm resulted in a much higher reconstruction efficiency for charged stable massive particles, especially in the crack regions of ATLAS at $1.0 < |\eta| < 1.7$ and $\eta \approx 0$, as could be shown in this thesis. Unfortunately, it also rendered the old calibration constants outdated.

For this renewed approach on the calibration, proven techniques of the previous calibration were adopted and extended by further calibration steps. These make use of the dataset that is enlarged due to the higher reconstruction efficiency on the one hand and due to the progressed data-taking in the years 2017–2018 on the other hand. The calibration procedure now starts with a drift-time calibration, taking account of an imperfect modelling of the non-linear space–drift-time-relation for the drift gas used in MDTs. This step is followed by a propagation-time calibration that corrects propagation times of signals in the detector electronics that were slightly incorrectly calculated during reconstruction. Afterwards, calibration steps similar to those in the previous calibration — a correction for each run as well as a correction for each MDT tube and RPC strip — are applied. Finally, the uncertainties of the β measurements are adjusted by a pull correction. With all of this, a β resolution as high as $\sigma = 0.022$ can be achieved. This is a result similar to that in the previous calibration, despite some MDT hits being not correctly processed in the barrel region of the ATLAS side C.

As searches for charged stable massive particles with the ATLAS detector rely on Monte Carlo simulated events, a treatment for this kind of events based on the above calibration steps is presented as well. Since the β resolution in Monte Carlo events tends to differ from the β resolution achieved in data, an elaborate procedure is needed to get those resolutions to match. As the statistics on individual MDT tubes and RPC strips are too low to allow a simulation treatment on that level, a chamber-wise approach is conducted. In this,

chambers overestimating the β resolution obtained in data receive a smearing procedure. For those underestimating the β resolution, an unfolding takes place. With this, good agreement between data and Monte Carlo is achieved.

Before the timing calibration of the ATLAS muon spectrometer presented in this thesis can be used for searches for charged stable massive particles, it is necessary to also revise the timing calibration of the tile calorimeter that is used in those searches as well. While the general procedure of the calibration can most certainly be adopted from a previous calibration, presumably also different calibration steps might be necessary to account for changes in the reconstruction algorithm. Then again, some calibration procedures might finally be possible due to the enlarged dataset now available.

Another pressing question that has to be answered before a renewed search for charged stable massive particles can be conducted is what the exact origin of the missing hits in MDTs in the barrel region of the ATLAS side C is. This is of course closely connected with answering how to solve this problem and whether a complete reprocessing of the data is needed afterwards. If this was the case, the timing calibration of the muon spectrometer as presented in this work would probably have to be conducted again. Nevertheless, as the described procedure stays valid, this could be done with little effort.

Finally, if all of this is accomplished, there are no further obstacles preventing a search for charged stable massive particles with the full Run-2 dataset taken in the years 2015–2018. With this, it will at least be possible to decrease the current upper cross-section exclusion limits set on those particles. Due to the model-independent approach of the search, it can be expected the achieved results will stay relevant for a long time, even if no excesses are observed and the specific models used for setting exclusion limits might be outdated. Nevertheless, the main hope is and stays, of course, to observe charged stable massive particles, at last.

Appendix A

Missing MDT hits in the barrel region of the ATLAS side C

In the course of this work, it was discovered that particles reconstructed with MUGIRLOWBETA have less registered MDT hits if they are detected in side C ($\eta < 0$) of ATLAS than in side A ($\eta > 0$). This can in particular be seen in Figure A.1. In the following, the investigations that were carried out on this shall be documented for future use. Unless stated otherwise, the samples used are collision data taken in the years 2015–2018, reconstructed with MUGIRLOWBETA in R21 and processed with the SUSY8 derivation. For more detailed information on the used events and event selection see Sections 5.1 and 5.2.

The first step after observing the missing MDT hits in the barrel region is to check whether only MDT hits are affected or whether RPCs are involved as well. This does not seem to be the case, as no difference is visible between $\eta < 0$ and $\eta > 0$ for RPCs in Figure A.2a. It can be noted at this point that, curiously enough, neither all hits are missing for MDTs in side C of the barrel region nor even a constant amount of hits. Instead, the number of missing hits varies broadly with η .

Despite RPC hits being not affected by this, it is nevertheless possible that less candidates are reconstructed in side C of ATLAS as a result of the missing hits. Indeed, as shown in Figure A.2b, small deviations are seen between the $\eta < 0$ and $\eta > 0$ regions. However, they are small and at some spots there are even more candidates reconstructed on side C than side A. Thus, no clear conclusion can be drawn from this case.

Secondly, it has to be checked whether the missing hits are dependent on the data format. Although there are significant deviations between the graphs for data and MC visible, the overall structure that less hits are registered for $\eta < 0$ stays the same. This can be seen in Figure A.3a. Apart from this, it is imaginable that the hits are lost when deriving the SUSY8 data from the analysis-object data (xAOD) for disk space reduction. Figure A.3b gives evidence that this is not the case as well. Note in this figure that xAOD files are not supposed to be used for analysis and the data sample taken into account is therefore small. No asymmetry between the number of registered hits for $\eta < 0$ and $\eta > 0$ can be observed

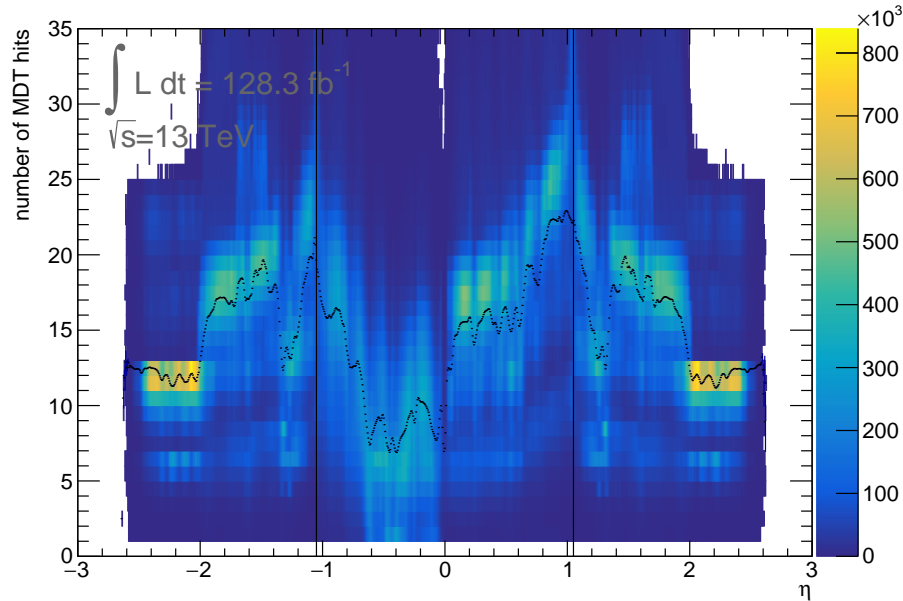
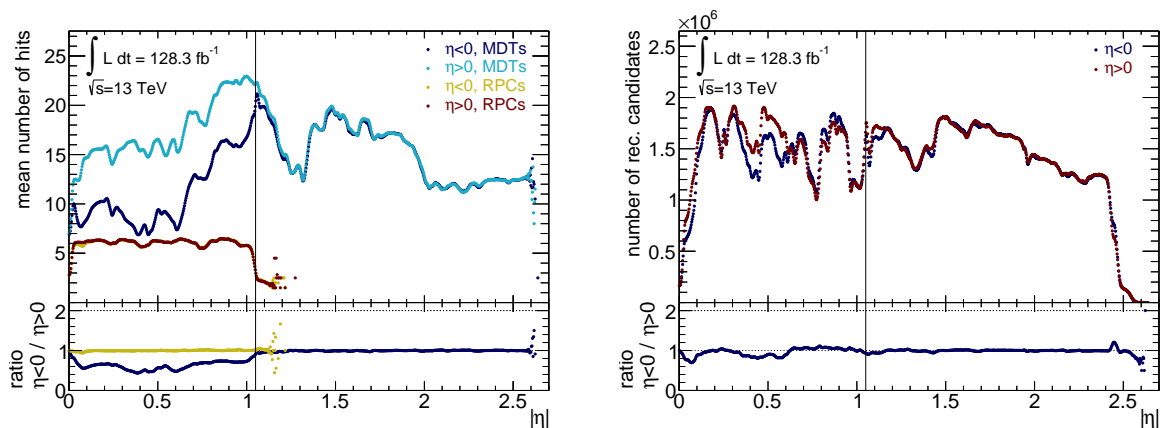


Figure A.1: Mean number of MDT hits per muon registered by MUGIRLLowBETA versus η of the reconstructed muons. The mean number of hits per η -bin is drawn in black. Vertical black lines mark the approximate border at $\eta \approx 1.05$ of the ATLAS barrel region.

in R20.7 (Figure A.3c). All of this leads to the conclusion that the origin of the missing hits has to be found within the reconstruction algorithm used in R21.

The next question, of course, is whether it is a bug of MUGIRLLowBETA or of the muon reconstruction algorithms in general. Clearly, no asymmetry can be observed for the nominal muon reconstruction algorithms, as shown in Figure A.4a. MUGIRL [89] is a muon reconstruction algorithm, which is in many ways similar to MUGIRLLowBETA. However, even when requiring MUGIRL as author of a reconstructed particle, as is done in Figure A.4b, no difference between $\eta < 0$ and $\eta > 0$ is found. Thus, the bug has its origin certainly within the code of MUGIRLLowBETA.

The last step that can be carried out to investigate this matter is to analyse the track fit parameters. There is neither a difference in the fit quality (χ^2 , Figure A.5a) nor in the number of degrees of freedom (ndof, Figure A.5b), which basically is a representation of the number of hits used for track fitting. In consequence, there is of course also no difference in χ^2/ndof , as shown in Figure A.5c. Even when subtracting the number of degrees of freedom in the ID from the total number of degrees of freedom, which reduces the number of hits used for track fitting not located in the muon spectrometer, no difference is visible (compare Figure A.5d). Unfortunately, no direct number of degrees of freedom is accessible for the muon spectrometer. Anyway, it is questionable that this would yield any new insight



(a) mean number of hits, MDTs versus RPCs

(b) number of reconstructed candidates

Figure A.2: (a) Mean number of registered hits versus $|\eta|$ for MDTs (light and dark blue) and RPCs (yellow and red), separated into $\eta < 0$ and $\eta > 0$. (b) Number of reconstructed candidates, separated into $\eta < 0$ (blue) and $\eta > 0$ (red). The vertical black line marks the approximate border of the ATLAS barrel region. Given are also the ratios for corresponding $\eta < 0$ and $\eta > 0$ graphs in both figures.

compared to the results show in Figure A.5. These outcomes are surprising as they suggest that the missing hits are actually not missing during track reconstruction. Therefore, it is probable that those hits are registered during reconstruction but erroneously discarded later on.

All in all, it can be concluded that the hits are missing only for MDTs in the ATLAS side C and they do so already on a rather basic level (pre-xAOD). The lower number of hits on side C can also be observed in simulation. It is a bug that was newly introduced in R21 but fortunately only affects MUGIRLOWBETA. Apart from that, it seems to have influence neither on the number of reconstructed candidates nor on the quality of the track fit. It stays an intriguing future task to discover the origin of this bug and fix it.

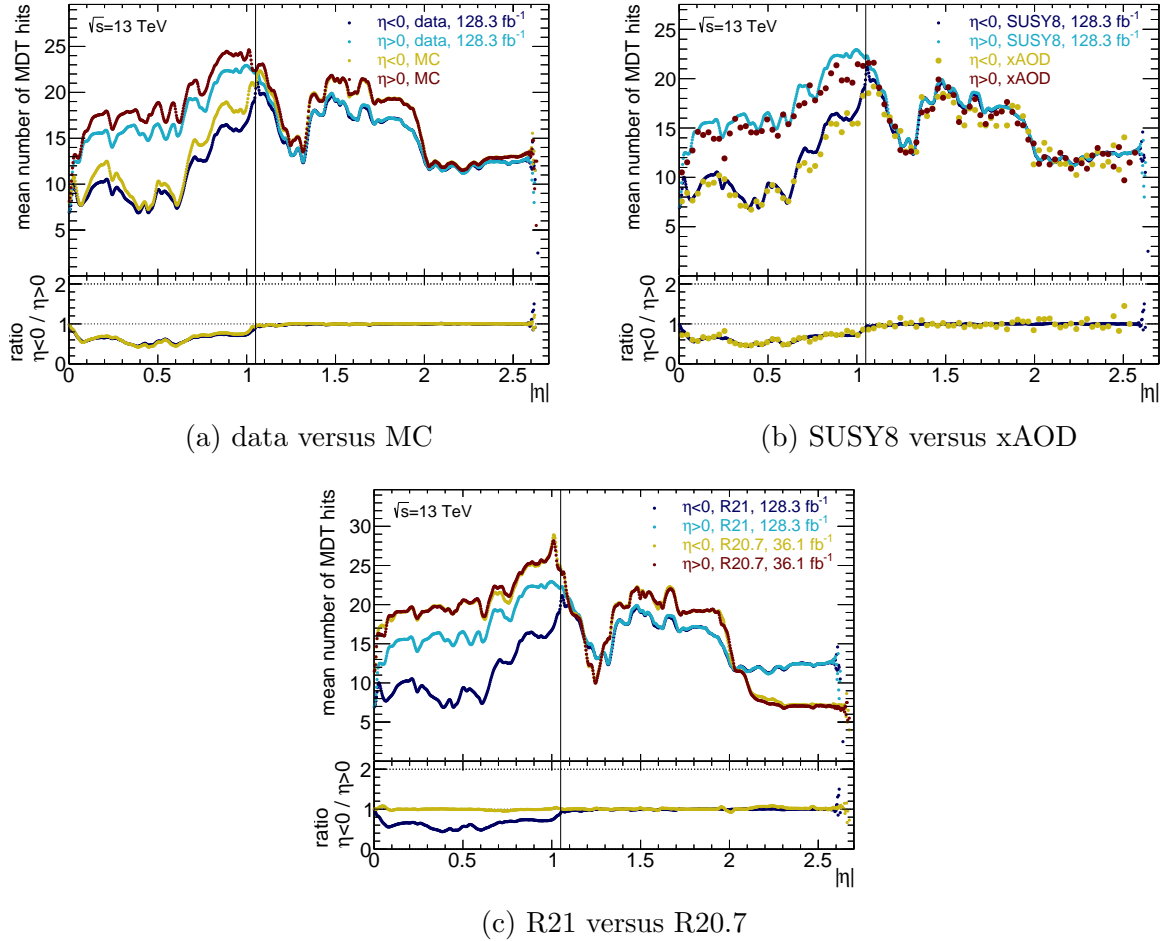
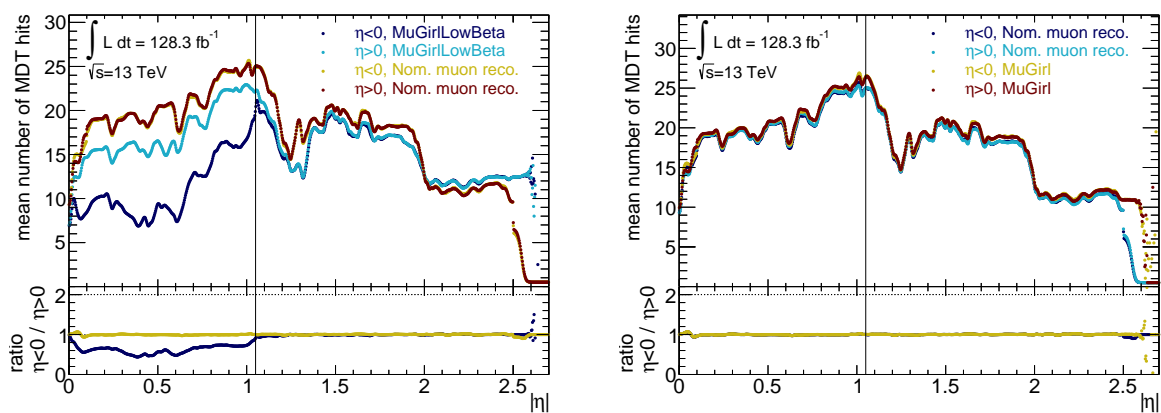


Figure A.3: Mean number of registered MDT hits versus $|\eta|$ for data compared to simulation (a), SUSY8 compared to xAOD (b) and R21 compared to R20.7 (c), separated into $\eta < 0$ and $\eta > 0$. The vertical black line marks the approximate border of the ATLAS barrel region. Given are also the ratios for corresponding $\eta < 0$ and $\eta > 0$ graphs in all figures.



(a) MUGIRLOWBETA versus nom. muon reco.

(b) Nom. muon reco. versus MUGIRL

Figure A.4: Mean number of registered MDT hits versus $|\eta|$ for reconstruction by MUGIRLOWBETA compared to nominal muon reconstruction algorithms (a) and nominal muon reconstruction algorithms compared to MUGIRL (c), separated into $\eta < 0$ and $\eta > 0$. The vertical black line marks the approximate border of the ATLAS barrel region. Given are also the ratios for corresponding $\eta < 0$ and $\eta > 0$ graphs in both figures.

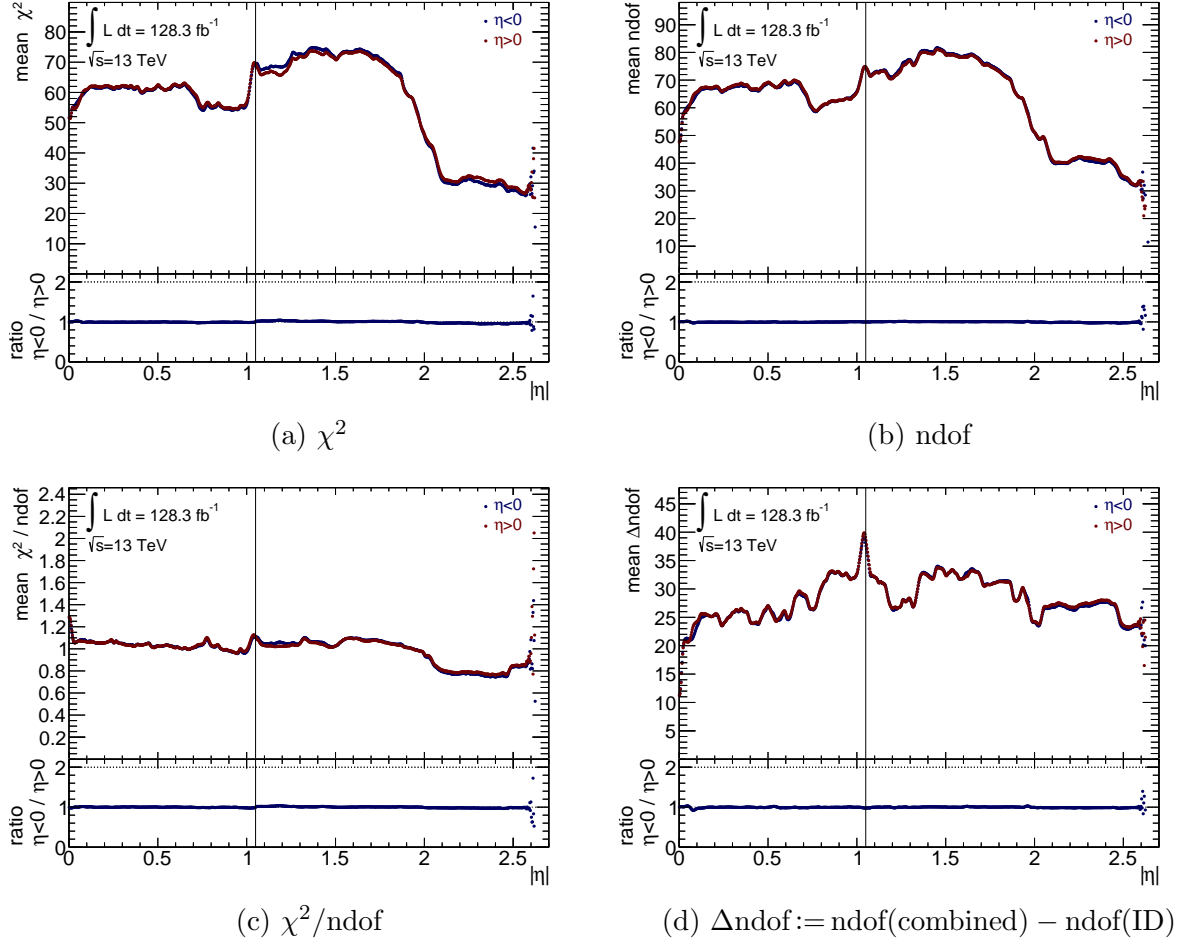


Figure A.5: Mean of track fit parameters versus $|\eta|$, separated into $\eta < 0$ (blue) and $\eta > 0$ (red). Shown are χ^2 (a), ndof (b), χ^2/ndof (c) and the difference between ndof for the combined track particle and for the Inner-Detector track particle (d). The vertical black line marks the approximate border of the ATLAS barrel region. Given are also the ratios for corresponding $\eta < 0$ and $\eta > 0$ graphs in all figures.

Appendix B

Attempt for an analytical propagation-time correction for RPCs

During the calibration procedure, a strong dependency of the timing information t_0 on ϕ was observed for RPC η -strips, as shown in Figure B.1. Looking closely, a sawtooth structure along ϕ can be noted that is repeated multiple times along t_0 . As the sawtooth feature seems to consist of 16 "V"-like structures that are placed along ϕ next to each other, it stands to reason that this is connected to the 16 ϕ -sectors the muon spectrometer is divided into. Indeed, the ϕ position of the bottom tip of each "V", as drawn exemplary in Figure B.1, corresponds exactly to the centre of the sectors in ϕ . In addition, those "V"-like structures are also repeated along the t_0 -axis.

The structures could be explained as follows: When the signal of a hit on an RPC η -strip reaches the readout, the time the signal took to propagate along the strip is unknown. Therefore, in a first step, it is corrected for the centre of the strip in ϕ , i.e., the centre of the ϕ -sector. During reconstruction, the propagation time then has to be recalculated from the position of the hit that can be determined by matching the corresponding RPC ϕ -strip timing information. If this recalculated propagation time yields a systematic error, e.g., by overestimating the propagation time of the signal along the strip or a different definition of the strip centre, a overestimation of t_0 will be observed that increases with the distance of the hit from the sector centre. Adding the readout timing-granularity of RPCs to this, the repetition of "V"s along t_0 can be explained.

Lacking a propagation-time information in R21, as was available in R20.7, the general hypothesis can only be tested by investigating the dependence of t_0 on the distance from the strip centre in ϕ , d_ϕ . This is calculated according to

$$d_\phi = |r \cdot \sin(\phi_i - \phi_{\text{chamber}})|,$$

where r is the distance from the IP in transverse plane, ϕ_i is the ϕ position of the hit

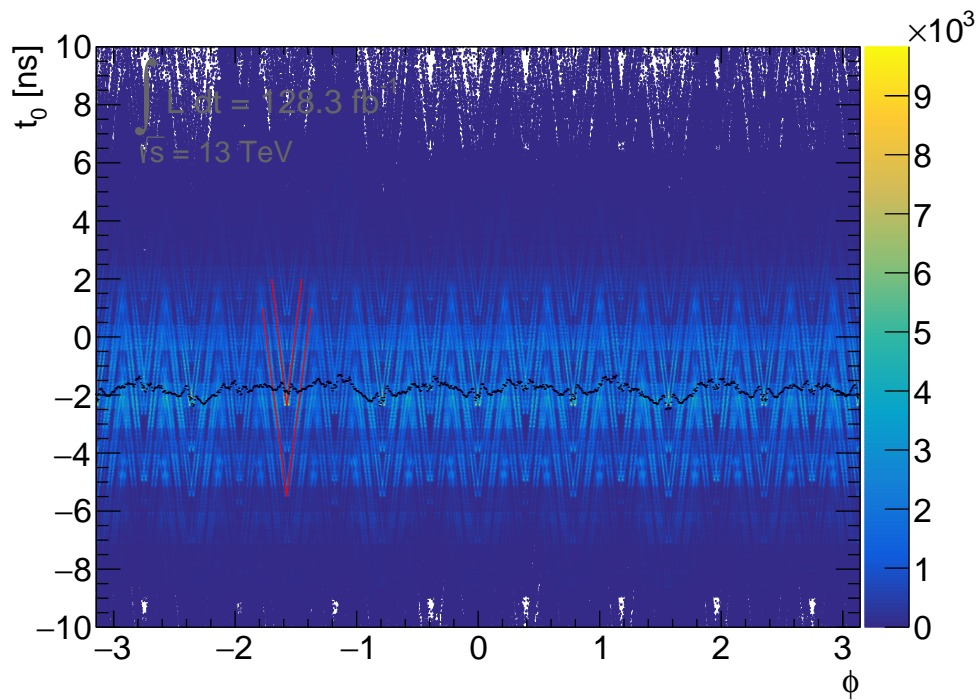


Figure B.1: t_0 versus ϕ of hits in RPC η -strips before calibration. Two of the periodically repeated, "V"-like structures along ϕ are marked in red. The means of the ϕ -bins are drawn in black.

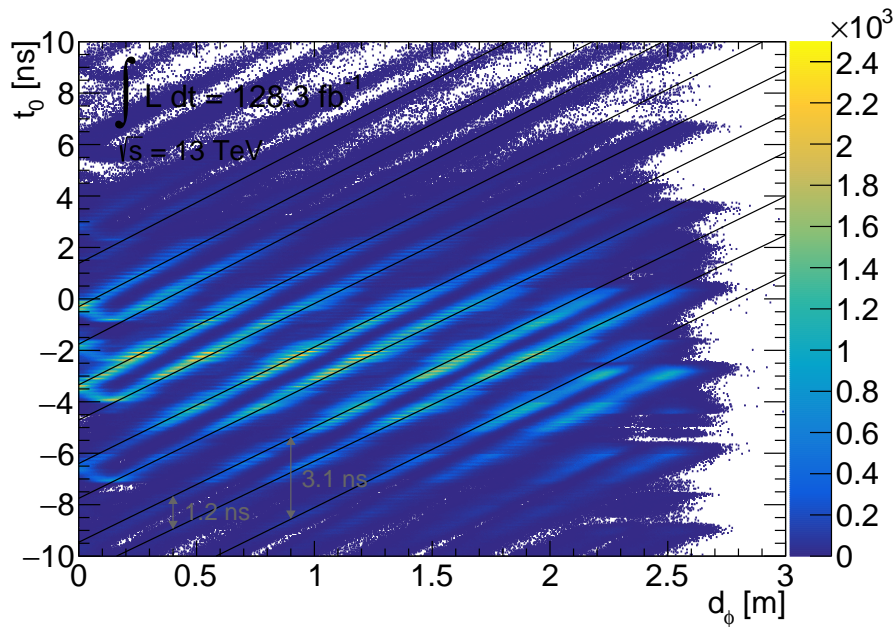


Figure B.2: t_0 of a hit versus the distance of the hit from the centre of the chamber in ϕ , d_ϕ , for RPC η -strips in station 4 (BOL) before calibration. Fits to the visible t_0 - d_ϕ -dependencies are drawn in black lines. The temporal distance between next-to-neighbouring fits is approximately 3.1 ns, compatible with the RPC readout timing-granularity. Two neighbouring fits each form pairs with a distance of about 1.2 ns.

and ϕ_{chamber} is the ϕ position of the centre of the chamber. As the different stations in the muon spectrometer have independent electronics that lead to slightly different timing delays, to observe a meaningful t_0 - d_ϕ -relation, stations have to be considered separately. Figure B.2 shows exemplary the distribution obtained for station 4, which represents large sectors of the outer detector layer of the barrel region (BOL). As expected, a very clear linear dependency is visible, which is fitted with linear functions that are drawn as black lines in the figure. The distances in t_0 between next-to-neighbouring fits are approximately 3.1 ns, consistent with the readout timing-granularity of 3.125 ns generally visible for RPCs. However, also a smaller substructure with a distance of about 1.2 ns is observed, relating two neighbouring fits each that are connected with a highly populated region at low d_ϕ . At the time of writing, although the ATLAS RPC experts were consulted and investigations carried out, no explanation could be found for this feature.

Having proven the connection between the structures seen in Figure B.1 and the distance of the hit from the readout, it can be attempted to correct for this effect. For this, the fits in Figure B.2, which follow the equation

$$t_0(d_\phi) = m \cdot d_\phi + n,$$

are used: For each station, the means of m , \bar{m} , and n , \bar{n} , are taken, weighted according

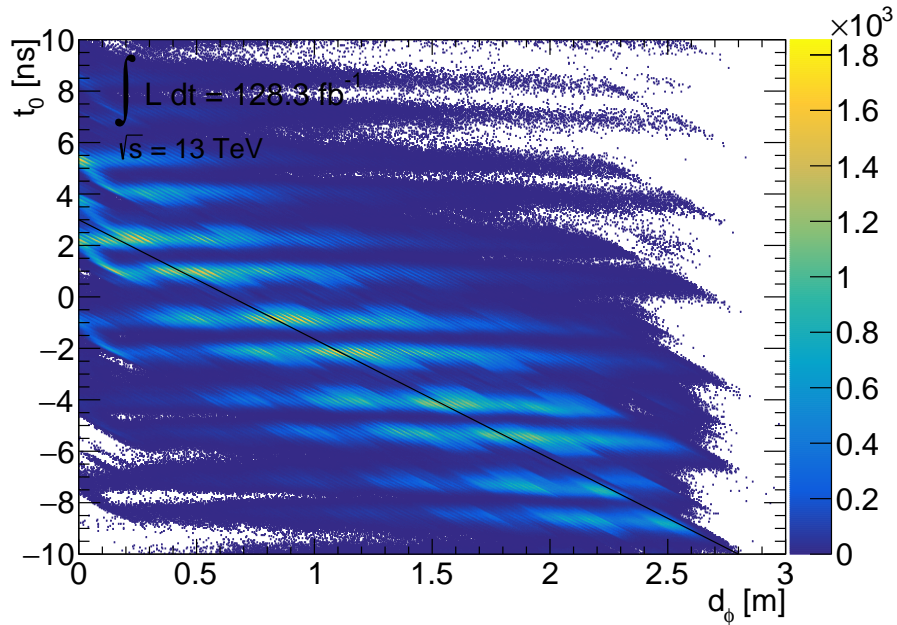


Figure B.3: t_0 of a hit versus the distance of the hit from the centre of the chamber in ϕ , d_ϕ , for RPC η -strips in station 4 (BOL) after the propagation-time correction described in this chapter. The visible correlation between t_0 and d_ϕ is marked with a black line.

to the fits' uncertainties. This results in average slopes \bar{m} in the range of 0.0043 ns/mm to 0.0046 ns/mm, corresponding to velocities between 217 mm/ns and 233 mm/ns. Intriguingly, this is close to the nominal value for the propagation velocity of signals along RPC strips, 208 mm/ns [119]. At the time of writing, however, it is yet unknown whether this resemblance is of coincidental or systematic nature. From \bar{m} and \bar{n} , the dependency of t_0 on d_ϕ can be corrected by rotating the matrix represented by Figure B.2 by the angle $\alpha = \arctan(\bar{m})$ between fit and d_ϕ -axis. This correction corresponds for each value t_0^{in} to

$$t_0^{\text{out}} = -\sin \alpha \cdot d_\phi + \cos \alpha \cdot t_0^{\text{in}} - \bar{n}.$$

Plotting t_0 versus d_ϕ for hits in RPC η -strips after this correction yields Figure B.3. Here, the dependencies of t_0 on d_ϕ seen in Figure B.2 have been removed. However, as no correction was attempted for this, the 3.125 ns structure and its 1.2 ns substructure remain. In addition, a new correlation between t_0 and d_ϕ was introduced by rotating, unfortunately, that is marked with a black line in Figure B.3. This correlation can of course also be noted when investigating the t_0 - ϕ -dependence after this propagation-time correction, which is shown in Figure B.4. It expresses itself as inverted "V"-like structures where again the tip of the "V" is located at the centre of the sector in ϕ .

Of course, it could be attempted to correct also this new inverted "V"-like dependency. However, while the 3.125 ns is understood and of no further concern, also the 1.2 ns substructure, which is of completely unknown origin, remained. In consequence, to not intro-

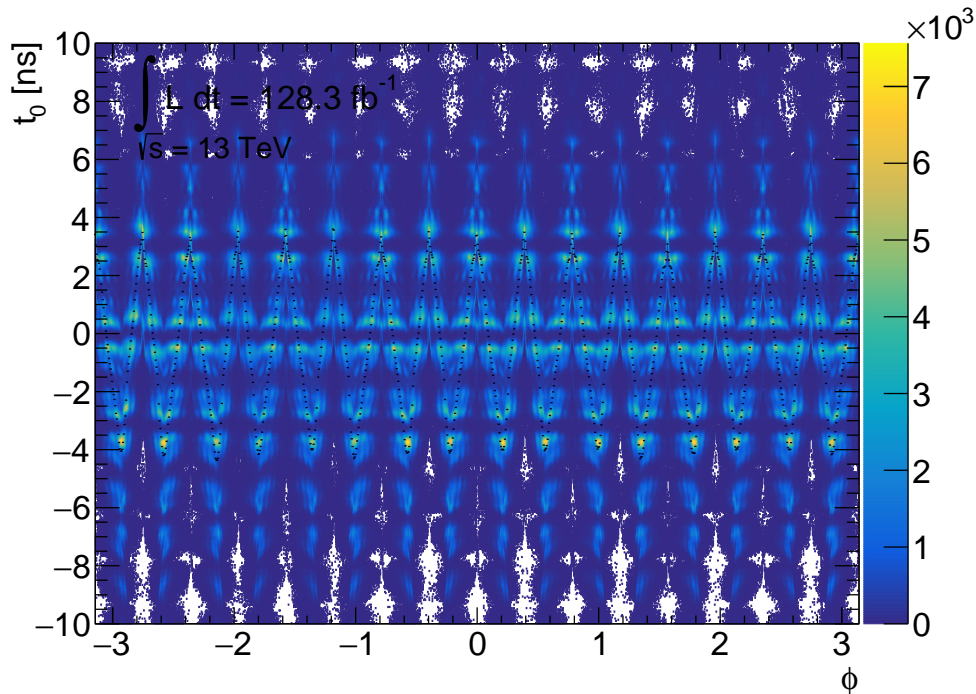


Figure B.4: t_0 versus ϕ of hits in RPC η -strips after the propagation-time correction described in this chapter. The means of the ϕ -bins are drawn in black.

duce any bias or new mistakes while correcting for the erroneously calculated propagation time, the propagation-time correction described in this chapter was abandoned, for now. Nevertheless, as soon as better understanding of the reasons for the observed dependencies is acquired, a renewed attempt on this calibration procedure can be started.

An approach similar to that for RPC η -strips could be conducted to correct the corresponding dependencies of t_0 on z for RPC ϕ -strips as shown in Figure B.5a. Here, the structure is less clear as the dependencies, a few of which are marked in red, overlap. The reason for this is that the detector is not as symmetric in z as it is in ϕ , in particular when comparing the different detector layers. Hence, a first step would have to be to remove this overlap by separating the hits by the station they were registered in. In addition, separating the RPC chambers according to their readout position gives an even clearer picture of the dependencies. This can be done as RPC chambers are segmented into modules in z direction, incorporated into the variable DoubletZ of a strip as mentioned in Figure 3.12. Figure B.5b shows the result of these separations for the large sector of a barrel station in the middle detector layer (BOL) with DoubletZ = 1. Nevertheless, as no different result than that for RPC η -strips can be expected, in the end, also this propagation-time correction is not pursued further for now. Instead, the modest propagation-time calibration as described in Section 5.6.2 is adopted.

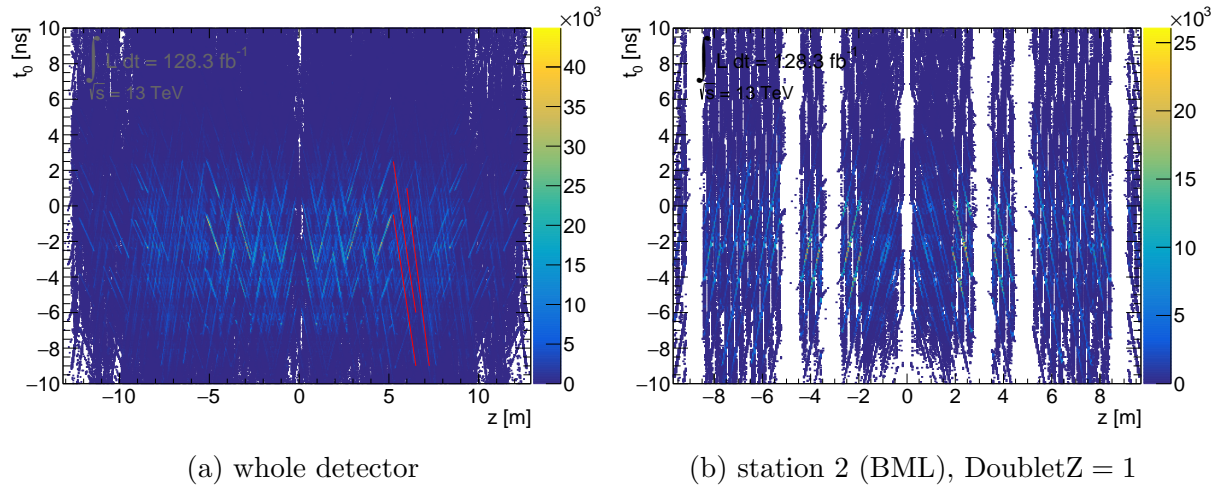


Figure B.5: (a) t_0 versus z of hits in RPC ϕ -strips before any calibration. A few selected dependencies of t_0 on z are marked in red. (b) t_0 versus z of hits in RPC ϕ -strips in station 2 (BML) with DoubletZ = 1 before any calibration.

Bibliography

- [1] G. Altarelli, *Collider Physics within the Standard Model – A Primer*, vol. 937 of *Lecture Notes in Physics*. Springer, Cham, 2017.
- [2] D. Griffiths, *Introduction to Elementary Particles*. WILEY-VCH Verlag GmbH & Co. KGaA, Weinheim, 2004.
- [3] A. Pich, *The Standard Model of Electroweak Interactions*. 2005.
`arXiv:hep-ph/0502010v1`.
- [4] “Wikipedia: Standard Model.”
https://en.wikipedia.org/wiki/Standard_Model. Accessed: Sept 7, 2018.
- [5] ATLAS Collaboration, “Observation of a new particle in the search for the Standard Model Higgs boson with the ATLAS detector at the LHC,” *Phys. Lett. B* **716** (2012) 1, `arXiv:1207.7214 [hep-ex]`.
- [6] CMS Collaboration, “Observation of a new boson at a mass of 125 GeV with the CMS experiment at the LHC,” *Phys. Lett. B* **716** (2012) 30, `arXiv:1207.7235 [hep-ex]`.
- [7] ATLAS Collaboration, “Observation of $H \rightarrow b\bar{b}$ decays and VH production with the ATLAS detector,” `arXiv:1808.08238 [hep-ex]`.
- [8] CMS Collaboration, “Observation of Higgs boson decay to bottom quarks,” `arXiv:1808.08242 [hep-ex]`.
- [9] A. Bettini, *Introduction to Elementary Particle Physics*. Cambridge University Press, 2008.
- [10] S. L. Glashow, J. Iliopoulos, and L. Maiani, “Weak Interactions with Lepton-Hadron Symmetry,” *Phys. Rev. D* **2** (Oct, 1970) 1285–1292.
- [11] M. Kobayashi and T. Maskawa, “CP-Violation in the Renormalizable Theory of Weak Interaction,” *PTP* **49** no. 2, (1973) 652–657.
- [12] S. Weinberg, “A Model of Leptons,” *Phys. Rev. Lett.* **19** (Nov, 1967) 1264–1266.

- [13] P. W. Higgs, “Broken Symmetries and the Masses of Gauge Bosons,” *Phys. Rev. Lett.* **13** (Oct, 1964) 508–509.
- [14] SNO Collaboration, “Electron energy spectra, fluxes, and day-night asymmetries of ^8B solar neutrinos from measurements with NaCl dissolved in the heavy-water detector at the Sudbury Neutrino Observatory,” *Phys. Rev. C* **72** (Nov, 2005) 055502, [arXiv:nucl-ex/0502021](#).
- [15] M. Gavela *et al.*, “Standard Model CP-Violation and baryon asymmetry,” *MPLA* **09** no. 09, (1994) 795–809, [arXiv:hep-ph/9312215](#).
- [16] Garrett, Katherine and Dūda, Gintaras, “Dark Matter: A Primer,” *Advances in Astronomy* (2011) .
- [17] Particle Data Group, “Review of Particle Physics: Grand Unified Theories,” *Phys. Rev. D* **98** (Aug, 2018) 030001.
- [18] M. E. Peskin, “Beyond the Standard Model,” [arXiv:hep-ph/9705479](#).
- [19] S. P. Martin, *Perspectives on Supersymmetry*, vol. 18 of *Advanced Series on Directions in High Energy Physics*, ch. A Supersymmetry Primer, pp. 1–98. World Scientific, 1998. [arXiv:hep-ph/9709356](#).
- [20] XENON100 Collaboration, “First axion results from the XENON100 experiment,” *Phys. Rev. D* **90** (Sept, 2014) 062009, [arXiv:1404.1455](#).
- [21] Yu. A. Golfand and E. P. Likhtman, “Extension of the Algebra of Poincare Group Generators and Violation of p Invariance,” *JETP Lett.* **13** (1971) 323. [*Pisma Zh. Eksp. Teor. Fiz.* **13** (1971) 452].
- [22] D. V. Volkov and V. P. Akulov, “Is the Neutrino a Goldstone Particle?,” *Phys. Lett. B* **46** (1973) 109.
- [23] J. Wess and B. Zumino, “Supergauge Transformations in Four-Dimensions,” *Nucl. Phys. B* **70** (1974) 39.
- [24] J. Wess and B. Zumino, “Supergauge Invariant Extension of Quantum Electrodynamics,” *Nucl. Phys. B* **78** (1974) 1.
- [25] S. Ferrara and B. Zumino, “Supergauge Invariant Yang-Mills Theories,” *Nucl. Phys. B* **79** (1974) 413.
- [26] A. Salam and J. A. Strathdee, “Supersymmetry and Nonabelian Gauges,” *Phys. Lett. B* **51** (1974) 353.
- [27] N. Sakai, “Naturalness in Supersymmetric Guts,” *Z. Phys. C* **11** (1981) 153.

- [28] S. Dimopoulos, S. Raby, and F. Wilczek, “Supersymmetry and the Scale of Unification,” *Phys. Rev. D* **24** (1981) 1681.
- [29] L. E. Ibanez and G. G. Ross, “Low-Energy Predictions in Supersymmetric Grand Unified Theories,” *Phys. Lett. B* **105** (1981) 439.
- [30] S. Dimopoulos and H. Georgi, “Softly Broken Supersymmetry and SU(5),” *Nucl. Phys. B* **193** (1981) 150.
- [31] H. Goldberg, “Constraint on the Photino Mass from Cosmology,” *Phys. Rev. Lett.* **50** (1983) 1419. Erratum: *Phys. Rev. Lett.* **103** (2009) 099905.
- [32] J. R. Ellis, J. S. Hagelin, D. V. Nanopoulos, K. A. Olive, and M. Srednicki, “Supersymmetric Relics from the Big Bang,” *Nucl. Phys. B* **238** (1984) 453.
- [33] M. Dine, *Supersymmetry and String Theory: Beyond the Standard Model*. Cambridge University Press, 2 ed., 2016.
- [34] J. A. Bagger, “Weak-Scale Supersymmetry: Theory and Practice,” [arXiv:hep-ph/9604232](https://arxiv.org/abs/hep-ph/9604232).
- [35] P. Fayet, “Supersymmetry and Weak, Electromagnetic and Strong Interactions,” *Phys. Lett. B* **64** (1976) 159.
- [36] P. Fayet, “Spontaneously Broken Supersymmetric Theories of Weak, Electromagnetic and Strong Interactions,” *Phys. Lett. B* **69** (1977) 489.
- [37] I. J. R. Aitchison, “Supersymmetry and the MSSM: An Elementary Introduction,” [arXiv:hep-ph/0505105](https://arxiv.org/abs/hep-ph/0505105).
- [38] Super-Kamiokande Collaboration, “Search for Proton Decay via $p \rightarrow e^+ \pi^0$ and $p \rightarrow \mu^+ \pi^0$ in a Large Water Cherenkov Detector,” *Phys. Rev. Lett.* **102** (Apr, 2009) 141801, [arXiv:0903.0676](https://arxiv.org/abs/0903.0676).
- [39] G. R. Farrar and P. Fayet, “Phenomenology of the Production, Decay, and Detection of New Hadronic States Associated with Supersymmetry,” *Phys. Lett. B* **76** (1978) 575.
- [40] R. Barbieri and G. F. Giudice, “Upper Bounds on Supersymmetric Particle Masses,” *Nucl. Phys. B* **306** (1988) 63.
- [41] B. de Carlos and J. A. Casas, “One loop analysis of the electroweak breaking in supersymmetric models and the fine tuning problem,” *Phys. Lett. B* **309** (1993) 320, [arXiv:hep-ph/9303291](https://arxiv.org/abs/hep-ph/9303291).
- [42] ATLAS Collaboration, “Summary of the searches for squarks and gluinos using $\sqrt{s} = 8$ TeV pp collisions with the ATLAS experiment at the LHC,” *JHEP* **10** (2015) 054, [arXiv:1507.05525](https://arxiv.org/abs/1507.05525) [hep-ex].

- [43] ATLAS Collaboration, “Search for electroweak production of supersymmetric particles in final states with two or three leptons at $\sqrt{s} = 13$ TeV with the ATLAS detector,” [arXiv:1803.02762](https://arxiv.org/abs/1803.02762) [hep-ex].
- [44] ATLAS Collaboration, “Summary of the ATLAS experiment’s sensitivity to supersymmetry after LHC Run 1 — interpreted in the phenomenological MSSM,” *JHEP* **10** (2015) 134, [arXiv:1508.06608](https://arxiv.org/abs/1508.06608) [hep-ex].
- [45] H. Baer *et al.*, “What hadron collider is required to discover or falsify natural supersymmetry?,” *Phys. Lett. B* **774** (2017) 451 – 455.
- [46] S. Diglio, L. Feligioni, and G. Moulhaka, “Stashing the stops in multijet events at the LHC,” *Phys. Rev. D* **96** (Sept, 2017) 055032, [arXiv:1611.05850](https://arxiv.org/abs/1611.05850).
- [47] T. Flacke *et al.*, “Electroweak Kaluza-Klein dark matter,” *JHEP* **2017** no. 4, (Apr, 2017) 41.
- [48] M. Fairbairn *et al.*, “Stable Massive Particles at Colliders,” *Phys. Rept.* **438** no. 1, (2007) 1 – 63. <https://www.osti.gov/biblio/899067>.
- [49] ATLAS Collaboration, “The ATLAS Experiment at the CERN Large Hadron Collider,” *JINST* **3** (2008) S08003.
- [50] L. Evans and P. Bryant, “LHC Machine,” *JINST* **3** no. 08, (2008) S08001.
- [51] “LHC: the guide.” <http://cds.cern.ch/record/2255762/files/CERN-Brochure-2017-002-Eng.pdf>. Accessed: Sept 20, 2018.
- [52] U. Ellwanger, *Vom Universum zu den Elementarteilchen*. Springer Spektrum, Berlin, Heidelberg, 3 ed., 2015.
- [53] “The CERN accelerator complex - August 2018.” <http://cds.cern.ch/record/2636343/>. Accessed: Oct 15, 2018.
- [54] SuperKEKB Collaboration, “Accelerator design at SuperKEKB,” *PTEP* **2013** no. 3, (2013) 03A011.
- [55] W. Herr and B. Muratori, “Concept of luminosity,” <https://www.researchgate.net/publication/267198803>.
- [56] “ATLAS: Luminosity Public Results Run 2.” <https://twiki.cern.ch/twiki/bin/view/AtlasPublic/LuminosityPublicResultsRun2>. Accessed: Oct 28, 2018.
- [57] “ATLAS Homepage.” <http://atlas.cern>. Accessed: Sept 26, 2018.

- [58] K. A. Assamagan *et al.*, “A Hierarchical Software Identifier Scheme for the ATLAS Muon Spectrometer; rev. version,” Tech. Rep. ATL-MUON-2004-003, CERN, Geneva, Aug, 2002. <https://cds.cern.ch/record/681542>.
- [59] Y. Abulaiti, *Search for Pair-Produced Supersymmetric Top Quark Partners with the ATLAS Experiment*. PhD thesis, Stockholm U., Aug, 2016. <http://inspirehep.net/record/1485383>.
- [60] ATLAS TDAQ Collaboration, “The ATLAS Data Acquisition and High Level Trigger system,” *JINST* **11** no. 06, (2016) P06008.
- [61] J. Stelzer and the ATLAS collaboration, “The ATLAS High Level Trigger Configuration and Steering: Experience with the First 7 TeV Collision Data,” *JPCS* **331** no. 2, (2011) 022026.
- [62] ATLAS Collaboration, *ATLAS Inner Detector: Technical Design Report. Vol. 1*. Technical Design Report ATLAS. CERN, Geneva, 1997. <http://inspirehep.net/record/455672>.
- [63] L. Scodellaro and the ATLAS and CMS Collaborations, “b tagging in ATLAS and CMS,” in *5th Large Hadron Collider Physics Conference (LHCP 2017) Shanghai, China, May 15-20, 2017*. 2017. arXiv:1709.01290.
- [64] A. L. Rosa, “ATLAS IBL Pixel Upgrade,” *Nucl. Phys. B - Proceedings Supplements* **215** no. 1, (2011) 147 – 150, arXiv:1104.1980.
- [65] ATLAS Collaboration, *ATLAS Liquid-Argon Calorimeter: Technical Design Report*. Technical Design Report ATLAS. CERN, Geneva, 1996. <http://cds.cern.ch/record/331061>.
- [66] ATLAS Collaboration, *ATLAS Tile Calorimeter: Technical Design Report*. Technical Design Report ATLAS. CERN, Geneva, 1996. <http://cds.cern.ch/record/331062>.
- [67] J. Wotschack, “ATLAS Muon Chamber Construction Parameters for CSC, MDT, and RPC chambers,” tech. rep., CERN, Geneva, Apr, 2008. <https://cds.cern.ch/record/1099400>.
- [68] ATLAS Collaboration, *ATLAS Muon Spectrometer: Technical Design Report*. Technical Design Report ATLAS. CERN, Geneva, 1997. <https://cds.cern.ch/record/331068>.
- [69] ATLAS Collaboration, “Standalone vertex finding in the ATLAS muon spectrometer,” *JINST* **9** (2014) P02001.

- [70] J. Dubbert *et al.*, “Performance of the ATLAS Muon Drift-Tube Chambers at High Background Rates and in Magnetic Fields,” tech. rep., Apr, 2016.
arXiv:1604.01598.
- [71] G. Carlino *et al.*, “The RPC Level-1 muon trigger of the ATLAS experiment at the LHC,” in *14th IEEE-NPSS Real Time Conference, 2005*, vol. 3, p. 4. June, 2005.
<https://cds.cern.ch/record/934478>.
- [72] ATLAS Collaboration, “Measurement of the W -boson mass in pp collisions at $\sqrt{s} = 7$ TeV with the ATLAS detector,” *Eur. Phys. J. C* **78** (2018) 110,
arXiv:1701.07240 [hep-ex].
- [73] ATLAS Collaboration, “Measurement of the cross-section for producing a W boson in association with a single top quark in pp collisions at $\sqrt{s} = 13$ TeV with ATLAS,” *JHEP* **01** (2018) 063, arXiv:1612.07231 [hep-ex].
- [74] ATLAS Collaboration, “Measurements of electroweak Wjj production and constraints on anomalous gauge couplings with the ATLAS detector,” *Eur. Phys. J. C* **77** (2017) 474, arXiv:1703.04362 [hep-ex].
- [75] ATLAS Collaboration, “Search for heavy particles decaying into top-quark pairs using lepton-plus-jets events in proton–proton collisions at $\sqrt{s} = 13$ TeV with the ATLAS detector,” *Eur. Phys. J.* (2018) , arXiv:1804.10823 [hep-ex].
- [76] ATLAS Collaboration, “Search for additional heavy neutral Higgs and gauge bosons in the ditau final state produced in 36 fb^{-1} of pp collisions at $\sqrt{s} = 13$ TeV with the ATLAS detector,” *JHEP* **01** (2018) 055, arXiv:1709.07242 [hep-ex].
- [77] ATLAS Collaboration, “Search for chargino—neutralino production using recursive jigsaw reconstruction in final states with two or three charged leptons in proton–proton collisions at $\sqrt{s} = 13$ TeV with the ATLAS detector,”
arXiv:1806.02293 [hep-ex].
- [78] ATLAS Collaboration, “Search for long-lived charginos based on a disappearing-track signature in pp collisions at $\sqrt{s} = 13$ TeV with the ATLAS detector,” *JHEP* **06** (2018) 022, arXiv:1712.02118 [hep-ex].
- [79] ATLAS Collaboration, “Search for long-lived, massive particles in events with displaced vertices and missing transverse momentum in $\sqrt{s} = 13$ TeV pp collisions with the ATLAS detector,” *Phys. Rev. D* **97** (2018) 052012, arXiv:1710.04901 [hep-ex].
- [80] ATLAS Collaboration, “Searches for heavy long-lived charged particles with the ATLAS detector in proton–proton collisions at $\sqrt{s} = 8$ TeV,” *JHEP* **01** (2015) 068,
arXiv:1411.6795 [hep-ex].

- [81] ATLAS Collaboration, “Search for heavy long-lived charged R -hadrons with the ATLAS detector in 3.2 fb^{-1} of proton–proton collision data at $\sqrt{s} = 13 \text{ TeV}$,” *Phys. Lett. B* **760** (2016) 647, [arXiv:1606.05129](https://arxiv.org/abs/1606.05129) [hep-ex].
- [82] ATLAS Collaboration, “Search for heavy long-lived charged particles with the ATLAS detector in $36.1/\text{fb}$ of proton–proton collision data at $\sqrt{s} = 13 \text{ TeV}$.” To be submitted to: *Phys. Rev. D*, <https://cds.cern.ch/record/2318724>.
- [83] H. Paetz gen. Schieck, *Nuclear Reactions: An Introduction*. Springer, Berlin, Heidelberg, 2014.
- [84] ATLAS Collaboration, “Search for heavy charged long-lived particles in proton-proton collisions at $\sqrt{s} = 13 \text{ TeV}$ using an ionisation measurement with the ATLAS detector.” Submitted to *Phys. Lett. B* (2018), [arXiv:1808.04095](https://arxiv.org/abs/1808.04095).
- [85] C. M. Becchi and M. D’Elia, *Introduction to the Basic Concepts of Modern Physics: Special Relativity, Quantum and Statistical Physics*. Springer, Milano, 2010.
- [86] C. Graham and D. Talay, *Stochastic Simulation and Monte Carlo Methods*. Springer, Berlin, Heidelberg, 2013.
- [87] D. Fassouliotis *et al.*, “Muon Identification using the MUID package,” Tech. Rep. ATL-COM-MUON-2003-003, CERN, Geneva, Nov, 2000. <https://cds.cern.ch/record/681596>.
- [88] R. Nicolaidou *et al.*, “Muon identification procedure for the ATLAS detector at the LHC using Muonboy reconstruction package and tests of its performance using cosmic rays and single beam data,” *JPCS* **219** no. 3, (2010) 032052. <http://stacks.iop.org/1742-6596/219/i=3/a=032052>.
- [89] S. Tarem *et al.*, “MuGirl – Muon identification in the ATLAS detector from the inside out,” in *2006 IEEE Nuclear Science Symposium Conference Record*, vol. 1, pp. 617–621. Oct, 2006.
- [90] G. Ordóñez Sanz, *Muon Identification in the ATLAS Calorimeters*. PhD thesis, Radboud University Nijmegen, June, 2009. https://www.nikhef.nl/pub/services/biblio/theses_pdf/thesis_G_Ordenez_Sanz.pdf.
- [91] S. Tarem *et al.*, “Trigger and reconstruction for heavy long-lived charged particles with the ATLAS detector,” *Eur. Phys. J. C* **62** no. 2, (Jul, 2009) 281–292.
- [92] J. Alwall, M.-P. Le, M. Lisanti, and J. G. Wacker, “Searching for Directly Decaying Gluinos at the Tevatron,” *Phys. Lett. B* **666** (2008) 34, [arXiv:0803.0019](https://arxiv.org/abs/0803.0019) [hep-ph].

- [93] J. Alwall, P. Schuster, and N. Toro, “Simplified Models for a First Characterization of New Physics at the LHC,” *Phys. Rev. D* **79** (2009) 075020, arXiv:0810.3921 [hep-ph].
- [94] D. Alves *et al.*, “Simplified Models for LHC New Physics Searches,” *J. Phys. G* **39** (2012) 105005, arXiv:1105.2838 [hep-ph].
- [95] J. J. Heinrich, *Search for charged stable massive particles with the ATLAS detector*. PhD thesis, Ludwig-Maximilians-Universität München, Mar, 2018.
http://www.etp.physik.uni-muenchen.de/publications/theses/download/phd_jheinrich.pdf.
- [96] M. Adersberger, “Studies on Velocity Measurements with the ATLAS Calorimeters for the Search for Heavy Long-Lived Particles,” Master’s thesis, Ludwig-Maximilians-Universität München, June, 2015. http://www.etp.physik.uni-muenchen.de/publications/theses/download/dipl_adersberger.pdf.
- [97] ATLAS Collaboration, “Luminosity determination in pp collisions at $\sqrt{s} = 8$ TeV using the ATLAS detector at the LHC,” *Eur. Phys. J. C* **76** (2016) 653, arXiv:1608.03953 [hep-ex].
- [98] G. Avoni *et al.*, “The new LUCID-2 detector for luminosity measurement and monitoring in ATLAS,” *JINST* **13** no. 07, (2018) P07017.
- [99] T. Sjöstrand, S. Mrenna, and P. Skands, “A brief introduction to PYTHIA 8.1,” *Computer Physics Communications* **178** no. 11, (2008) 852 – 867, arXiv:0710.3820.
- [100] D. J. Lange, “The EvtGen particle decay simulation package,” *Nucl. Instrum. Methods Phys. Res., Sect. A: Accelerators, Spectrometers, Detectors and Associated Equipment* **462** no. 1, (2001) 152 – 155. BEAUTY2000, Proceedings of the 7th Int. Conf. on B-Physics at Hadron Machines.
- [101] S. Alioli *et al.*, “A general framework for implementing NLO calculations in shower Monte Carlo programs: the POWHEG BOX,” *JHEP* **2010** no. 6, (June, 2010) 43.
- [102] J. Pumplin *et al.*, “New Generation of Parton Distributions with Uncertainties from Global QCD Analysis,” *JHEP* **2002** no. 07, (2002) 012.
- [103] ATLAS Collaboration, “Measurement of the Z/γ^* boson transverse momentum distribution in pp collisions at $\sqrt{s}=7$ TeV with the ATLAS detector,” *JHEP* **2014** no. 9, (Sept, 2014) 145.
- [104] M. Dine and W. Fischler, “A Phenomenological Model of Particle Physics Based on Supersymmetry,” *Phys. Lett. B* **110** (1982) 227.

- [105] L. Alvarez-Gaume, M. Claudson, and M. B. Wise, “Low-Energy Supersymmetry,” *Nucl. Phys. B* **207** (1982) 96.
- [106] C. R. Nappi and B. A. Ovrut, “Supersymmetric Extension of the $SU(3) \times SU(2) \times U(1)$ Model,” *Phys. Lett. B* **113** (1982) 175.
- [107] J. Alwall *et al.*, “The automated computation of tree-level and next-to-leading order differential cross sections, and their matching to parton shower simulations,” *JHEP* **2014** no. 7, (Jul, 2014) 79.
- [108] R. D. Ball *et al.*, “Parton distributions with LHC data,” *Nucl. Phys. B* **867** no. 2, (2013) 244 – 289, [arXiv:1207.1303](https://arxiv.org/abs/1207.1303).
- [109] “ATLAS Run 1 Pythia8 tunes,” Tech. Rep. ATL-PHYS-PUB-2014-021, CERN, Geneva, Nov, 2014. <https://cds.cern.ch/record/1966419>.
- [110] G. F. Giudice, M. A. Luty, H. Murayama, and R. Rattazzi, “Gaugino mass without singlets,” *JHEP* **12** (1998) 027, [arXiv:hep-ph/9810442](https://arxiv.org/abs/hep-ph/9810442).
- [111] L. Randall and R. Sundrum, “Out of this world supersymmetry breaking,” *Nucl. Phys. B* **557** (1999) 79, [arXiv:hep-th/9810155](https://arxiv.org/abs/hep-th/9810155).
- [112] ATLAS Collaboration, “The ATLAS Simulation Infrastructure,” *Eur. Phys. J. C* **70** no. 3, (Dec, 2010) 823–874.
- [113] S. Agostinelli *et al.*, “Geant4—a simulation toolkit,” *Nucl. Instrum. Methods Phys. Res., Sect. A: Accelerators, Spectrometers, Detectors and Associated Equipment* **506** no. 3, (2003) 250 – 303.
- [114] “Summary of ATLAS Pythia 8 tunes,” Tech. Rep. ATL-PHYS-PUB-2012-003, CERN, Geneva, Aug, 2012. <https://cds.cern.ch/record/1474107>.
- [115] A. D. Martin *et al.*, “Parton distributions for the LHC,” *Eur. Phys. J. C* **63** no. 2, (Sept, 2009) 189–285, [arXiv:0901.0002](https://arxiv.org/abs/0901.0002).
- [116] M. Adersberger, *Searches for Heavy Charged Long-Lived Particles with the ATLAS Detector*. PhD thesis, Ludwig-Maximilians-Universität München, Nov, 2018. To be published.
- [117] T. Adye, “Unfolding algorithms and tests using RooUnfold,” in *Proceedings of the PHYSTAT 2011 Workshop on Statistical Issues Related to Discovery Claims in Search Experiments and Unfolding*, H. B. Prosper and L. Lyons, eds., pp. 313–318. Geneva, May, 2011. <https://cds.cern.ch/record/1349242>.
- [118] R. Brun and F. Rademakers, “ROOT – An object oriented data analysis framework,” *Nucl. Instrum. Methods Phys. Res., Sect. A: Accelerators, Spectrometers, Detectors and Associated Equipment* **389** no. 1, (1997) 81 – 86. New Computing Techniques in Physics Research V.

- [119] G. Chiodini, S. Spagnolo, and the ATLAS Collaboration, “Off-line time calibration of the ATLAS RPC system,” *JINST* **8** no. 02, (2013) T02004.

List of Abbreviations

ALICE	A Large Ion Collider Experiment, one of the four main experiments at the Large Hadron Collider.
AMSB	Anomaly-mediated symmetry breaking, breaking of supersymmetry through conformal anomaly.
BC	Bunch crossing, the collision of two proton bunches at the interaction point in ATLAS.
BSM	Beyond the Standard Model, term for theories extending the Standard Model.
CERN	European Organization for Nuclear Research, a research organisation for particle physics based in Geneva, Switzerland.
CMB	Cosmic microwave background, electromagnetic radiation that is a remains of the Big Bang.
CMS	Compact Muon Solenoid, a multi-purpose particle detector, one of the four main experiments at the Large Hadron Collider.
CSC	Cathode-strip chamber, (basic element of) one of the subdetector systems in the ATLAS muon spectrometer, responsible for precision measurements in the forward region.
DxAOD	Derived analysis-object data, a data format that is derived from xAOD to reduce disk space and allow faster processing.
GMSB	Gauge-mediated symmetry breaking, breaking of supersymmetry through gauge-interactions in the Standard Model.
GUT	Grand Unified Theory, a theory unifying electroweak and strong interaction.

HLT	High-Level Trigger, a high-level, software-based trigger system in ATLAS.
IBL	Insertable B-Layer, the innermost layer of the pixel detector in ATLAS.
ID	Inner Detector, the innermost subdetector of ATLAS.
IP	Interaction point, the location of particle collisions in ATLAS.
KK	Kaluza-Klein, a term relating to the Kaluza-Klein theory (a theory introducing a fifth dimension).
L1	Level-1, a low-level, hardware-based trigger system in ATLAS.
LAr	Liquid argon, a cooled noble gas used in some ATLAS systems.
LEP	Large Electron–Positron Collider, a large particle collider at CERN that collided electrons and positrons.
LHC	Large Hadron Collider, the world’s largest and most powerful particle collider, colliding protons or heavy ions.
LHCb	Large Hadron Collider beauty, one of the four main experiments at the Large Hadron Collider.
LHCf	Large Hadron Collider forward, an experiment at the Large Hadron Collider.
Linac 2	Linear accelerator 2, a linear hadron accelerator at CERN.
LKP	Lightest Kaluza-Klein particle, the non-Standard Model particle in a Kaluza-Klein model with the lowest mass, a potential dark matter candidate if the Kaluza-Klein parity is conserved.
LLP	Long-lived particle, in the definition of this work, a particle with a high lifetime, allowing it to reach at least the Inner Detector of ATLAS within its mean lifetime.

LSP	Lightest supersymmetric particle, the non-Standard Model particle in a supersymmetric model with the lowest mass, a dark matter candidate if R -parity is conserved.
mAMSB	minimal anomaly-mediated symmetry breaking, anomaly-mediated symmetry breaking with an added universal constant term.
MC	Monte Carlo, a type of algorithm using random sampling, employed for simulations in ATLAS.
MDT	Monitored drift tube, (basic element of) one of the subdetector systems in the ATLAS muon spectrometer, responsible for precision measurements in the central region.
MoEDAL	Monopole and Exotics Detector at the LHC, an experiment at the Large Hadron Collider.
MPV	Most probable value, the value most likely to be observed in a distribution.
MS	Muon spectrometer, the outermost subdetector of ATLAS, designed for detecting muons.
MSSM	Minimal Supersymmetric (version of the) Standard Model, the supersymmetric model adding minimal additional particle content to the Standard Model.
MWPC	Multiwire proportional chamber, a type of detector measuring the ionisation in a gas caused by a passing particle.
ndof	number of degrees of freedom, the number of values in a calculation that are allowed to be varied, corresponds to the number of available data points if a fit is concerned.
NLSP	Next-to-lightest supersymmetric particle, the non-Standard Model particle in a supersymmetric model with the second-lowest mass, in some models a candidate for a charged stable massive particle.
PDF	Parton distribution function, probability density function to produce a particle with a certain momentum fraction in a collision.
PS	Proton Synchrotron, a circular hadron accelerator at CERN, larger than the Proton Synchrotron Booster.

PSB	Proton Synchrotron Booster, a circular hadron accelerator at CERN.
PV	Primary vertex, the first vertex of a decay chain.
QCD	Quantum chromodynamics, the relativistic quantum field theory describing the strong interaction.
QED	Quantum electrodynamics, the relativistic quantum field theory describing electrodynamics.
QFT	Quantum field theory, a kind of theory combining quantum mechanics, field theory and special relativity.
R20.7	Release 20.7 of the software framework ATHENA used in ATLAS.
R21	Release 21 of the software framework ATHENA used in ATLAS, the latest version.
RMS	Root mean square, the square root of a distribution's mean square.
RPC	Resistive-plate chamber, (basic element of) one of the subdetector systems in the ATLAS muon spectrometer, responsible for triggering in the barrel region.
SCT	Semiconductor tracking detector, a subdetector system of the Inner Detector in ATLAS.
SM	Standard Model of particle physics, a gauge theory describing elementary particles and their interactions.
SMP	Stable massive particle, in the definition of this work, a particle with a mass higher than that of any Standard Model particle that traverses the detector completely in its mean lifetime.
SPS	Super Proton Synchrotron, a circular hadron accelerator at CERN, larger than the Proton Synchrotron.
SUSY	Supersymmetry, a group of theories introducing a symmetry relating bosons and fermions.
TGC	Thin-gap chamber, (basic element of) one of the subdetector systems in the ATLAS muon spectrometer, responsible for triggering in the end-cap region.

ToF	Time of flight, the time a particle takes to propagate from the interaction point to the position of measurement.
TOTEM	TOTAL Elastic and diffractive cross-section Measurement, an experiment at the Large Hadron Collider.
TRT	Transition-radiation tracker, a subdetector system of the Inner Detector in ATLAS.
UED	Universal Extra Dimensions, a theory introducing additional compactified spatial dimensions.
xAOD	Analysis-object data, a basic data format used in ATLAS for storing the information related to reconstructed objects.

Acknowledgement

It is astonishing how many people ultimately have a share in this master's thesis despite the mere year of its writing. At this point, I want to express my deepest gratitude to all of them.

Nevertheless, there is a couple of people who deserve to be mentioned more specifically.

First of all, I am most grateful to Sascha Mehlhase for his guidance throughout the whole project. Your richness of ideas what to investigate and how to approach it shaped this work and made it an intriguing task all along the way, teaching me also the value of in-depth understanding over quick incomprehensible results. Thanks also for your patience over the whole period of time and in particular in the last month, in which you bore having to support two theses at the same time with calm resignation. It was a great pleasure to work with you.

My deep gratitude also to Dorothee Schaile who gave me the opportunity to write this thesis at her chair in the first place. The great working atmosphere in the LS Schaile is not least the merit of you, having always the best of each chair member in mind.

Further, a big thanks to my colleagues in the SMP analysis, Michael Adersberger, Jochen J. Heinrich, Sascha Mehlhase, Troels Petersen and Shlomit Tarem, for long physics discussions and explanations on muon and SMP reconstruction.

In particular, I want to thank Jochen J. Heinrich for his previous calibration of the muon spectrometer. Not only did your work give me a guideline how to approach this calibration but also a competing result I could try to outperform. As my final β resolution could not exceed yours, in the end: You win this time, Jochen.

Thanks also to Michael Adersberger for the great work atmosphere, infectious enthusiasm for physics and a nose for what is not worth investigating — and what is, in contrast. Without you, this work would have been significantly shorter.

In general, I want to say thanks to each member of the LS Schaile. One feels always welcome to ask for help or join less productive but fun activities with you.

Finally, I also want to thank my family for their never-ending support. Without you, this work would not be as good and, therefore, I am most grateful to you.

Selbstständigkeitserklärung

Hiermit erkläre ich, Martin Habedank, geboren am 26. Mai 1994 in Berlin, die vorliegende Arbeit mit dem Titel

Calibrating the ATLAS Muon Spectrometer for a Search for Charged Stable Massive Particles

selbständig verfasst und keine anderen als die in der Arbeit angegebenen Quellen und Hilfsmittel benutzt zu haben.

(Martin Habedank)
München, den 15. November 2018